NEUTRON SCATTERING CROSS SECTION AND ANALYZING POWER MEASUREMENTS FOR ^{28}Si AND ^{32}S

AND

NUCLEAR MEAN FIELD FROM -80 TO +80 MeV

by

Mohammad Abdulaziz Al-Ohali

Department of Physics
Duke University

NEUTRON SCATTERING CROSS SECTION AND ANALYZING POWER MEASUREMENTS FOR ^{28}Si AND ^{32}S
AND
NUCLEAR MEAN FIELD FROM -80 TO +80 MeV

by

Mohammad Abdulaziz Al-Ohali

Department of Physics
Duke University

Date: March 25, 1993

Approved:

Richard L Walter
Richard L. Walter, Supervisor

James Tomow

Alfred Lee

Laurence Norum

Calvin R. Howell

Dissertation submitted in partial fulfillment of the requirements for the degree of Doctor of Philosophy in the Department of Physics in the Graduate School of Duke University

1993

ABSTRACT

(Physics-Nuclear)

NEUTRON SCATTERING CROSS SECTION AND ANALYZING POWER MEASUREMENTS FOR ^{28}Si AND ^{32}S AND NUCLEAR MEAN FIELD FROM -80 TO +80 MeV

by

Mohammad Abdulaziz Al-Ohali

Department of Physics
Duke University

Date: March 25, 1993

Approved:

Richard L Walter

Richard L. Walter, Supervisor

Dennis Tomasi

Alfred Zee

Laurence Brown

Calvin R. Howell

Dissertation submitted in partial fulfillment of the requirements for the degree of Doctor of Philosophy in the Department of Physics in the Graduate School of Duke University

1993

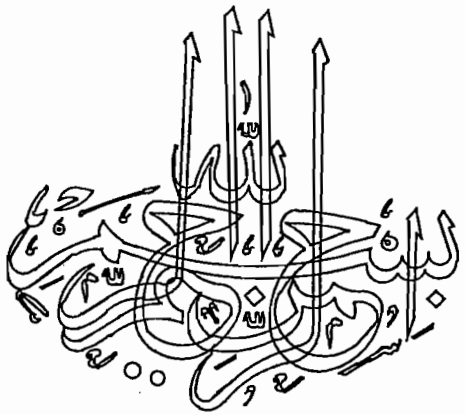

Abstract

Neutron Scattering Cross Section and Analyzing Power Measurements for ^{28}Si and ^{32}S and Nuclear Mean Field from -80 to +80 MeV

by
Mohammad A. Al-Ohali

The neutron scattering differential cross sections $\sigma(\theta)$ for ^{28}Si and ^{32}S have been measured at incident neutron energies of 15.5 and 19 MeV. For the same nuclei, the analyzing powers $A_y(\theta)$ were measured at 15.5 MeV. The $\sigma(\theta)$ measurement used a pulsed neutron beam from the ^{2}H(d,n)^{3}He reaction and the time-of-flight spectrometer at the Triangle Universities Nuclear Laboratory (TUNL). The same facility was used for the $A_y(\theta)$ measurement but the neutron beam was produced via the polarization transfer reaction $^{2}\mathrm{H}(\vec{d},\vec{n})^{3}\mathrm{He}$. The two set of data were corrected for the effects of flux attenuation, finite geometry and multiple scattering.

The data were combined with previous $\sigma(\theta)$, $A_y(\theta)$, and total cross-section data for ^{28}Si and ^{32}S to form a large database in the energy range between 1 and 80 MeV. In addition, information about binding energies of the single-particle states for the n-^{28}Si and n-^{32}S systems was incorporated to extend the database to negative energies. This database was interpreted in the framework of the nuclear mean field (NMF). The NMF for each system was derived from a Dispersive Optical Model (DOM) analysis that incorporates explicitly the Dispersion Relation (DR) which connects the real and the imaginary parts of the NMF. The extension of the DOM potential from the positive to the negative energy domain provides the shell-model potential for bound-state predictions. Each DOM describes the data very well except for the total cross section in the energy domain of $E < 8$ MeV; here the prediction is about 12% higher than the averaged experimental data. A comparison was done between the NMF for these two relatively light-mass nuclei with the mean fields of systems in the mass number region of $40 \le A \le 208$. The comparison demonstrates that the present parametrization of the strength and

the radius of the Hartree-Fock potential is consistent with previous parametrization.

A DOM analysis was applied to a similar database for the n-^{27}Al system, but most of the parameters were constrained to be close to those of the DOM for n-^{28}Si. The DOM for n-^{27}Al was able to predict the total cross section better than a previous DOM derived for the same system.

The new DOM for n-^{27}Al was combined with those for n-^{28}Si and n-^{32}S to describe the neutron elastic scattering from nuclei in the center of 2s-1d shell in the energy domain between 0 and 80 MeV. A constrained DOM for these nuclei in the mass number region $27 \le A \le 32$ is obtained. A comparison between the parameters obtained in the present DOM model with those obtained from the conventional Spherical Optical Model (SOM) reveals the importance of determining the Hartree-Fock potential strength from a database that contains a combination of scattering data and empirical information about single-particle bound states in the negative energy region.

ACKNOWLEDGMENTS

The one who does not thank people, does not thank ALLAH

It is a great pleasure to express my gratitude and appreciation to those people who have contributed in the completion of this dissertation. My thanks go first to my advisor, Professor Richard L. Walter. His valuable advice since my joining the Duke graduate school has been highly recognized and beneficial. The extensive encouragement, patience and long discussions *he* offered were very essential for this work. I would like to express special thanks to Dr. Werner Tornow and Dr. Calvin R. Howell for their crucial contributions to this investigation. Their expertise, assistance with data acquisition, many generous discussions and the time they have shared with me have enlightened my learning and educational attitude.

Thanks also go to Prof. Tom Clegg for the valuable experience I gained from his expertise with the polarized source. The many and long test runs on the new atomic polarized source were very valuable to my education.

The contributions of the following people who helped in the data acquisition of this work are recognized and appreciated: Paul Felsher, Gary Weisel, Mahmoud Nagadi, Ross Setze, , Richard Braun, Dr. J. Lambert (visiting professor from Georgetown Univ., Washington, D.C.) and Dr. Zemin Chen (visiting professor from Beijing, China).

The encouragement and the support of Prof. Edward G. Bilpuch is deeply appreciated. Prof. Russell Roberson and Prof. Chris Gould are recognized for the development of the data acquisition system at TUNL. Thanks also to all TUNL technical staff, Paul Carter, John Dunham, Sidney Edwards, and Patrick Mulkey. I thank Mari Cheves for the efficient editing of this dissertation.

A great acknowledgment goes to the King Fahad University for Petroleum and Minerals in Dhahran, Saudi Arabia for their support and

encouragement during my graduate education. The Cultural Mission of Saudi Arabia deserves my thanks for their support during my stay in the U.S.A.

Although words are not enough to express my great heart-felt thanks, my thanks and gratitude go to my *parents*. I feel their prayer all my life. The patience, the understanding and the support of my *wife* and my *children* are unforgettable.

Table of Contents

CHAPTER 5

The Nuclear Mean Fields of ^{28}Si and ^{32}S

CHAPTER 6

Global Dispersive Optical Model for ^{27}Al, ^{28}Si, and ^{32}S

CHAPTER 7

LIST OF FIGURES

LIST OF TABLES

CHAPTER 1

Introduction

Introduction

The complexity of the nucleus is such that even after more than eighty years of investigation and study, there is no fundamental theory that can exactly describe the structure of the nucleus or reactions between its constituents. Therefore, phenomenological models are still being developed to expand our understanding of the physical systems. Proposed models start as simple models, and then refinements or modifications are introduced to improve the model. The continuous efforts of refinements and modifications to an earlier model can be considered as a reflection of the success of that model.

One of the important approaches to understand nuclear physics is the study of the nucleon-nucleus interaction. The scattering of a nucleon from a nucleus provides a unique probe to the nuclear force. A direct aspect of this scattering is the angular distribution of the elastic scattering of neutrons. This angular distribution is dominated by a diffraction pattern, which is particularly recognizable for energies above a few MeV. This phenomenon is due to the combination of the finite size of the nucleus and the fact that the nuclear matter is "partially transparent" to the incident neutrons. A model, known as the "Optical Model Potential" (OMP) was introduced [Fer 49] to explain the observations of nucleon-nucleus elastic scattering. The model consists of replacing the many-body problem by a simple effective potential in a one-body Schroedinger equation. The name optical is due to its similarity to the treatment of an optical medium with a complex index of refraction. The empirical determination of the parameters and terms in the optical model potential has been thoroughly explored using much experimental elastic scattering data.

Since the proposal of the nucleon-nucleus optical-model potential, it has played an important role in the interpretation of data for many types of nuclear reactions. In particular, the OMP has had great success in describing the average behavior of elastic scattering observables (total and differential cross sections and analyzing powers) and reaction cross sections. However,

increasingly accurate experimental data made it clear that a simple parametrization of the OMP was no longer adequate to describe some of the deviations between the model predictions and the experimental data. One of these deviations is the non-linear behavior of the energy dependence of the real potential of the simple OMP and the need for energy-dependent radii and diffusenesses.

In order to properly explain such deviations from linearity or from constant-value geometry parameters, a physical basis must be established. This basis is provided by the dispersion relation (DR), which connects the real and imaginary parts of the optical potential. In several fields of physics, the DR has proven to be of great importance and in recent years has provided a powerful phenomenological framework for relating experimental data to the scattering interaction.

The introduction of the DR into OMP analysis gives a solid base for determining the low-energy optical potential by setting it in the framework of the *nuclear mean field* that extends from the negative-energy region, where it is normally called shell-model potential, to the positive-energy region, where it is called the optical-model potential. This broader description provides at least three advantages over earlier optical models:

i) It enables the low-energy OMP to be determined from a much wider range of data, not only from the scattering and total cross-section data, but also from the data on bound single-particle states of the negative energy region.

ii) It provides an important connection between real and imaginary parts of the OMP through the DR. This connection not only explains the Fermi-surface anomaly [Fin 85], but also gives an additional constraint that can be used to define the potential more precisely; therefore, it gives a more precise and physically sound determination for the model parameters.

iii) Most importantly, it enables a straightforward connection of the OMP for positive and negative energies. This extension to negative energies is of great significance because much more empirical information is available about the potential at positive energies than for negative energies, and for the first time it is

possible to safely use the scattering data to obtain properties of the shell-model potential. Previously, one had to obtain the shell model potential from a collection of fragmented and somewhat questionable experimental observables, such as the spectroscopic factors, single-particle orbits, occupation probabilities and spectral functions.

From the recent applications of the DR, one makes two observations. *First*, most of the nuclei that were studied are believed to have spherical shape. *Second*, the lightest nucleus studied was ^{40}Ca. Hence, no real test for the "full application of the DR" was made, for example, on a deformed nucleus or a nucleus with mass number A < 40. The very recent study of ^{27}Al nucleus by Nagadi [Nag 92] focused mainly on the positive energy region of the NMF (scattering region), and the extrapolation of the model towards the negative energy region was very limited because of lack of useful data. Therefore, it was important to investigate more fully the application of the DR in the lighter mass nuclei. In addition, the nuclei near the center of the 2s-1d shell provide an attractive ground to which many nuclear models have been applied due to their highly collective states. Furthermore, the wide separation between the ground state and the first-excited state of these nuclei makes it ideal to measure observables for neutron elastic scattering.

Therefore, the objective of the work described in this dissertation is three-fold: First, to incorporate the DR approach into the optical model to derive the nuclear mean field for neutrons in ^{28}Si and ^{32}S in a wide energy range between -80 and +80 MeV; Second, to complete the TUNL high-quality database of differential cross section and analyzing power for ^{28}Si and ^{32}S; Third, to investigate the applicability of the DR approach to light nuclei.

The presentation in this dissertation is divided in the following style. Chapter 2 explains the details of the measurement and data analysis of the differential cross section. Similarly, Chapter 3 explains the details of the measurement and data analysis of the analyzing power. The database used in this study is discussed in Chapter 4 along with the correction of the

compound nucleus. In Chapter 5 we present an overview of the concept of the nuclear mean field, the historical application of the Dispersive Optical Model (DOM) with its formulation, and the analyses of the mean field for n-^{28}Si and n-^{32}S. We devote Chapter 6 to the development of a new DOM study for n-^{27}Al, and to the extension of the present DOM study to develop a "constrained" regional DOM for the mass region $27 \leq A \leq 32$. Conclusions and comments are presented in Chapter 7.

CHAPTER 2

Cross Section Measurements

2.1 Experimental Equipment and Techniques

2.1.1 Introduction

The $^{28}Si(n,n_0)$ and $^{32}S(n,n_0)$ measurements of the differential cross section at incident neutron energies of 15.5 and 19.0 MeV and the analyzing power at 15.5 MeV were conducted using the time-of-flight spectrometer at Triangle Universities Nuclear Laboratory (*TUNL*) on the campus of Duke University. A floor plan of the laboratory is shown in Fig. 2.1. Starting from the upper left corner of the figure, and concentrating on the experiment-related equipment, are the two ion sources for the production of unpolarized (DENIS II) or polarized (ABPIS) deuteron beams. Next in line (and not shown in fig. 2.1) are the electrostatic lenses to focus and magnetic steerers to direct the beam into the bunching system just before injection into the accelerator. The beam is accelerated by the High Voltage Engineering model FN tandem Van de Graaff accelerator. At the high-energy end, the beam is bent 38° by an analyzing magnet and focused onto the deuterium gas cell in the neutron TOF target area, which is in the lower right corner of the figure.

In order to perform experiments involving neutron beams, some essential requirements must be met due to the fact that the neutron has no charge. *First*, neutrons cannot be accelerated using the electromagnetic force. This restriction requires the use of a nuclear reaction such as the $^2H(d,n)^3He$ reaction employed in the present work to produce a beam of energetic neutrons. *Second*, neutrons cannot be detected directly by ionization in materials. Hence, a nuclear reaction (n-p elastic scattering) is used to produce charged particles that can be detected by the energy deposited in a material through ionization. Moreover, the size of the neutron detectors need to be thick enough to compensate for the low detection efficiency.

Presented in the following sections are descriptions of the experimental procedure and apparatus utilized in the measurement.

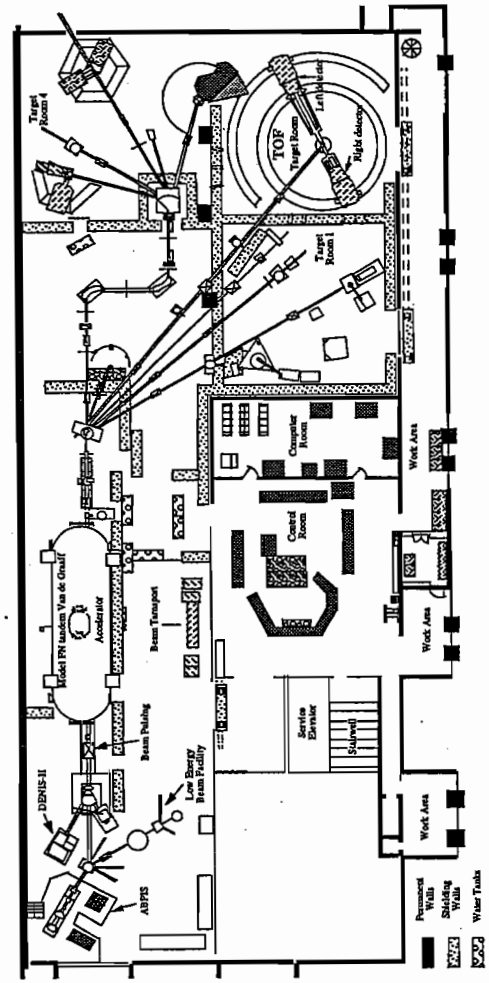

Figure 2.1. Floor Plan of the Triangle Universities Nuclear Laboratory (TUNL)

2.1.2 The Experimental Procedure

The measurement of the neutron differential cross sections was obtained through the procedure outlined here. An ion source produced a beam of deuterons. The beam was pulsed, accelerated and directed through a capacitive time-pickoff unit before passing through a thin foil into a deuterium gas target. Via the $^{2}H(d,n)^{3}He$ reaction, neutron beam pulses were incident on the sample. The scattered neutrons were detected by two liquid organic scintillators positioned in the horizontal reaction plane. A start signal from the detector followed by a stop signal from the pick-off unit were processed through a set of electronic modules and the information was sent to the VAX computer for analysis and storage.

The angular distribution yields were normalized to the relative incident neutron flux from the $^{2}H(d,n)$ reaction, which was monitored using a lightly shielded liquid scintillator. Absolute differential cross sections were obtained by normalizing the yields to that for n-p scattering, which were measured periodically in the same experimental arrangement and which were also normalized to the neutron flux using the monitor detector positioned at 50°.

2.1.3 The Ion Source

The deuteron beam was produced by a *Direct-Extraction Negative Ion Source* (DENIS II). A schematic diagram of DENIS II is shown in Fig. 2.2. A hot filament emits electrons which are accelerated toward the anode. On their way to the anode, the electrons collide with the deuterium atoms, producing a plasma containing negative deuteron ions. An electric field is applied between the anode and the extractor electrode to extract these negative ions. The negative beam is then focused by an electrostatic lens. The source is biased at -50 kV potential to accelerate the negative ion beam for injection into the tandem accelerator. This 50 keV DC beam with an intensity of about 15-20 μA is directed through the electrostatic lenses into the pulsing apparatus. More details about DENIS II can be found in [Gus 81, How 84].

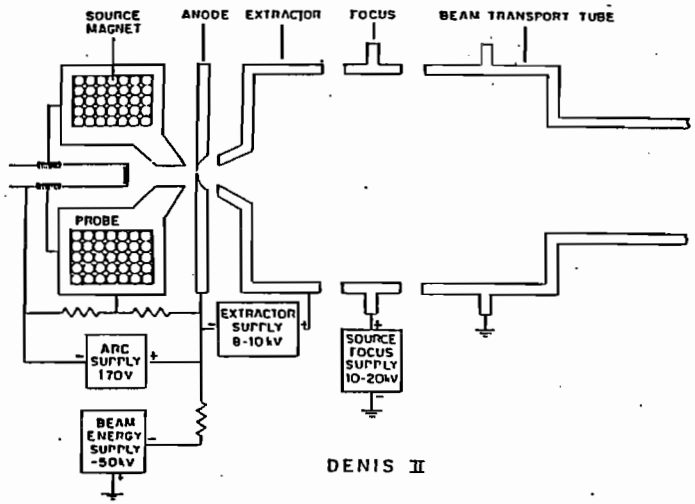

Figure 2.2. A schematic diagram of DENIS II used to produce the deuteron beam

2.1.4 Beam Pulsing

Before injecting the beam into the accelerator, the DC beam is pulsed. The pulses need to be compressed as narrow as possible to provide good energy resolution. In addition adjacent pulses need to have sufficiently large separation in time to avoid overlays of neutrons in the detectors from events induced by adjacent beam bursts. The beam pulsing process consists of two parts: *chopping* and *bunching*. A summary of the basic principles of beam pulsing is given here; more details can be found in [How 84, Rob 88]. First, the beam is *chopped* into pulses or segments by sweeping it across an aperture with a periodically varying transverse electric field applied to two parallel plates. Only the portion of the beam that traverses the chopper plates when the electric field is near zero passes through the aperture. The transmitted bursts are *bunched* or compressed in time by modulating the energy of the deuteron-ions in the beam segment so that they arrive at the target at the same instant. The buncher at TUNL is a double-gap buncher which is a system of cylindrical tubes consisting of three electrically insulated sections: a longer-section in the center and two short sections at either end separated by a small gap. A block diagram of the chopper and double-gap buncher system is shown in Fig. 2.3. A sinusoidal voltage is applied to the central section while the two end (outer) sections are held at ground potential. The phase between the chopping and bunching waveforms is adjusted so that the instantaneous potential across the first bunching gap (negative polarity) decelerates the front of the beam segment (negative-D ions) as it enters the gap. The rear of the beam segment is accelerated by the change in polarity. When the center of the segment passes through, there is no potential difference; hence, the system has no effect on this part of the beam segment. The length of the center section of the buncher is adjusted so that the beam particles traverse the distance between the gaps in one-half the sinusoidal period. This causes the beam segment to arrive at the exit of the buncher tube so that it experiences similar deceleration and acceleration effects as when it entered the buncher. The end result of this bunching is a non-uniform velocity distribution across the beam segment, causing a narrowing of the beam burst as it drifts toward the target. The efficiency of the TUNL bunching system just described is ≈20%

due to the fact that only ≈20% of the sine wave applied to the buncher is sufficiently linear to produce suitable bunching. In order to increase the beam bunching efficiency, a second buncher was added. It operates at twice (10 MHz) the frequency of the first buncher and is adjusted to run 180° out of phase from the first. This two-stage double-drift bunching system is capable of compressing ≈60% to 65% of the DC beam into a beam burst of approximately 2.0 ns full width at half maximum (FWHM) on target. For the cross-section measurements the time averaged beam intensity on target was kept under about 2μA in order to avoid damage to the foil of the deuterium gas cell described below.

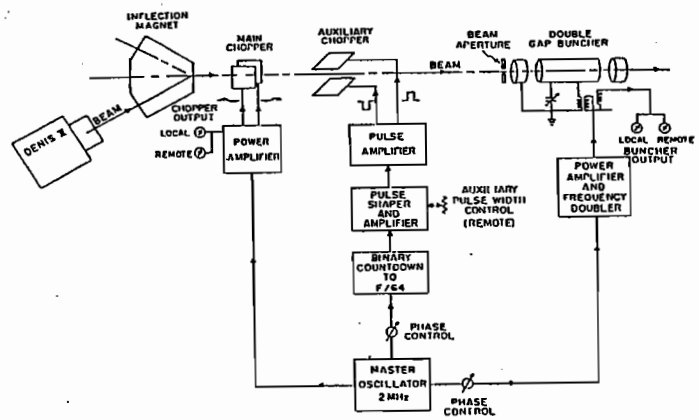

Figure 2.3. The chopper and buncher system used to pulse the beam.

2.1.5 Acceleration and Beam Transport

The pulsed and negatively-charged deuteron ions were accelerated by the *FN Tandem Van de Graaff accelerator*. A positive-charged terminal is connected to evacuated acceleration tubes and placed in the center of the accelerator tank that is filled with an insulating gas. The tandem can reliably operate at terminal voltages up to 9 MV, and therefore the accelerated ions can acquire an energy up to 18 MeV in passing through the tandem. The tandem principle is that the negative ions are accelerated to the terminal where a thin carbon foil strips two electrons from the negative ions, upon which the beam becomes positively charged. The positive ions are then accelerated additionally by traveling from the terminal to ground potential at the far end of the accelerator. The terminal voltages used for the $\sigma(\theta)$ measurements were 6 and 8 MV.

In December of 1991, the performance of the TUNL accelerator was upgraded by the installation of a new charging system (pellatron chain) and new acceleration tubes. In addition, the quality of the insulating gas was improved by mixing a small amount of sulfur hexafluoride with the normal insulating gas (CO_2). The pellatron chain has the advantages, in contrast to the conventional belts, of not producing dust (which can result in tank sparks), being mechanically stiff so ripples on the terminal voltage due to belt flop is eliminated, and requiring little maintenance. These new improvements added more stability to the system, improved the beam transmission, and allowed the accelerator to run up to 10 MV.

After the beam exits from the high-energy end of the tandem, it is bent by the "20-70" analyzing magnet through 38° into the TOF beam leg and then transported to the TOF experimental area. The 38° momentum-analyzing magnet provides accurate determination of the deuteron beam energy. A pair of horizontal slit edges, located just after the analyzing magnet, are used to provide a fast-feedback signal to the accelerator terminal. In order to maintain the terminal voltage, the difference signal from these slits is sent to the corona control circuit to make minor adjustments to the terminal voltage.

The deuteron beam is transported from the ion source to the accelerator and from the accelerator to the analyzing magnet by means of

electric and magnetic steerers, and by means of electrostatic and magnetic quadrupoles for focusing the beam. A beam-line vacuum of about 5 x 10^{-7} Torr is provided by diffusion and cryo pumps in stations along the beam transport system.

2.1.6 Neutron Source Reaction

At the end of the 38°-beam leg, the pulsed deuteron beam enters the gas cell containing deuterium to produce neutrons via the $^2H(d,n)^3He$ reaction. This particular monoenergetic reaction was chosen for the following reasons: i) The high cross section at the reaction angle of zero degree in the energy range of this experiment. ii) The angular distribution of neutrons is forward peaked (i.e., the cross section falls off rapidly with angle), which causes a reduction of neutron background in the side detectors. iii) The positive Q-value (+3.269 MeV) provides good separation between the desired neutrons that originates from the reaction to the ground state of ^3He, and the neutrons originating from the $^2H(d,np)^2H$ reaction breakup with Q-value (-2.22 MeV).

The gas cell, as shown in Fig. 2.4, is a cylindrical tube of 0.8 cm in diameter and 3.16 cm long. The outer wall of the cell is made of stainless steel while the side wall is lined with a 0.38 mm thick tantalum sleeve. The end wall of the cell (i.e., beam stop) is lined with a 0.51-mm thick tantalum disc held in place by the tantalum sleeve. The purpose of the sleeve is to shield the gas cell from the deuterons that scatter from the deuterium gas inside the cell. On the beam entrance side, the gas was contained inside the cell with a 6.35-μm thick Havar foil. The gas cell is isolated electrically so that the amount of charge deposited by the beam can be monitored by a beam current integrator. Air cooling was applied to the gas cell assembly to avoid heat buildup in the cell. The gas cell was pressurized with high purity deuterium which was passed through a liquid nitrogen trap before entering the cell to remove hydrocarbon contaminants. As can be seen from Table 2.1, two gas pressures were employed. Neutron energies of 15.5 and 19.0 MeV with spread in neutron energy of 160 and 251 keV, respectively were used in the measurements. The spread in energy of the neutron beam is due to the fact that neutrons are produced in the $^2H(d,n)^3He$ reaction at different sites along the gas cell. (the quoted energy spreads neglects the

folding in of the approximately 20 keV energy spread due to straggling of the deuterons in the entrance foil.)

Table 2.1 Beam energy loss in the gas cell (All energies are in MeV)

E_n (MeV)	Gas pressure (atm)	Deuteron energy loss in foil	Deuteron energy loss in the gas
15.5	4.0	0.214	0.160
19.0	7.8	0.177	0.251

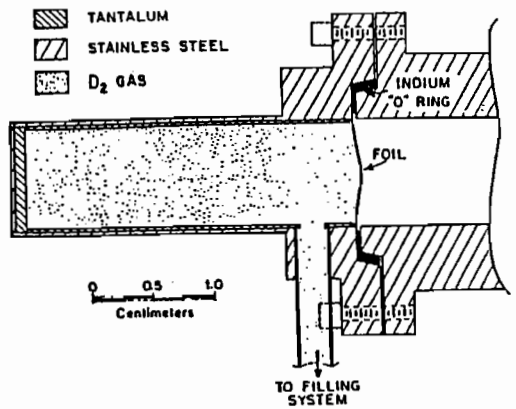

Figure 2.4: The deuterium gas cell used in the measurement.

2.1.7 Scattering Samples

Four scattering samples were used in the experiment. All the samples were right circular cylinders. Table 2-2 lists the descriptions and the isotopic compositions of the samples. The polyethylene and the carbon samples were used for absolute normalization purposes, while the ^{28}Si and ^{32}S samples were the nuclei under study. The samples were mounted coaxially on a vertical steel wire which passed through the pivot point of the side detectors. The center of the samples was aligned along the incident deuteron beam axis and at a distance of 11.4 cm from the center of the gas cell. A Zeiss optical level was used to check the proper centering of the samples.

Table 2.2 The Descriptions of the Scattering Samples.

Sample	Mass (g)	Radius (cm)	Height (cm)	Isotopic composition	
Polyethylene	3.37	0.717	2.279	^{1}H ^{12}C	66.7% 33.3%
Carbon	2.911	0.477	2.376	^{12}C ^{13}C	99.0% 1.0%
Silicon	25.27	1.176	2.528	^{28}Si ^{29}Si ^{30}Si	92.55% 4.55% 2.90%
Sulfur	23.63	1.230	2.540	^{32}S ^{33}S ^{34}S	95.28% 0.74% 3.98%

2.1.8 Neutron Time-Of-Flight Spectrometer

The neutrons scattered from the target sample were detected using the neutron TOF spectrometer facility at TUNL shown in Figs. 2.1 and 2.5. Four neutron detectors compromise the overall TOF system; two main detectors and two monitors. All detectors are liquid organic scintillators of NE-213 or NE-218 contained in cylindrical glass housing and coupled to photomultiplier tubes. All the scintillators provide good pulse-shape-

discrimination (PSD) characteristics and fast signal response [How 84]. The *two main detectors* were located in the horizontal plane, defined by the detector axes and the beam axis, one to the right (called the Right-detector) and the other to the left (called the Left-detector) of the incident beam axis.

A very prominent feature of the Right and the Left detectors is the large massive shields surrounding them. The shields weigh about 500 kg and contain a large amount of a mixture of paraffin loaded with lithium carbonate. Parts of the collimator and shielding near the detector are made of copper and lead. A schematic diagram of the detector's shielding and collimation is shown in Fig. 2.6. The front-portion of each shield consists of a doubly-truncated conical collimator that was designed to minimize the number of detected neutrons that did not scatter directly from the sample while permitting the entire detector to view the complete sample [Gla 74]. At the back of the detector, copper and polyethylene was added to reduce the background of neutrons scattered from the walls behind the detector. Tungsten shadow bars were used to shield the detector and the collimator throat from the direct neutron flux from the neutron source. Details of the shadow bars setting are described in [Bey 81]. A schematic diagram of the detectors shielding and collimation is shown in Fig. 2.6. The detector shields were mounted on carriages which allow changes in their radial position (longer or shorter neutron flight paths) and in their angular position (0^{o} to 160^{o}).

Another main part of the system was a detector suspended from the ceiling called *"ceiling monitor detector"*. The purpose of this detector was to provide monitoring of the direct neutron flux emitted from the gas cell to be used for the $\sigma(\theta)$ normalization. This detector viewed the neutron-source reaction (gas cell) from a distance of 1.8 m above the reaction plane and at an angle of about 50^{o}. To shield this detector from neutrons scattered around the room, the detector was housed in a 50 kg copper cylinder with collimator inserts.

The fourth detector, called the *zero-degree detector*, was located along the axis of the incident deuteron beam and at a distance of about 4 m from the gas cell. The purpose of this detector was to monitor the direct neutron beam's time characteristics, i.e., pulse shape and width. During the course of

The TOF stop signal was derived from the pulse induced in a capacitive pick-off unit located in front of the gas cell. The *pick-off* unit is a tube of 6.4 cm in length and 1.9 cm in diameter.

Table 2.3 Summary Of The Detectors

Detector	Purpose	Position	Thickness (cm)	Diameter (cm)	Fl. Path (m)
Right	Angular Yield	18° -155°	5.08	8.88	2.50 -3.90
Left	Angular Yield	18° -155°	5.08	12.7	3.76 -5.70
Ceiling	Flux Monitor	55°	5.1	5.1	fixed
Zero-deg	Timing	0°	5.1	5.1	fixed

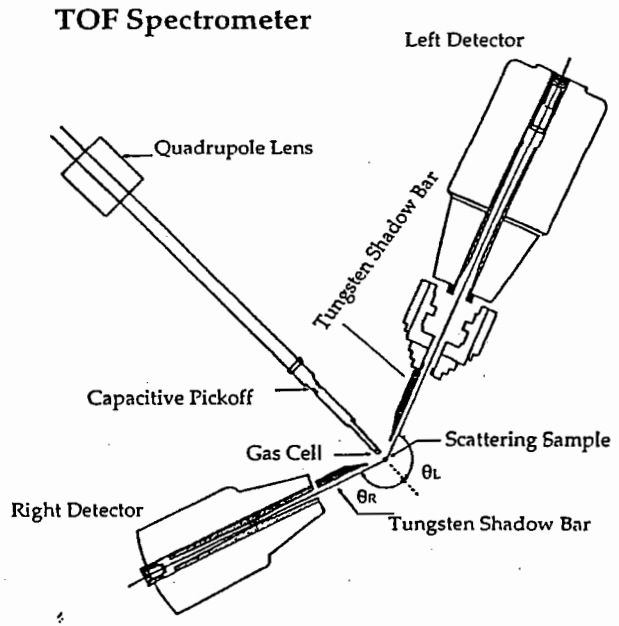

Figure 2.5 . Neutron TOF spectrometer at TUNL.

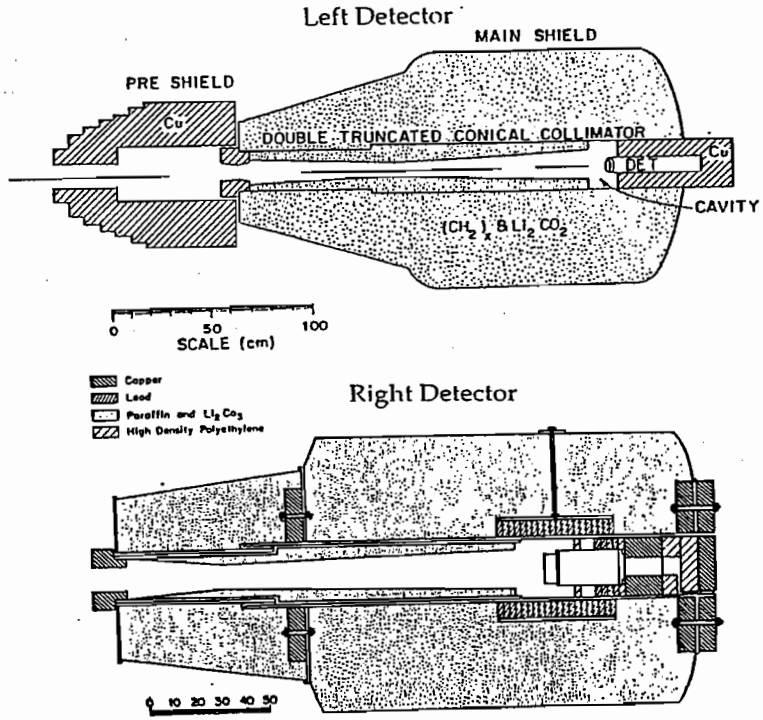

Figure 2.6: The *Right* and the *Left* detector shielding and collimation.

2.1.9 Electronics

The TOF electronics is based on two signals, the detector anode signal that is used as a start signal and the pick-off signal that is used as a stop signal. For the four detectors used in the TOF spectrometer, there were four sets of almost identical electronic modules designed to analyze and process the light output information from each scintillator. A block diagram of the electronics used in the measurement is shown in Fig. 2.7. The fast signal from the photomultiplier anode was brought to the control room via a 50-ohm low-loss cable and sent to three different branches in the circuit to process the signal. Each signal had to meet three requirements: 1) **Energy bias:** A bias level was set on the recoil pulse-height to reject low energy events. This was achieved by amplifying the signal and feeding it to a single-channel analyzer (AMP-SCA). The SCA was operated in a mode that produced a logic signal (gate) whenever an input pulse had an amplitude greater than the bias level. This level was set at 1/2 of the maximum height of the Compton recoil edge produced by the 0.662 MeV γ-rays from ^{137}Cs, as shown in Fig. 2.8. This bias, called "1 $\times$ Cs bias", corresponds to the light output of a proton having an energy of about 1.6 MeV. The SCA-bias gate was sent to a universal coincidence module.

2) **Pulse shape discrimination:** The PSD was used to discriminate against pulses due to γ–rays, therefore reducing the background in the TOF spectra. The principle of this discrimination is based on the differences in the time profile of the light produced in the scintillator for γ–rays and neutrons. In the scintillator, the γ–rays interact with the atomic electrons (low-ionizing electrons), while the neutrons interact via n-p scattering (high-ionizing protons). Electrons and protons produce light flashes in the scintillator with two different decay responses (the light produced by electrons has a shorter decay time than that from protons).

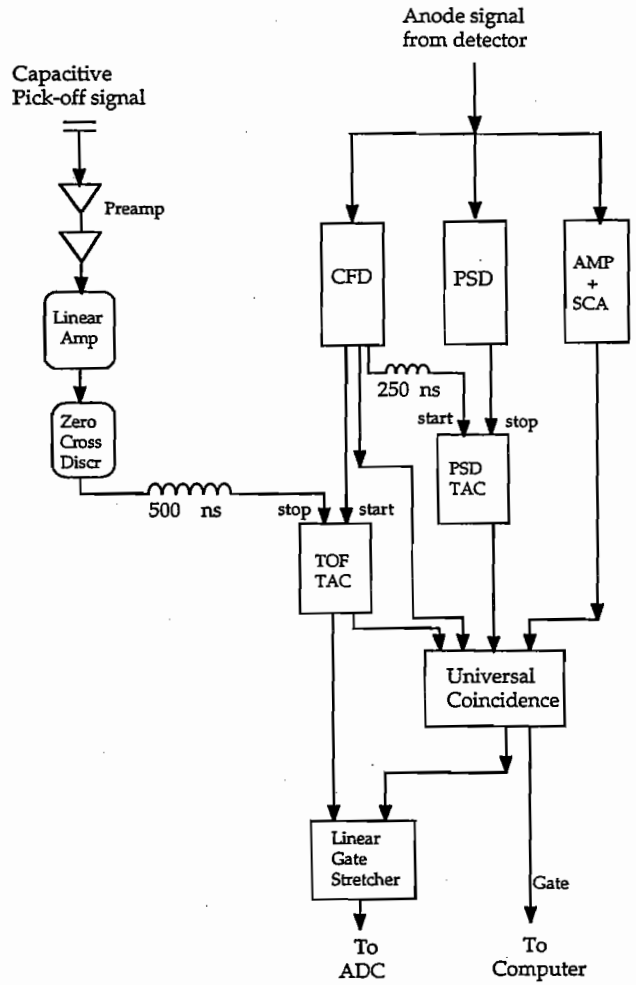

Figure 2.7. Block diagram of the electronics used in the $\sigma(\theta)$ measurement.

In order to apply the required discrimination, the incoming anode signal was fed to two modules: the constant-fraction discriminator (CFD) and the pulse-shape discriminator (PSD). The signal coming out the PSD was triggered by the trailing edge of the pulse while the signal coming out the CFD was triggered by the leading edge. These two output-signals were used to start and stop the time-to-amplitude converter $(TAC)_{PSD}$ which produces an output voltage proportional to the time difference between the two signals. Thus the $(TAC)_{PSD}$ spectrum has two distinct peaks corresponding to γ–rays events and neutron events. The neutron events were selected by setting a broad window on the neutron peak using the SCA of the $(TAC)_{PSD}$, which produced a gate whenever an event fell within this window. The gate was then sent to the universal coincidence to be used in coincidence with the energy bias requirement mentioned above. The PSD requirement for the neutron events was set before the start of the experiment using an Am-Be radioactive neutron source. The Am-Be source was used instead of the neutron beam because it provides a clean spectrum with less γ–rays than the spectrum from the beam scattered from the sample.

3) **TOF measurement:** In the time-of-flight electronics a pulse whose amplitude is proportional to the time interval between two reference pulses is produced to indicate the relative times of occurrence of the events. The first reference was a *start* signal, coming from the CFD which was triggered by the detector anode signal, and the second was a *stop* signal produced by the capacitive beam pick-off. The two signals were used to start and stop, respectively, a time-to-amplitude converter $(TAC)_{TOF}$ operated with a 200-ns range. The pick-off signal was derived from the time the deuteron beam pulse arrived at the gas cell. This pick-off signal was amplified, fed into a discriminator and then delayed to arrive at the $(TAC)_{TOF}$, after the start signal. The reason for choosing the neutron detector signal to be the start signal rather than the pick-off signal, was to reduce false signals (signals that do not produce valid neutron-events in the detectors) from starting the TAC and causing it to be busy. The pick-off pulse rate was 2.5 MHz in the $\sigma(\theta)$ measurements and 5 MHz in the $A_y(\theta)$ measurements and would have locked up the TAC if it was used as the start signal. Thus the $(TAC)_{TOF}$

produced an output which had a voltage proportional to the time of flight of the detected neutron or γ–ray. This output was then shaped by a linear gate and stretcher.

The $(TAC)_{TOF}$ linear signal from the linear gate and stretcher was gated by the logic output of the universal coincidence and then sent to an analog-to-digital converter (ADC). The gates were counted using scalers. The ADC and computer dead time was monitored by calculating the ratio of the number of gates to the number of events. No corrections were needed for the electronics dead time because it was very small.

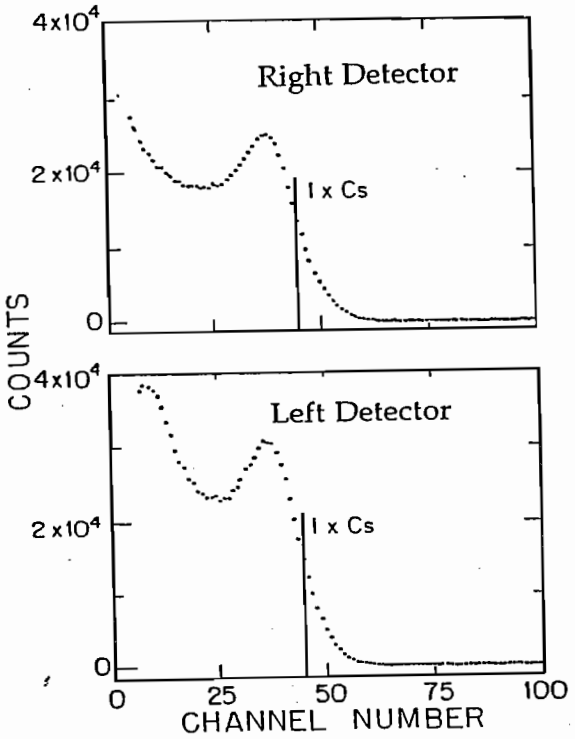

Figure 2.8. The Compton recoil spectrum in the Right and the Left neutron detectors. The so-called "1×Cs" energy bias is indicated. Note the offset for zero counts.

2.1.10 Data Acquisition

Once the signals for valid neutron events were processed by the electronics and digitized by the ADC's, the resulting digital information was sent to the TUNL VAX 11/780 computer for data analysis and storage. In the later stages of the present work, the mainframe was replaced by a 3200-micro VAX workstation. The hardware used as interface between the ADC's, scalers and the VAX was based on CAMAC crates controlled by a Microprogrammed Branch Driver (MBD-11). A more thorough description of the data acquisition hardware at TUNL is given by King *et al.* [Kin 81] and Roberson *et al.* [Rob 81]. The new micro Vax system was designed and installed by N.R. Roberson, C.R. Howell and S.E. Edwards of Duke University and TUNL.

The software system XSYS used to control the data acquisition and analysis was originally developed at TUNL [Gou 81]. The system XSYS is a set of general purpose commands available to all experimenters at TUNL. In addition, packages of routines written in Digital Equipment's Command Language (DCL) and FORTRAN were written specifically for the $\sigma(\theta)$ measurement. These routines were combined into an on-line data acquisition software package for the neutron time-of-flight measurement called NTOF and into an off-line data analysis software package called NTOFOFF.

The $\sigma(\theta)$ for ^{28}Si and ^{32}S were measured at incident neutron energies of 15.5 and 19.0 MeV. The TOF spectra were accumulated with the left and right detectors from 18° to 160° in 4° step intervals. These spectra are 1024 channel wide and each channel corresponds to 0.18 ns. For each element and at each scattering angle, two spectra from both detectors were taken in "sample-in" and "sample-out" configurations. When one of the silicon or sulfur samples was in front of the neutron beam, the condition is called "sample-in"; the "sample-out" configuration is when the sample was removed and the bare wire (identical to the one holding the sample) was in place of the sample. To minimize the effect of any sample misalignment relative to the neutron beam axis, which gives an incorrect scattering angle, the forward-angle measurements were taken simultaneously with both left and right detectors at the same scattering angle but on opposite sides of the

neutron beam axis. In the final data presentation, the measurements at a given angle were averaged to minimize the errors resulting from uncertainties in the detector angular position.

In addition to the silicon and sulfur samples, polyethylene and a ^{12}C scatterer were used to measure the yield for neutron scattering from hydrogen for absolute normalization purposes. These measurements were taken at different times during the angular distribution measurement, usually at the beginning, middle and end of an angular distribution measurement. The angles where these measurements were carried out were chosen to give maximum resolution of the hydrogen peak from the peaks due to elastic and inelastic scattering of carbon [Gus 82]. The angles were θ =27° for 15.5 MeV and 25° for the 19 MeV. All of these data were taken concurrently with the measurements of M. M. Nagadi who investigated neutron scattering from ^{27}Al and ^{59}Co. It was more efficient and more convenient to combine these efforts, since time is lost when the detector-angle positions are changed. In addition, the same sample-out configurations could be used for all 4 samples, thus reducing the running time considerably. Altogether, the $\sigma(\theta)$ and $A_y(\theta)$ experiments took about 56 24-hr shifts of beam. The data accumulation was divided into eight 7-day runs.

At each angle, the neutron flux was monitored by the ceiling detector and the associated spectra were stored in data areas for yield normalization. Similarly, the zero-degree monitor was used to monitor the time characteristics of the beam pulses. The data were accumulated with an average statistical uncertainty of 3%, and with a time resolution of about 2 ns (FWHM). Some of the characteristics and parameters of the experiment are listed in Table 2-4.

Table 2.4 Characteristics of the Experimental Parameters

Parameter	Value	Parameter	Value
Beam Intensity	2.4 μA	Chopper Frequency	2.5 MHz
FWHM	2 ns	Terminal Voltages	6 & 8 MV
Gas Pressure	7.8 atm	Energy spreads	160, 251 keV

2.2 Data Analysis

The process of extracting the valid neutron events from the neutron time-of-flight spectra plays a crucial role in obtaining correct cross-section values. In order to insure correct normalization of the measured TOF spectra and to investigate the systematics of the measurement, several tests were conducted to inspect any drifts or variations in the timing and flux monitor spectra. All data analyses were performed using a software package called NTOFOFF operating under the TUNL system XSYS.

The following sections describe the steps carried out to derive elastic differential cross sections from the measured TOF spectra for $^{28}Si(n,n_o)$ and $^{32}S(n,n_o)$. Three steps are involved in this process: peak stripping and background determination, data normalization, and the finite-geometry corrections.

2.2.1 Neutron-Yield Extraction

The neutron yield was extracted at each scattering angle for the left and the right detectors by first generating a TOF "difference" spectrum that was obtained by subtracting the properly normalized sample-out spectrum from the sample-in spectrum. The sample-out spectrum was scaled by the ratio of the counts of the neutron-flux monitor for the sample-in and sample-out condition.

The neutron-flux monitor yields were obtained by summing the neutron events inside a selected monitor window after subtracting an underlying background. Fig. 2.9 shows a sample of a TOF neutron-flux monitor spectrum. The monitor window was set on the narrow peak of neutrons coming directly from the $^2H(d,n)^3He_{g.s.}$ reaction in the gas cell. In choosing this window, two conditions were imposed: i) the window should be narrow to reduce the uncertainty associated with fitting the underlying background shown in Fig. 2.9, and ii) to choose the window to be wide enough to avoid steep slopes on the peak in order to minimize the effect on the monitor yield due to small shifts in timing. To detect any shift in timing, the centroid of the peak in the monitor spectrum was monitored

throughout the peak-stripping process for the entire angular distribution measurement. If necessary, the monitor window was shifted a channel or two to compensate for small time drifts. Tests were made to study the sensitivity of the monitor yield to the particular choice of the left-edge of the monitor window. All these tests revealed that the monitor yields were not sensitive to the choice of the left-side of the monitor peak as long as the width of the windows was unchanged. After the monitor window was chosen, several tests were conducted to estimate the level of background lying under the neutron peak by fitting the regions to either side of the peak of interest with a least-square fitting routine. In Fig. 2.9 the solid vertical lines show the monitor window, and the two windows, defined by the dashed vertical lines, were used for determining the background. In order to keep the same normalization for the entire angular distribution, the *width* of the background windows as well as the *width* of the monitor window were not changed. Then, the yields of the monitor spectra for the sample-in (Y_{in}^{mon}) and the sample-out (Y_{out}^{mon}) were determined by summing all neutron events inside the monitor window and above the background.

The scaling of the sample-out spectrum to the sample-in spectrum was done by multiplying the sample-out spectrum by the ratio of the "monitor-in" counts and the "monitor-out" counts. A difference spectrum for each sample was then generated by subtracting the normalized sample-out spectrum from the associated sample-in spectrum.

Similarly, a difference spectrum for hydrogen was generated from the polyethylene and the carbon spectra. Since the carbon scatterer contains the same number of carbon nuclei as the polyethylene scatterer (CH_2), the difference spectrum for hydrogen was calculated by subtracting the normalized carbon spectrum (used as an 'out' spectrum) from the polyethylene spectrum (used as a 'in' spectrum). Fig. 2.10 shows an example of a sample-in, a scaled sample-out and a difference spectrum for ^{28}Si.

The difference spectrum exhibits a small residual background which is associated with the presence of the sample. This background was adequately described by a linear function in the region of the elastic peak. When choosing the window for summing the events in the peak, care was taken to include all good neutron events (see Fig. 2.10 b). The neutron yield

per monitor events (Y_S) was calculated in the difference spectrum by summing the events inside the peak window and above the residual background, and dividing by the "monitor in" yield (Y_{in}^{mon}). That is:

$$Y_s(\theta) = \frac{1}{Y_{in}^{mon}}\left(Y_{diff} - B_{diff}\right) \qquad (2\text{-}1)$$

where Y_{diff} are the events inside the peak window in the difference spectrum,
and B_{diff} is the residual background in the difference spectrum.

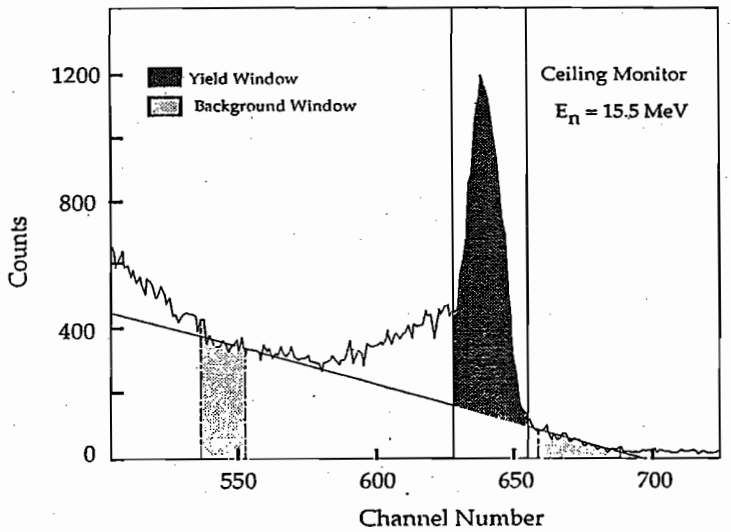

Figure 2.9. Neutron-flux monitor spectrum obtained by the ceiling detector at a neutron energy of 15.5 MeV.

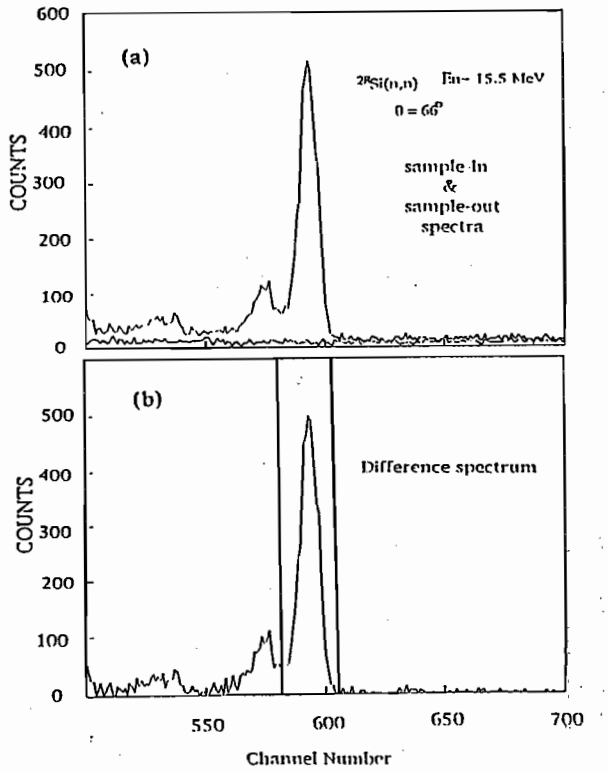

Figure 2.10. **(a)** The sample-in and the sample-out TOF spectra for ^{28}Si at $\theta_l = 66°$ for E_n=15.5 MeV.

(b) The difference spectrum. The vertical lines indicate the window used for summing the yield.

2.2.2 Data Normalization

The neutron yields extracted by the above method were normalized to obtain an absolute differential cross sections. During the angular distribution measurement, usually at the beginning, middle and end of the individual distributions, a polyethylene and a ^{12}C scatterer were used to measure the yield for neutron scattering from hydrogen. A certain normalization angle was chosen for each incident neutron energy distribution to give maximum resolution of the hydrogen peak from the inelastic of carbon [Gus 82]. The angles were θ =27° for 15.5 MeV and 25° for the 19 MeV. The TOF difference spectrum for the hydrogen nuclei was generated from the polyethylene and ^{12}C scatterers as explained in Sect. 2.2.1.

At the normalization angle θ_H, the yields of neutrons scattered from the ^{28}Si and the ^{32}S samples at the lab scattering angle θ_l, were compared to the yields for neutrons scattered from hydrogen nuclei. The measured differential cross section $\sigma(\theta_l, E_n)$ at the lab angle θ_l and neutron energy E_n was normalized using the equation:

$$\sigma(\theta_l, E_n) = \frac{Y_S(\theta_l)}{Y_H(\theta_H)} \cdot \frac{N_H}{N_S} \cdot \frac{1}{F(\theta_H, E_n)} \cdot \sigma_H(\theta_H, E_n) \qquad (2\text{-}2)$$

where $Y_S(\theta_l)$ is the yield per monitor for the sample, and $Y_H(\theta_H)$ is the yield per monitor for hydrogen obtained from the difference spectrum of the normalization measurement at lab angle θ_H. The ratio N_H/N_S is the number of hydrogen nuclei in the polyethylene sample divided by the number of nuclei in the scattering sample. The σ_H (θ_H, E_n) is the well-known n-p scattering cross section at the energy E_n and angle θ_H [Hopkins and Breit 1971]. The $F(\theta_H, E_n)$ is a correction factor which accounts for the relative detector efficiency and for attenuation, finite-geometry, and multiple-scattering effects applied to the hydrogen yield. The calculation of these correction factors were obtained from the Monte-Carlo computer code EFFIGY15 which is discussed in detailed in Sect. 2.2.3. Briefly, the correction for the hydrogen was performed as follows:

The code was run in its two-nuclei mode to generate a TOF spectrum for the polyethylene scatterer, using a library containing the total cross sections and differential elastic cross sections for both hydrogen and carbon as well as inelastic cross sections for carbon. From the carbon scatterer, a TOF spectrum was generated to be used as an 'out' spectrum. The difference spectrum was then calculated by subtracting the carbon spectrum (out spectrum) from the polyethylene spectrum, since the carbon scatterer contains the same number of carbon nuclei as the polyethylene scatterer. Finally, the yield was determined by setting a window in the difference spectrum around the hydrogen peak in the simulated spectrum. From the ratio of the known cross section (the library value) to the calculated yield, the correction factors $F(\theta_H,E_n)$ were deduced. The correction factors for hydrogen at E_n =15.5 MeV and 19.0 MeV were 1.205 and 1.224, respectively.

The uncertainties accompanying the data normalization step are listed in Table 2-5.

Table 2-5 Sources of Uncertainties for $\sigma(\theta)$

SOURCE	VALUE
A. Relative Uncertainties	
1. Counting Statistics and Background	1.5-6 %
2. Relative Detector Efficiency	2.5 %
3. Multiple-scattering Correction*	0.8 - 1 %
B. Normalization Uncertainties	
1. n-p Cross Section	0.7 -1.2 %
2. Hydrogen Yield	0.5 - 1 %
3. Polyethylene Correction Factor	2.2 %
4. The ratio N_H/N_S of number of nuclei	0.8 - 1 %

*Does not include error enhancement from subtracting multiple-scattering events.

2.2.3 Finite-Geometry Correction

In the theoretical definition of $\sigma(\theta)$ and $A_y(\theta)$, it is assumed that neutrons scatter from a point target and are detected by a point detector. However, the experiment requires that the neutron source, the target and the detector are all of finite dimension. Fig. 2.11 compares the geometrical configuration of the ideal scattering situation and the real experiment.

The finite-geometry compromises are required to compensate for the low counting rate due to the following basic reasons. a) Neutron experiments are a "double-scattering process". Neutrons that are first produced by a source reaction are scattered from a target before their detection, which involves a second scattering process. Such experiments usually are low count-rate experiments. b) The need for a pulsed beam for the TOF experiments. When the DC beam generated by the ion-source is pulsed, a good fraction of the beam is lost (about 40% for the $A_y(\theta)$ experiments and 80% in the $\sigma(\theta)$ measurements). (This was particularly harmful in the $A_y(\theta)$ measurement where the beam from the ion-source is the limiting factor in the time spent to measure the data.) c) The energy resolution requirements for TOF experiments. The TOF technique seeks better energy resolution which is proportional to the neutron flight path: the longer the sample-detector distance, the better TOF energy resolution. This longer flight path leads to a lower counting rate because the counting rate is inversely proportional to the square of the sample-detector distance. d) The neutrons are detected indirectly as a recoil proton and their detection depends on nuclear cross sections which in turns require large-volume detectors to compensate for the low detection efficiency.

The above finite-geometry compromises produce finite-geometry effects which require corrections to the experimental data. The relatively large size of the scattering sample leads the incoming neutron flux to be attenuated in the sample. The attenuation of the neutron flux in the sample causes the effective center of the sample to be slightly shifted towards the neutron source (due to the high illumination of that side). This makes the effective scattering angle smaller than the apparent scattering angle measured in the laboratory. The scatterer, which was located at 11.4

cm from the center of the gas cell, subtended an angle of $\Delta\theta = 5.9°$ in the reaction; it was crucial to accurately determine the mean scattering angle by properly accounting for the variation of $\sigma(\theta)$ across the face of the scatterer. Moreover, the relatively large size of the detector subtends a finite solid angle; the total angular spread seen at the detector is about 1.3°.

In addition to attenuation effects, the finite size of the sample causes neutrons to be scattered several times within the sample before exiting. This multiple scattering causes neutrons that are originally headed towards the detector to be scattered into another direction, i.e., a loss of counts, and the multiple scattering causes neutrons that were scattered in another direction to be scattered a second or third time into the direction of the detector.

All the above effects require the observed differential cross-section and analyzing power data to be corrected for finite geometry, multiple scattering and flux attenuation.

For the differential cross-section data, these finite geometry corrections were calculated using the code EFFIGY15, a Monte Carlo simulation of the experiment using an iterative procedure. The process starts by assuming the experimental data as a trial point-geometry library of cross sections. Then the code is run, which folds in the effects of multiple scattering and finite geometry. If the trial guess leads to a computed $\sigma(\theta)$ different from that observed, then the difference between the two is employed to adjust the point-geometry $\sigma(\theta)$ library and the next iteration is performed.

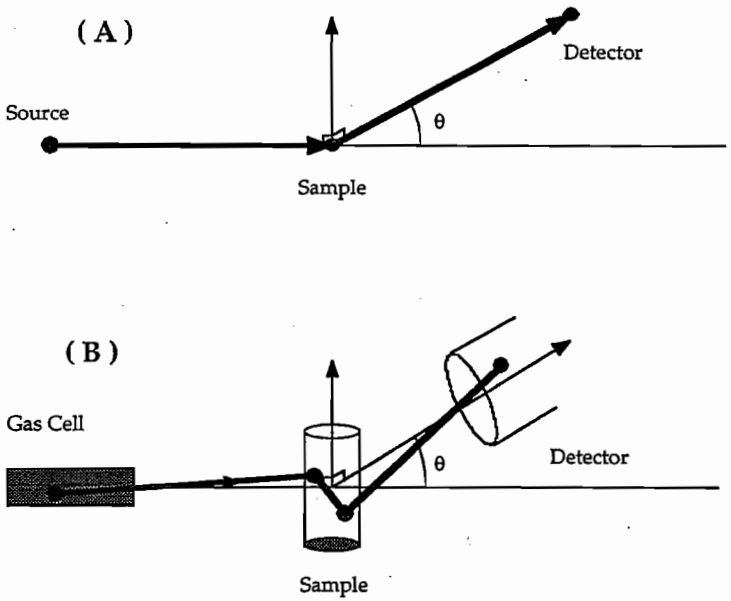

Figure 2.11 Geometrical configuration of (A) the ideal scattering and (B) a doubly-scattered neutron observed in the real experiment.

The simulation requires a library of total and differential cross sections at the energies needed for the calculation. In addition, it requires an input file containing the parameters of the experimental setup; these include the experimental geometries, detector efficiency, and information about the neutron production differential cross section and mass density of the sample. The simulation was done by keeping track of the orders of scattering within the sample (single, double and triple) with sufficient neutron histories. The sufficient number of neutron histories was achieved when the uncertainties in the correction factors computed from the simulated yields are much less than the experimental uncertainties (about 15% of the experimental uncertainties). An example of EFFIGY15's simulation for the relative yields for the different orders of scattering from the ^{28}Si sample is shown in Fig. 2.12. The angular distribution observed in the laboratory would correspond to the sum of these three contributions.

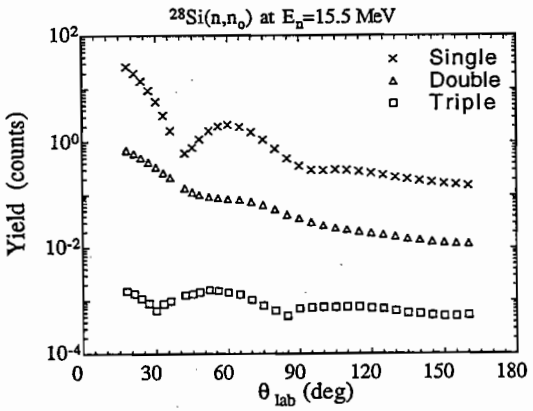

Figure 2.12. Simulated relative yields for single, double, and triple scattered neutrons from ^{28}Si at 15.5 MeV.

Next, windows were selected in the simulated time-of-flight spectra in a similar manner as the experimental windows were set. The code, then sums the events inside those windows and calculates the cross sections. Once the cross sections from the simulation are calculated, the code used them with the values generated from the current cross-section library to generate the correction factors. These correction factors are then applied to the experimental data at each angle to obtain the corrected values for the differential cross sections.

After each iteration, the code makes comparisons between the calculated and the experimental cross sections to check if convergence is achieved. If not, the cross-section library is updated with the new corrected values and the code begins a new iteration. The code continues this process until the iteration process reach convergence within a set percentage.

EFFIGY15 also calculates the mean neutron energy at which the experiment was performed. Figs 2.13 and 2.14 show the final data in the c.m. system for ^{32}S and ^{28}Si, respectively, after all the corrections were applied, along with the uncorrected data. The multiple-scattering effect is prominent in the valleys of the cross section, where it tends to fill in the valleys in the minima. The angle shifts due to averaging over the angular resolution of the sample and the detector were less than 1°, except at the steep slopes of the distribution were it reached up to 2.3°. The flux attenuation of neutrons, which causes the experimental yield to be low, is the dominant correction for the data. It added up to 16% in ^{28}Si, and about 15% in ^{32}S. The uncertainties in the data due to the multiple-scattering corrections (as listed in Table 2-5) ranges between 0.8 and 1 %.

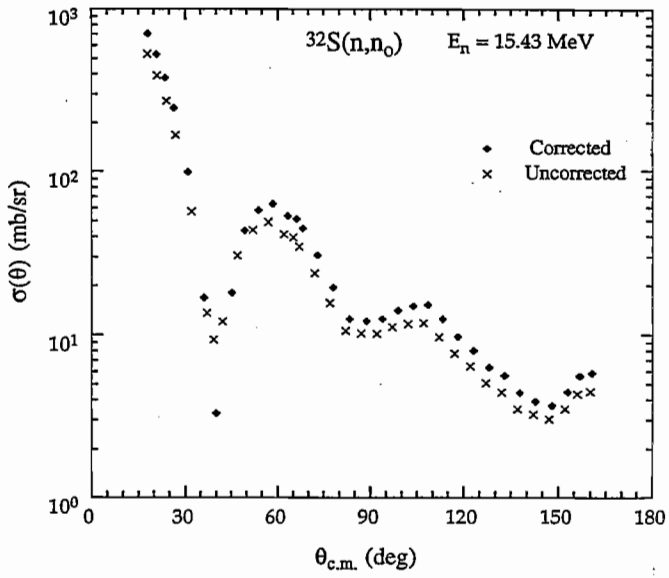

Figure 2.13. The final corrected data in the c.m. system for ^{32}S at 15.43 MeV compared to the uncorrected data.

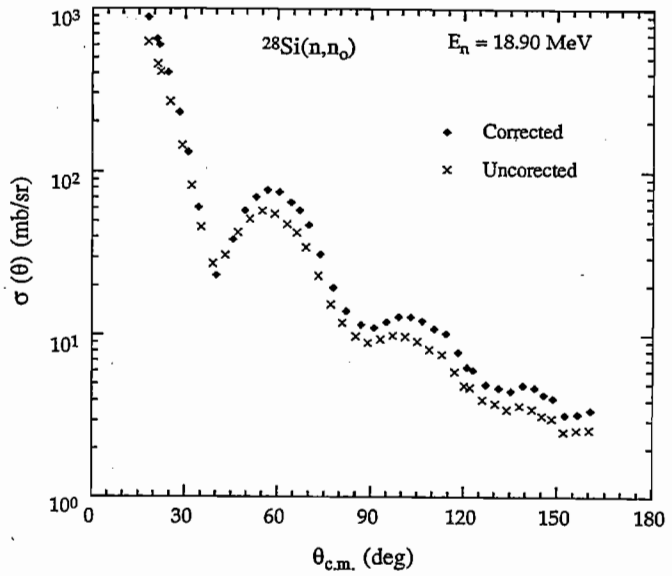

Figure 2.14. The final corrected data in the c.m. system for ^{28}Si at 18.90 MeV compared to the uncorrected data.

2.2.4 Data Presentation

After all of the above corrections were applied, the data were described in the center-of-mass system with Legendre polynomials expanded in the following form:

$$\sigma(\theta,E)=\sum_{l=0}^{n} a_l(E)\cdot P_l(\cos\theta) \qquad (2\text{-}3)$$

The a_l(E) are the Legendre polynomial expansion coefficients. The fits were carried out using the TUNL code MACRO. The order of the polynomial fit was chosen to be a compromise of the following three criteria:

a. *Minimum chi-square* which is defined as

$$\chi^2=\sum_{i=1}^{N}\frac{1}{\Delta\sigma_{exp}{}^2}\left[\sigma_{fit}(\theta_i)-\sigma_{exp}(\theta_i)\right]^2 \qquad (2\text{-}4)$$

Here $\sigma_{fit}(\theta_i)$ and $\sigma_{exp}(\theta_i)$ are the calculated (fit) and the experimental cross sections, respectively, the $\Delta\sigma_{exp}$ is the error associated with $\sigma_{exp}(\theta_i)$, and N is the number of data points.

b. *Wick's limit:* The elastic scattering cross section at zero degree must be consistent with Wick's inequality [Hod 71] (i.e., $\sigma(\theta=0^\circ)$ should be greater than or equal to Wick's limit σ_W(E) as in the following relation:

$$\sigma(0^\circ,E)\geq\sigma_w(E)=\left[\frac{k}{4\pi}\sigma_T(E)\right]^2 \qquad (2\text{-}5)$$

Here σ_T (E) is the total cross section, and k is the center-of-mass wave number.

c. *Observed fit* : An eye judgment was used to establish best fits to the data especially at the large backward angles ($\theta > 160^\circ$) where there were no data. To assist in this criterion, it was necessary to insert into the data set (for the purpose of Eq. 2-3 calculations) a fictitious data point at $\theta = 175^\circ$. The value chosen was taken from an (global) optical-model calculation and a large error was assigned to it. Without this approach, the polynomial fit would often give unphysical results beyond about 170°.

The elastic cross sections for ^{28}Si and ^{32}S with the corresponding Legendre polynomial representations at the mean neutron energies of 15.44 and 18.90 MeV are shown in Figs. 2.15 and 2.16, respectively. The Legendre polynomial expansion coefficients for all representations are tabulated in appendices A-1 and A-2.

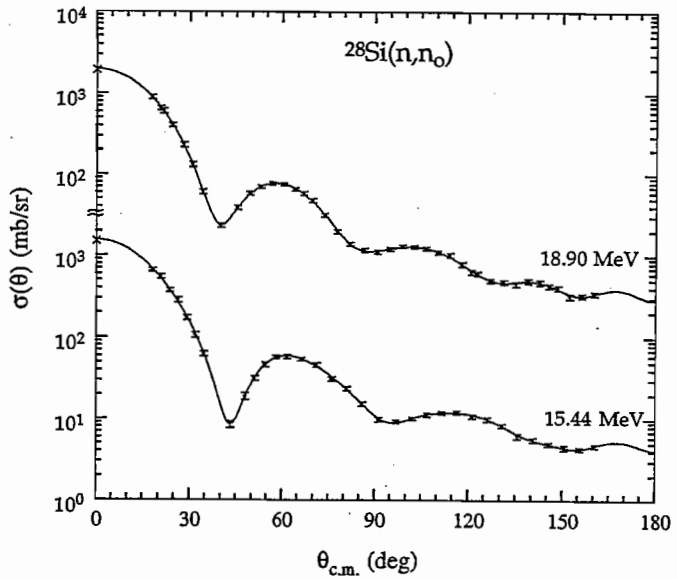

Figure 2.15. Elastic neutron scattering from ^{28}Si at mean neutron energies of 15.44 and 18.90 MeV. Curves are Legendre polynomial fits, dots are the experimental data. The Wick's limit is indicated at θ=0° by × for each curve.

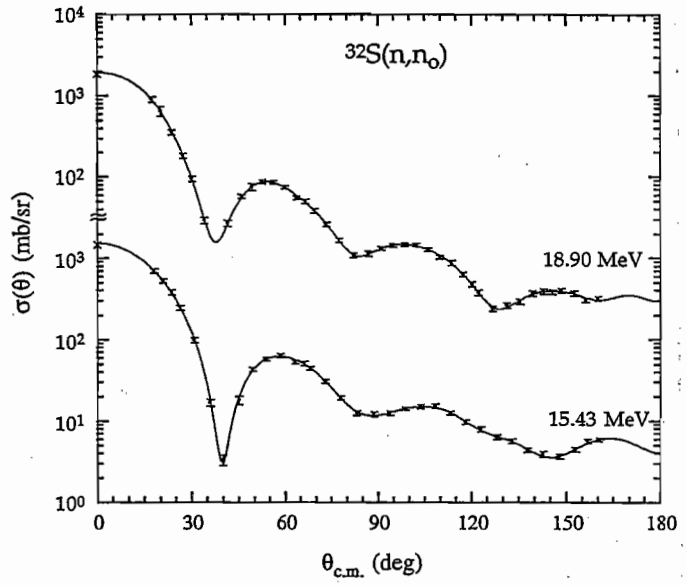

Figure 2.16. Elastic neutron scattering from ^{32}S at mean neutron energies of 15.43 and 18.90 MeV. Curves are Legendre polynomial fits, dots are the experimental data. The Wick's limit is indicated at $\theta = 0°$ by × for each curve.

CHAPTER 3

Analyzing Power Measurements

3.1 Polarization Observables

3.1.1 Introduction

There is an excellent facility at TUNL to measure polarization observables in nuclear reactions. Part of this project focuses on the measurements of the analyzing power for neutrons scattered from ^{28}Si and ^{32}S. The necessary beam of polarized neutrons is obtained via the polarization transfer ^{2}H($\vec{d}$,$\vec{n}$)^{3}He reaction. In the following sections we give a discussion of definitions involved in describing polarization phenomena and the related polarization formalism. Also, the difference between conducting measurements of the polarization of a beam of particles and the analyzing power is described. However, it is important to define first the coordinate system used for the description of the polarization $P(\theta)$ and the analyzing power $A_y(\theta)$. For a comprehensive discussion of polarization phenomena and formalism, one should consult Haeberli [Hae 74] and Ohlsen [Ohl 72].

3.1.2 The Madison Convention

In the present discussion the Madison-convention coordinate system shown in Fig. 3.1 is assumed [Hae 74] for the description of the polarization and the analyzing powers. This system is defined to be a right-handed coordinate system with the z-axis in the direction of the incident beam momentum, $\hat{k}_{in}$. The positive y-axis is defined by $\hat{k}_{in}x\hat{k}_{out}$ where $\hat{k}_{out}$ is along the momentum of the outgoing particle. The spin quantization (or symmetry) axis ζ is defined by the polar angle β and the azimuthal angle ϕ. The angle β is measured between $\hat{k}_{in}$ and the quantization axis ζ, with $0 \le \beta \le \pi$. The angle ϕ is measured between y-axis and the projection of ζ onto the x-y plane, with $0 \le \phi \le 2\pi$. For the measurement of the $A_y(\theta)$ in this project, the direction of the spin quantization axis ζ is set by the Wien Filter

(see Sect. 3.2.3) such that β=90° and ϕ=0° (i.e., the direction of ζ is along the y-axis).

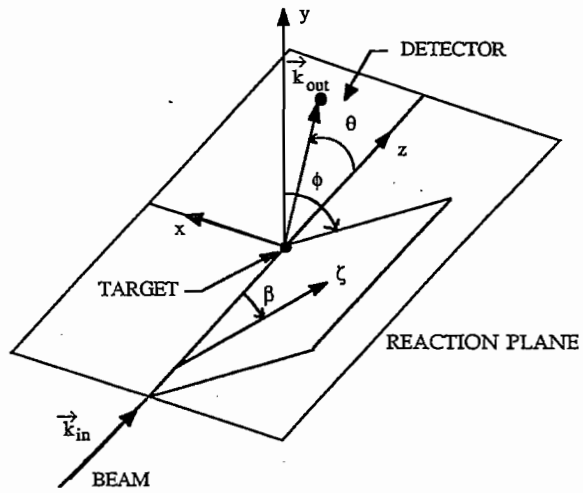

Figure 3.1. The coordinate system specifies the spin quantization axis ζ and the angles β and ϕ.

3.1.3 Definitions and Formalism for the Beam Polarization

The polarization state of a beam composed of particles of spin S can be completely described by $(2S+1)^2-1$ parameters [Hae 74]. The polarization parameters are certain expectation values of the spin operator $\vec{S}$ averaged over all particles in the beam. For deuterons (spin-1 particle), two types of polarization parameters are usually defined: the vector and the tensor beam moments. In Cartesian notation, these are:

vector polarization	$P_i = \langle S_i \rangle \qquad i = x, y, z$	(3-1)
tensor polarization	$P_{ij} = \frac{3}{2}\langle S_iS_j + S_jS_i \rangle - 2\delta_{ij}i, j = x, y, z$	(3-2)

The polarized beam that is produced in the ion source has an axis of symmetry of the spin system ζ about the z-axis. The z-axis is along the quantization axis defined by the direction of the source's magnetic field. Any axially symmetric polarization state can be represented by an incoherent mixture (see Fig. 3.2) of particles N_+ with spin along $+\zeta$, particles N_- with spin along $-\zeta$, and particles N_0 with the spins uniformly distributed in a plane perpendicular to the z-axis.

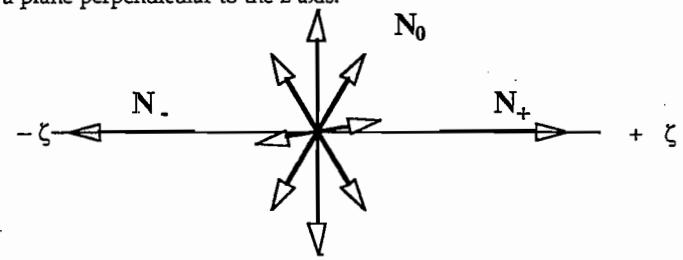

Figure 3.2. Schematic representation of an axially symmetric spin-1 system.

This axial symmetry property of the polarized beam reduces the polarization beam moments (of Eqs. 3-1 and 3-2) to only two moments [Hae 74], namely P_ζ and $P_{\zeta\zeta}$ where:

$$P_\zeta = N_+ - N_- \tag{3-3}$$

$$P_{\zeta\zeta} = 1 - 3N_o. \tag{3-4}$$

Furthermore, the polarization P_ζ and $P_{\zeta\zeta}$ can be related to the coordinate system (Fig. 3.1) in terms of the angles β and ϕ. Only the vector polarization P_ζ was measured in this project. The following is the expression for the vector components of P_ζ (assuming the quantization axis is along the z-axis as an axis of symmetry):

$$P_x = - |P_\zeta| \sin\beta \sin\phi \tag{3-5}$$

$$P_y = |P_\zeta| \sin\beta \cos\phi \tag{3-6}$$

$$P_z = |P_\zeta| \cos\beta \tag{3-7}$$

Similar expressions for the tensor moments can be found in [Ohl 72] or [Hae 74].

The availability of polarized ion sources makes it easy to study many polarization aspects. One of these aspects is the *analyzing power* $A_y(\theta)$. To understand $A_y(\theta)$, first we need to talk about the cross section when the incident beam is polarized. The cross section for a reaction produced by a polarized beam is different from the cross section for unpolarized beam. The relative change in cross section, when the incident beam is polarized, is related to the *analyzing power*. Fig. 3.3 shows the relationship between the cross section and the analyzing power [Hae 73].

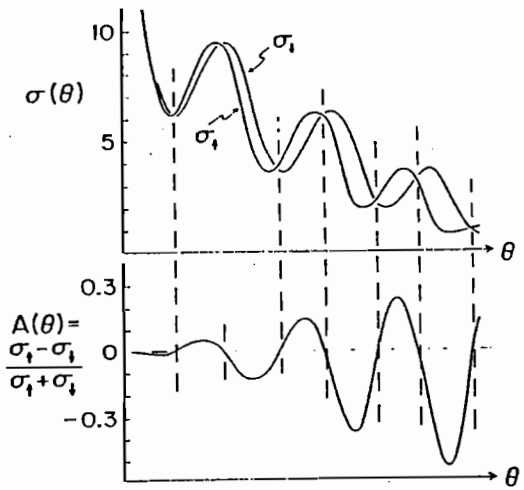

Figure 3.3. The relationship between the cross section and the analyzing power (lower curve), assuming 10% shift in angular scale between the $\sigma(\theta)$ for an incident beam polarized in the spin up direction and $\sigma(\theta)$ for spin down [Hae 73].

3.1.4 Analyzing power

If one can describe the incident polarized incident beam in a frame of reference, as in Fig. 3.1 , where its z-axis is along the projectile momentum direction and the y-axis is along the normal to the reaction plane defined by $\hat{k}_{in}x\hat{k}_{out}$. Then the general form of the cross section for a polarized deuteron beam, is given by [Dar 71] :

$$\sigma(\theta)=\sigma_0(\theta)\left[1+\frac{3}{2}P_\zeta A_y(\theta)\sin\beta\cos\phi+\frac{1}{4}P_{\zeta\zeta}A_{zz}(\theta)\left(3\cos^2\beta-1\right)\right.$$
$$\left.-P_{\zeta\zeta}\,A_{xz}(\theta)\sin\beta\cos\beta\sin\phi-\frac{1}{4}P_{\zeta\zeta}\left(A_{xx}(\theta)-A_{yy}(\theta)\right)\sin^2\beta\cos2\phi\right] \quad (3\text{-}8)$$

where $\sigma_0(\theta)$ is the cross section for unpolarized beam, and P_ζ and $P_{\zeta\zeta}$ are the vector and the tensor polarization moments of the beam. The $A_y(\theta)$ is the vector analyzing powers. The $A_{zz}(\theta)$, $A_{xz}(\theta)$, $A_{xx}(\theta)$, $A_{yy}(\theta)$ are the tensor analyzing powers. Using a pair of symmetric-angle detectors (Left and Right of the beam axis), one can define the two spin directions:

1) *Spin up* ($\beta=90°$ and $\phi=0°$), where the incident beam quantization axis is along the *positive* y-axis, then Eq. 3-8 reduces to:

$$\sigma_{Lu}(\theta)=\sigma_0(\theta)\left[1+\frac{3}{2}\,P_\zeta\,A_y(\theta)+\frac{1}{2}\,P_{\zeta\zeta}\,A_{yy}(\theta)\right], \quad (3\text{–}9)$$

$$\sigma_{Ru}(\theta)=\sigma_0(\theta)\left[1-\frac{3}{2}\,P_\zeta\,A_y(\theta)+\frac{1}{2}\,P_{\zeta\zeta}\,A_{yy}(\theta)\right], \quad (3\text{–}10)$$

σ_{Lu} and σ_{Ru} are the cross sections measured by the left and right detectors for the spin-up direction. The change in sign in the second term of Eq. 3-10 is due to the reverse in sign of the vector analyzing power in going from the left side of the $\hat{k}_{in}$ direction to the right (i.e., $\sigma(\theta)$ distribution shifts in opposite directions for the two symmetric angles). Solving Eq. 3-9 and 3-10 for $A_y(\theta)$ gives:

$$A_y(\theta)=\frac{1}{P_\zeta}\left(\frac{\sigma_{Lu}(\theta)-\sigma_{Ru}(\theta)}{\sigma_{Lu}(\theta)+\sigma_{Ru}(\theta)}\right). \quad (3\text{-}11)$$

2) *Spin Down* ($\beta=-90°$ and $\phi=0°$), where the incident beam quantization axis is along the *negative* y-axis, then Eq. 3-8 reduces to:

$$\sigma_{Ld}(\theta)=\sigma_0(\theta)\left[1-\frac{3}{2}\,P_\zeta\,A_y(\theta)+\frac{1}{2}\,P_{\zeta\zeta}A_{yy}(\theta)\right], \quad (3\text{–}12)$$

$$\sigma_{Rd}(\theta)=\sigma_0(\theta)\left[1+\frac{3}{2}\,P_\zeta\,A_y(\theta)+\frac{1}{2}\,P_{\zeta\zeta}A_{yy}(\theta)\right]. \quad (3\text{–}13)$$

σ_{Ld} and σ_{Rd} are the cross sections measured by the left and right detectors for the spin-down direction. The change in sign in the second term of Eq. 3-12 is due to the reverse in sign of the vector polarization of the beam. Then solving Eq. 3-12 and 3-13 for $A_y(\theta)$ gives:

$$A_y(\theta)=\frac{1}{P_\zeta}\left(\frac{\sigma_{Ld}(\theta)-\sigma_{Rd}(\theta)}{\sigma_{Ld}(\theta)+\sigma_{Rd}(\theta)}\right). \quad (3\text{-}14)$$

A detector actually measures counts or yield (not $\sigma(\theta)$) which is proportional to the differential cross section as:

$$Y=K\,\sigma(\theta)=(\eta\,n\,I\,t\,rd\Omega)\,\sigma(\theta), \quad (3\text{-}15)$$

where η is the detector efficiency, I is the incident flux, n is the target density, t is the time counted and $rd\Omega$ is the detector solid angle.

The efficiency and the solid angle are not the same for the two detectors. Hence, from Eq. 3-15, $K_{Lu}\neq K_{Ru}$. Therefore, using two detectors with one spin direction will introduce numbers of instrumental asymmetries. However, these instrumental asymmetries can be eliminated by combining the $A_y(\theta)$ from the spin-up and spin-down directions using two symmetric detectors. The result of such a combination gives the optimum method of measuring the vector analyzing power. This method is called the "two-detectors spin-flip" method. The expression for $A_y(\theta)$ from Eq. 3-11 and 3-14 and using the yield as in Eq. 3-15 gives:

$$A_y(\theta)=\frac{1}{P_\zeta}\left(\frac{\sqrt{\frac{L_uR_d}{L_dR_u}}-1}{\sqrt{\frac{L_uR_d}{L_dR_u}}+1}\right), \quad (3\text{-}16)$$

where L_u and L_d are the spin-up and spin-down yields for the Left detector, and R_u and R_d are the spin-up and spin-down yields for the Right detector. Using a short notation,

$$\alpha=\sqrt{\frac{L_uR_d}{L_dR_u}}, \quad (3\text{-}17)$$

and

$$\varepsilon(\theta)=\frac{\alpha-1}{\alpha+1}, \quad (3\text{-}18)$$

where α is the effective left-right ratio and $\varepsilon(\theta)$ is the scattering asymmetry,

$$A_y(\theta)=\frac{1}{P_\zeta}\left(\frac{\alpha-1}{\alpha+1}\right)=\frac{1}{P_\zeta}\cdot\varepsilon(\theta). \quad (3\text{-}19)$$

3.1.5 Beam Polarization and Analyzing Power Measurement

The relationship given by Eq. 3-19, provides an important tool for measuring the beam polarization or the vector analyzing power. In both cases the observed quantity is the scattering asymmetry, $\varepsilon(\theta)$.

In the *analyzing power measurement*, we want to determine the effect of the polarization of the incident beam on the scattering cross section, knowing the beam polarization, P_ζ. Then by measuring the scattering asymmetry, $\varepsilon(\theta)$, and using Eq. 3-17, $A_y(\theta)$ can be determined.

For the *beam polarization measurement*, a nuclear reaction of a precisely known analyzing power must be used. If we assume, $X(\bar{a},b)Y$ is the nuclear reaction used, with X represnting the calibrated scatterer nucleus, $\overline{Ay}$ the accurately known analyzing power, and $\bar{a}$ is the polarized incident particle, then we can measure the polarization of the polarized incident particle, P_a. First, we measure the effect of the polarization of the incident particle (of unknown polarization) on the scattering cross section of X at a selected angle. Once the $\varepsilon(\theta)$ is measured, then by using Eq. 3-19 in the form $P_a(\theta)=\frac{\varepsilon(\theta)}{\overline{Ay}}$, one can calculate the beam polarization (see Sect. 3.3.2). One can relate P_a to P_ζ through the particular transfer reaction utilized from the ion source.

3.2 Experimental Equipment and Techniques

3.2.1 Introduction

The $^{28}Si(n,n_o)$ and $^{32}S(n,n_o)$ measurements of the analyzing power $A_y(\theta)$ at an incident neutron energy of 15.5 MeV, were conducted using the neutron TOF facility described in Chap. 2. The main difference between the differential cross sections and the analyzing power measurements is that the latter utilizes a polarized beam to induce the neutron-generating reaction. The new Atomic Beam Polarized Ion Source (ABPIS) at TUNL was used to produce a continuous (DC) beam of polarized deuterons of 50 keV energy. This DC beam was pulsed and bunched and then accelerated by the tandem Van de Graaff. The beam was transported to the same NTOF target area that was used earlier for the $\sigma(\theta)$ measurement. The 15.5 MeV polarized neutrons were produced at $\theta=0^\circ$ via the polarization transfer $^2H(\vec{d},\vec{n})^3He$ reaction [Lis 75]. The polarized neutrons were scattered from the same silicon and sulfur samples previously used in the $\sigma(\theta)$ measurement. The scattered neutrons were detected by the two detectors (the right and the left) positioned symmetrically about the beam axis. The flight paths for the right and the left detectors were 3.26 m and 3.82 m, respectively. Some of the characteristics and parameters of the experiment are listed in Table 3-1.

Table 3-1 Experimental parameters for the $A_y(\theta)$ measurement

Parameter	Value	Parameter	Value
Beam Current	450 nA	Repetition Rate	5 MHz
FWHM	2 ns	Gas Pressure	7.8 bar
Beam Polarization	61 %	Neutron Polarization	54 %

3.2.2 Beam Polarization and its Production

The polarized deuteron beam was produced using an atomic beam polarized ion source which utilizes the Stern-Gerlach separation of atoms with given electronic spin projection. What follows next is a brief description of the population of the hyperfine substates of the deuterium atoms in their ground states in an external magnetic field.

The deuterium atom has a *nucleus* with a spin of $\hbar$, and an *electron* with a spin of 1/2 $\hbar$. Therefore, in a magnetic field, the nucleus spin can align its magnetic moment in one of three possibilities (m_I = -1, 0, and +1), while the electron spins has two ways for alignment ($m_j = \pm 1/2$). So, the projection of the total angular momentum produces six possible hyperfine states with different atomic energy levels. These hyperfine states are labeled 1, 2,..., 5, 6 in the energy level diagram of deuterium shown in Fig. 3.4.

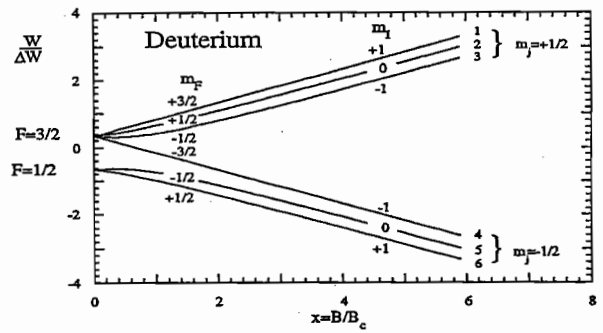

Figure 3.4. The hyperfine splitting of deuterium s a function of applied B-field strength.

The aim of the polarization process is to select certain hyperfine substates to produce a desired polarization. In the first stage of the

polarization process, the beam is passed through a sextupole magnet which provides an inhomogeneous magnetic field. The field of the sextupole magnet, which increases linearly with the radial distance from the beam axis, exerts a restoring force on the atoms *focusing* those with spin projection m_j=+1/2 and *defocusing* those with m_j=-1/2. The focusing of atoms with m_j=+1/2, is due to the opposite alignment of the electron magnetic moment with the field which cause them to move toward the lower magnetic field to minimize their energy, thus forcing them to pass axially through the magnet center. Atoms with m_j=-1/2 experience a corresponding force. It causes them to move away from the axis of the magnet. As a result, the three upper states with m_j=+1/2 (labeled 1, 2 and 3 in Fig. 3.4) are focused toward the axis of the beam, while the three lower states with m_j=-1/2 (labeled 4, 5 and 6) are deflected away from the beam axis. After the first sextupole magnet, the beam with hyperfine states 1, 2 and 3 is fully polarized in electronic spin.

In the second step, the electron polarization of the beam is converted into nuclear polarization. This is accomplished by causing the atoms to perform resonant transitions between substates of opposite m_j. This may require a second sextupole magnet (to remove newly populated m_j=-1/2 substates) and more transitions until all remaining substates have the same m_I. Thus, a polarized beam is produced.

3.2.3 The Polarized Ion Source (ABPIS)

The TUNL *Atomic Beam Polarized Ion Source* (ABPIS) is a low temperature ion source. It has basically four sections; (1) dissociator, (2) sextupole separation magnets, (3) transition units and (4) ionizer [Cleg 89]. A schematic diagram of the TUNL ABPIS is shown in Fig. 3.5.

The dissociator mainly consist of a 1 cm-diameter Pyrex tube. Deuterium-gas molecules entering the tube are dissociated by an RF discharge. Atomic recombination is minimized by bringing the deuterium gas in thermal contact with a cooled copper nozzle. The nozzle is kept at 30 K and coated with high purity nitrogen gas to minimize recombination of atoms into molecules. The gas coming out of the nozzle has a highly

directional velocity with supersonic characteristics. The center part of the jet is directed through a collimator or a "skimmer" placed 21 mm away from the nozzle.

Next, the atomic beam is passed through a system of two sextupole magnets and a set of transition units to obtain the desired beam polarization. In the first sextupole magnet the atomic beam with the states (1, 2 and 3 with m_j=1/2) are selected, while others with m_j=-1/2 are deflected away from the magnet axis.

The nuclear polarization is then induced using two successive sextupole magnets and a set of transition units. Fig. 3.6 shows the selection of the magnetic substates through the source. The electron-polarized atomic beam enters a strong field (85G) transition unit (called SF1) where the transition 3 → 5 is induced. The resulting beam is composed of states 1, 2 with m_j = 1/2 and state 5 with m_j = -1/2. A second sextupole magnets follows, where the state 5 is removed out of the beam leaving only 1 and 2 with m_I =1 and m_I =0 respectively. Next, depending on the spin direction required, an additional transition unit is used.

The $A_Y(\theta)$ measurements require the production of the vector beam polarization P_Z with theoretical maximum of P_Z = +1 for *spin-up* measurement, and P_Z = -1 for the *spin-down* measurement. This was achieved by using a combination of the following RF transition units. To obtain P_Z = +1 which make *spin-up*, another strong transition unit (called SF2) is used to induce the transition 2 → 6. The resulting beam is fully polarized in state m_I = 1. For *spin-down* (P_Z = -1), a weak transition unit (called WF2) uses a 5G field to make the transition 1 → 4. This gives a fully polarized beam in state m_I =-1. The beam then enter the ECR ionizer section.

The ionization of the polarized beam takes place in the plasma region of the electron-cyclotron-resonance (ECR) *ionizer*. The plasma is created in the ionizer from high purity nitrogen gas and is confined axially by mirror coils and radially by an axially symmetric field of a sextupole magnet. In the plasma region, electrons are stripped from their neutral atoms producing positive charged ions. A negative biased plate is used to extract the positive beam out of the ionizer region. The positively charged

beam is focused through a series of electrostatic lenses. Finally, the beam is converted to a negative ion beam by passing through a cesium vapor in the *cesium oven* . Here two electrons are picked up through charge exchange. The polarized negative beam is accelerated to 26 keV after which it passes through a Wien Filter where the spin quantization axis is rotated to the desired orientation. An additional acceleration of up to 50 keV, is applied to the beam before being transported to the tandem accelerator.

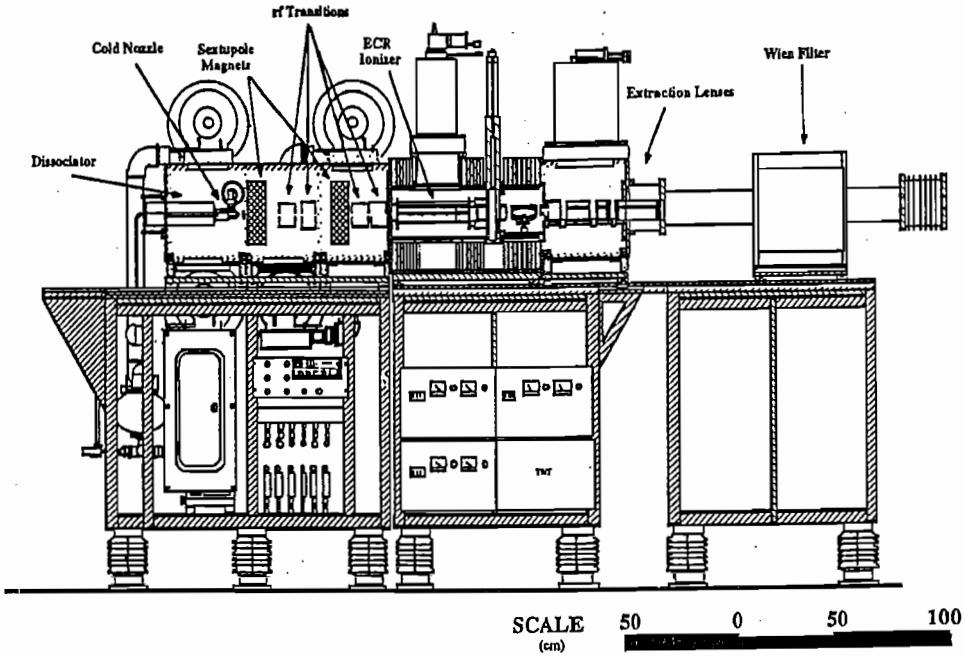

Figure 3.5. A schematic diagram of the ABPIS at TUNL.

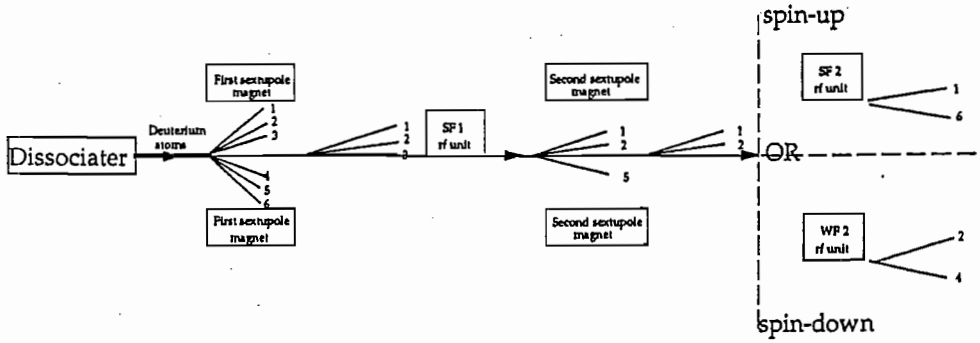

Figure 3.6. The selection of the magnetic substates through the source.

3.2.4 Spin Orientation and The Wien Filter

In the polarization experiments, it is important to align the spin quantization axis so that the spin of the polarized beam arrives at the reaction plane with the proper direction. This is achieved by a device called *Wien Filter* located after the ABPIS source.

The Wien Filter has magnetic and electric fields which are mutually perpendicular, and both at right angles with respect to the incident beam direction. Both fields can be varied in magnitude and orientation. The magnetic field is used to precess the spin of the particle, while the electric field is used to maintain the beam axis along the initial direction.

The coordinate system shown in Fig. 3.1 specifies the spin quantization axis and the reaction plane. The beam exits from the source with the quantization axis aligned at $\beta = 0^{\circ}$and $\phi = 0^{\circ}$. In order to measure the $A_y(\theta)$, as explained in Sect. 3.1.4, by utilizing the two spin directions, up and down, the quantization axis should be aligned initially at $\beta = 90^{\circ}$and $\phi = 0^{\circ}$.

As has been mentioned above, the substates $m_I = 1$ were selected by the SF2 transition unit while the WF2 transition unit produce the substates $m_I = -1$. Then switching between SF2 and WF2 gives the spin-up and spin-down direction, respectively. But during the course of the $A_y(\theta)$ measurement, the performance of the WF2 transition unit became poor (low polarization in spin down case), which led us to use only the SF2 unit and to flip the spin to the down direction by periodically rotating the Wien Filter through $\beta = -90^{\circ}$. Although this method turned out to be tedious and took more time, it ensured the same magnitude of the polarization for both spin directions.

3.2.5 Beam Polarization Measurement Using $^{12}C(\vec{n},n_o)$ reaction

The neutron beam polarization was determined by measuring the asymmetry from the $^{12}C(\vec{n},n_o)$ reaction at $\theta_{lab} = 50^{\circ}$. Tornow *et al* [Tor 87] have measured the analyzing power of this reaction at E_n=15.5 MeV with a 5% accuracy, using the same neutron source reaction $^2H(\vec{d},\vec{n})^3He$ reaction. Approximately every 8 h during the experiment, the two neutron detectors

were positioned at $\theta = 50^{\circ}$, and the carbon scatterer was placed in the sample-in position. The carbon sample is the same sample mentioned in Sect. 2.1.7. With the two detectors, data were taken for four configurations; with the sample in and out for both spin directions (up and down). Before utilizing the relation Eq. 3-17 between the scattering asymmetry, beam polarization and analyzing power, the measured scattering asymmetry must be corrected for finite geometry (see Sect. 3.3.2).

3.2.6 Data Acquisition

The data acquisition system used for the analyzing power measurements is similar to that used for $\sigma(\theta)$ measurements. The software PTOF was used on-line for data acquisition. The data was accumulated following the "two detector spin-flip" method. In this method both detectors were positioned at the same angle on both sides of the beam axis and the spin direction of the vector polarization of the incident neutron beam was periodically flipped up and down. This method eliminates most sources of instrumentally induced asymmetries. Four PTOF spectra for valid neutron events were accumulated in four 512 channel ADC's in two configurations. First, spectra were obtained at each angle from the *right* and the *left* detectors with the scattering sample in place (*sample-in* configuration) and then with the sample out of the neutron beam (*sample-out* configuration).

The neutron flux was monitored indirectly by measuring the deuteron beam current with a beam-current integrator (BCI) which gives the amount of charge deposited in the gas cell by the beam. The BCI gives one digital pulse per fixed amount of deposited charge. These pulses were counted by a scalar and stored in the computer.

3.3 DATA ANALYSIS

For each spin-direction of the incident polarized deuteron beam, the Polarized Neutron Time-Of-Flight (PNTOF) spectra were accumulated for the sample-in and the sample-out cases for the right and the left detectors. The two detectors were positioned symmetrically about the beam axis at a scattering angle θ. A "difference" spectra was generated for each detector and for each spin-direction. These spectra are the source of obtaining a single value of $A_y(\theta)$.

The analyzing power function as defined in Eq. 3-19 relating the scattering asymmetry $\varepsilon(\theta)$, and the neutron beam polarization P_n. The scattering asymmetry was determined at each angle from the four yields of Eq. 3-17. These yields were combined utilizing the "two- detector spin-flip" method as explained in Sect. 3.2.6. The advantage of this method is that most of the instrumental asymmetries are eliminated such as the relative efficiencies of the two detectors and the BCI for the two spins. Then using Eq. 3-18, the scattering asymmetry can be determined. Once the incident beam polarization P_n is calculated from the calibrated analyzing power of $^{12}C(\vec{n},n_o)$ reaction (see Sect. 3.3.2), the analyzing power $A_y(\theta)$ can be obtained through Eq. 3-19.

3.3.1 Neutron Yield Extraction

In order to discuss the determination of the scattering asymmetry, it is necessary to discuss the method of spectra reduction and background determination. A data analysis package called PTOFOFF similar to NTOFOFF was used in the data analysis. The steps followed to extract the neutron yield were carried out in the following order:

i) *Difference spectra:* In the analyzing power measurement there exist sample-uncorrelated counts (sometimes called "room background"). These events were caused by the scattering of neutrons from the experimental apparatus (i.e., floor, walls, detector shields, etc.) and the air in the vicinity of the sample. To eliminate most of these sample-uncorrelated counts

appearing in the spectrum, a difference (DIFF) spectrum was generated for spin-up and spin-down, for each detector. The DIFF spectra were calculated by subtracting the sample-out (OUT) spectrum from the corresponding sample-in (IN) spectrum after scaling the OUT spectrum with the ratio of the total BCI charge collected on the beam stop during the IN and the OUT runs:

$$\text{DIFF} = \text{IN} - \text{OUT} \times \frac{(\text{BCI})_{\text{IN}}}{(\text{BCI})_{\text{OUT}}}, \qquad (3\text{-}20)$$

where $(\text{BCI})_{\text{IN}}$ is the sample-IN integrated beam current and $(\text{BCI})_{\text{OUT}}$ is the sample-OUT integrated beam current.

ii) Background determination: Although most of the apparent background in the four spectra is accounted for by the sample-out measurement, some unwanted sample-correlated background counts remained in the DIFF spectra. These background counts are caused by neutrons which scatter from the sample and then scatter from various objects (such as the shadow bars and the collimator) on the their way to the detectors. The background level in the regions alongside the peak of interest needs to be examined to approximate these counts. In order to determine the best way to approximate the level of these counts, some tests were conducted to examine this non-subtracting background. A set of windows was chosen for the elastic peak in the UP and DOWN spectra accumulated by each detector. In setting these windows two things were considered: *First*, because windows in both the UP and the DOWN spectra are the same, it was helpful to superimpose the two spectra to determine a suitable location for identifying a suitable background region. Within statistical uncertainties the background had the same level for both the spin-up and the spin-down spectra and could be approximated adequately by a linear function. Also, no evidence of a polarized background was found. *Second*, narrow windows were used to define the counts in the peak of interest; this allows one to improve statistical uncertainties in neutron scattering yields by enhancing the signal-to-noise ratio.

Figs. 3.7 and 3.8 show time-of-flight DIFF spectra from the polarized neutron measurements for ^{28}Si at $\theta_{lab}=66^\circ$ for spin-up and spin-down,

respectively. The windows used for defining the elastic peak and the background are indicated in the figure.

iii) Yield & Asymmetry Calculation: After the determination of the background, three sets of windows were set on each side of the elastic peak at 10%, 20% and 50 % of the full peak height. For each case a yield was generated for the right detector spin-up (R_u), right detector spin-down (R_d), left detector spin-up (L_u), and the left detector spin-down (L_d). The yields were calculated by summing the counts in the channels within the peak windows and above the background curves. To ensure the proper background assignment and to avoid any contaminants from unresolved states near the peak, all the three yields were examined but only the 20% yield was used in the calculation.

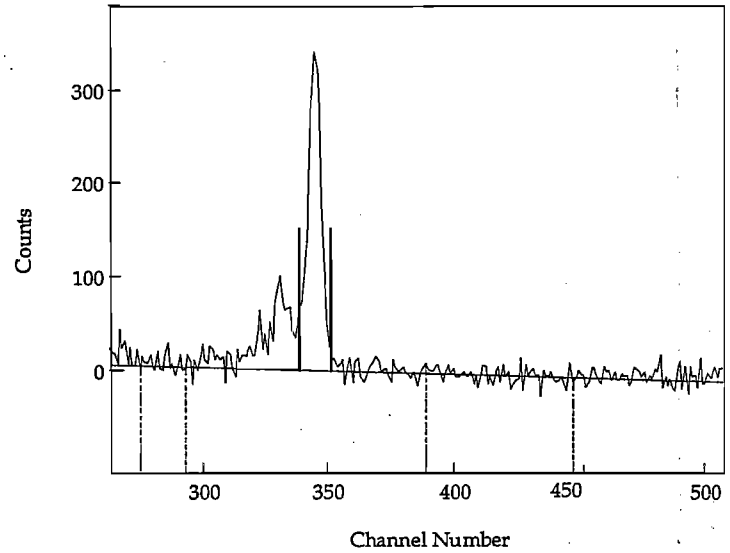

Figure 3.7. The time-of-flight DIFF spectrum for the scattering of 15.5 MeV polarized neutron from ^{28}Si for *spin-up* at θ_{lab}=66°. The two solid lines indicate the window used for summing the yield, while the dashed lines indicate the estimated background. Note the offset for zero counts.

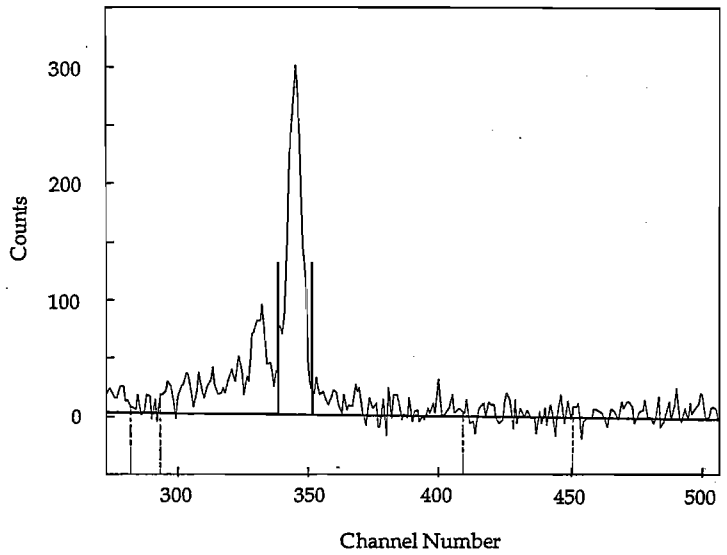

Figure 3.8. The time-of-flight DIFF spectrum for the scattering of 15.5 MeV polarized neutron from ^{28}Si for *spin-down* at θ_{lab}=66°. The two solid lines indicate the window used for summing the yield, while the dashed lines indicate the estimated background. Note the offset for zero counts.

3.3.2 Beam Polarization Calculation

As mentioned in Sect. 3.2.5, the neutron beam polarization P_n was determined using the $^{12}C(\vec{n},n_o)$ reaction. From the DIFF spectra of all the ^{12}C runs, the scattering asymmetry at θ=50° was determined. The measured scattering asymmetry gave the experimental scattering asymmetry with finite geometry $\varepsilon_f^e(\theta)$. In order to use Eq. 3-19, the experimental analyzing power for finite geometry $A_f^e(\theta)$ must be calculated. This was done utilizing the code JANE with the exact experimental conditions in order to simulate the experiment. This method yields the required analyzing power as will be explained in Sect. 3.3.4. The average neutron beam polarization was determined to be 54%. We assign a 3% absolute uncertainty to this value. The uncertainty originated mainly in the uncertainty in the ^{12}C analyzing power as determined by Tornow et al. [Tor 87].

3.3.3 Finite Geometry Corrections

As discussed in Sect. 2.3.3, it is necessary for the analyzing power data to be corrected for the effects of finite geometry, flux attenuation, and multiple scattering. These corrections were calculated for the analyzing power measurements using a Monte-Carlo simulation code JANE. A full description of the code can be found in [Woy 81] and [Hon 83]. The final correction to the A_y (θ) data is calculated using an iterative method. The ultimate aim of JANE is to determine the analyzing power for single scattering for point geometry at a mean scattering angle $\theta_{c.m.}$.

Before using JANE, a scattering library was constructed for ^{28}Si scattering and ^{32}S scattering separately. Each library consisted of differential cross section, analyzing power and total cross section at several energies within the full energy range available to the scattered neutrons. The data used in each library were obtained from [How 84, Tai 82]. Included in this library, as a first approximation to the A_y (θ) library, was the experimental (raw) A_y (θ) which needed to be corrected. After each iteration, the A_y (θ)

library was updated by fitting the newly corrected A_y (θ) data with an associated Legendre polynomial using the code MACRO and then update the library with the coefficients of the associated Legendre polynomial expansion. In addition to the library, details of the experiments must be supplied to JANE as input. These details include the incident deuteron energy, gas cell pressure, detector flight path and the dimension of the gas cell, sample and detector.

The uncorrected analyzing power obtained in the measurement is a weighted average of the single and the multiple scattering and is related as:

$$A^T = P^S A^S + P^M A^M, \tag{3-21}$$

$$F = A_P^S(\theta_P) - A_f^S(\theta_f), \tag{3-22}$$

where

A^T, A^S, A^M are the analyzing power for total, single, and multiple scattering, respectively.

P^S, P^M are the probabilities of single and multiple scattering in the sample, respectively.

A_P^S, A_f^S are the single-scattering analyzing powers for point geometry and for finite geometry, respectively, and

F is the finite geometry correction.

The correction process of JANE is based on the Monto Carlo technique. Using the experimental geometries, JANE simulates the experiment by randomly generating numbers of "neutron histories". A neutron history is a set of locations with one location in the gas cell, one or two locations in the sample and a location in the detector. The code JANE traced 10,000 single-scattering histories and 25,500 multiple-scattering histories. This amount provides an even distribution of scattering events in all three volumes. This is done by randomly generating numbers of "neutron histories". A neutron history is a set of locations with one location in the gas cell, one or two locations in the sample and a location in the detector. The code JANE traced 1000 single-scattering histories and 6,500 multiple-scattering histories. This amount provides an even distribution

of scattering events in all three volumes. From these neutron histories and for each scattering angle, simulated TOF spectra for both detectors are generated for spin up and spin down, for single and multiple scattering. The code then uses these spectra to calculate A^T, P^S,P^M and F.

The uncorrected experimental data along with the quantities calculated in JANE are input to another program CORE (a program associated with JANE). Using Eqs. 3-21 and 3-22, CORE calculate the first estimate for the single scattering analyzing powers. To improve the estimation, the corrected single scattering data is used to update the analyzing power library. A second iteration of JANE was performed and then the new corrected data is compared to the corrected data from the previous iteration. If agreement within 1% was found then convergence is achieved and the point-geometry, single-scattering data has been obtained. If the values disagree by more than 1%, another iteration of the code was needed, starting with a new update to the library data from the last iteration. For both correction of ^{28}Si and ^{32}S data, three iterations of JANE were performed. However, two iterations were sufficient to achieve the 1% convergence criterion.

Figs. 3.9 and 3.10 show the experimental uncorrected data and the final corrected values for ^{28}Si and ^{32}S, respectively, at the mean neutron energy of 15.5 MeV. The uncorrected and the corrected values for ^{28}Si and ^{32}S are listed in appendices A-5 and A-6, respectively. Typically, the effect of the multiple scattering is to lower the magnitude of the analyzing power from the single-scattering value. The largest corrections are in the region of the $\sigma(\theta)$ minima. These large corrections are also reflected in the large angle shift between the central value in the lab and the determined mean scattering angle for point scattering and the increase of the uncertainties applied to the data.

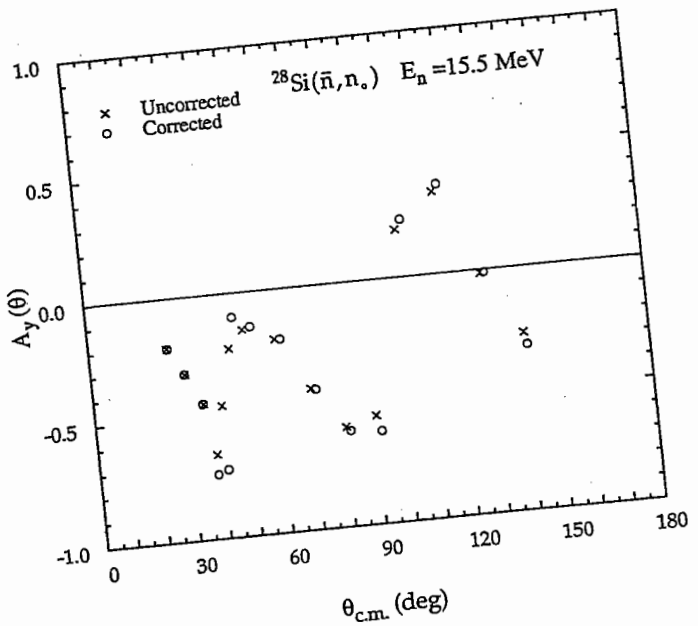

Figure 3.9. The Ay (θ) data for elastic neutron scattering from ^{28}Si at 15.5 MeV. The open circles (O) are the corrected data, while the × 's are the values before the finite geometry corrections.

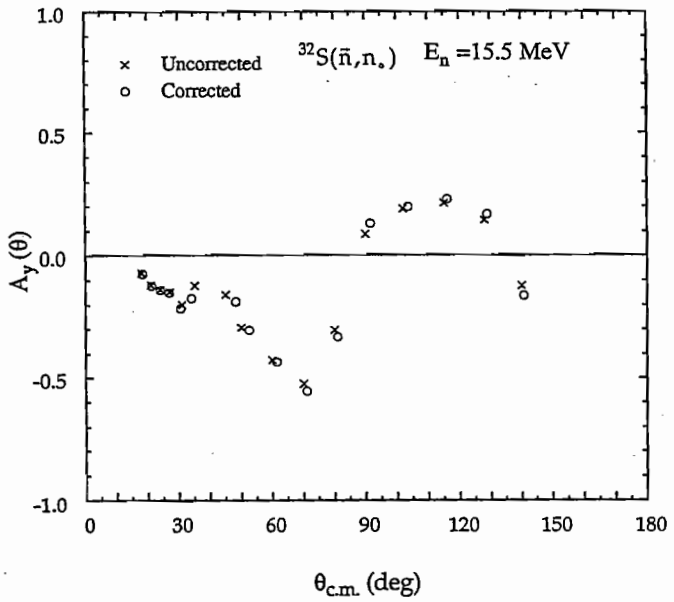

Figure 3.10. The A_y (θ) data for elastic neutron scattering from ^{32}S at 15.5 MeV. The open circles (O) are the corrected data, while the × 's are the values before the finite geometry corrections.

Special attention was given to the correction at the first minimum (near 40°) of the $A_y(\theta)$ in ^{28}Si. This was done in order to study the influence of variations in the library on the final extracted $A_y(\theta)$ values at this sharp-structure region. When the finite-geometry corrections are applied to the experimental data, the structure is enhanced because the finite geometry in the experiment causes the structure of the $A_y(\theta)$ to smooth out. The sensitivity of the corrections for the data points at θ_{lab} = 38° and 41° were examined by creating two unphysical libraries for $A_y(\theta)$. In the first library, library-A, the value at 38° was increased by 25% and the value at 41° was decreased by the same percentage. For the second library, library-B, the value at 38° was decreased by 25%, and the value at 41° was increased by the same percentage. These modifications to the library are shown in Fig. 3.11 with the associated Legendre polynomial fits of the corresponding two libraries. The final iteration of the code JANE was reapeted for each library case with the corresponding updated library. The results of the calculations would prove how much the final values shift with the changes in the library. It was found that the changes to the resulting analyzing power data, were within 2% of the final quoted values in appendix A-5.

The uncertainties in the $Ay(\theta)$ data are summarized in Table 3-2. In both the ^{28}Si and ^{32}S cases, the data have relative uncertainties ranging between 2% (at forward angles) and 7% (near the minimum of the $\sigma(\theta)$). These relative uncertainties include statistical errors from sample yields and the background subtraction, and errors from the finite geometry corrections from the JANE simulation. There were two normalization (or scale) uncertainties. The first was due to the uncertainties in the determination of the deutron beam polarization and it was about 2%. A second scale uncertainty (5%) was assigned to the analyzing power of the ^{12}C(n, n) reaction that was used to determine the neutron beam polarization. Error bars listed with the data in appendices A-5 and A-6, and shown in the figures include the relative uncertainties only. In a future experiment it will be possible to reduce the uncertainty in the ^{12}C(n, n) analyzing power and then to specify more accurately the scale factor.

Table 3-2 Summary of sources of Uncertainties for A_y measurement.

SOURCE	VALUE
A. Relative Uncertainties	
Yield and Background subtraction	2 - 7 %
Finite Geometry Correction	1 %
B. Normalization Uncertainties	
Deuteron Beam Polarization	2 %
The A_y of ^{12}C (analyzing reaction)	5 %

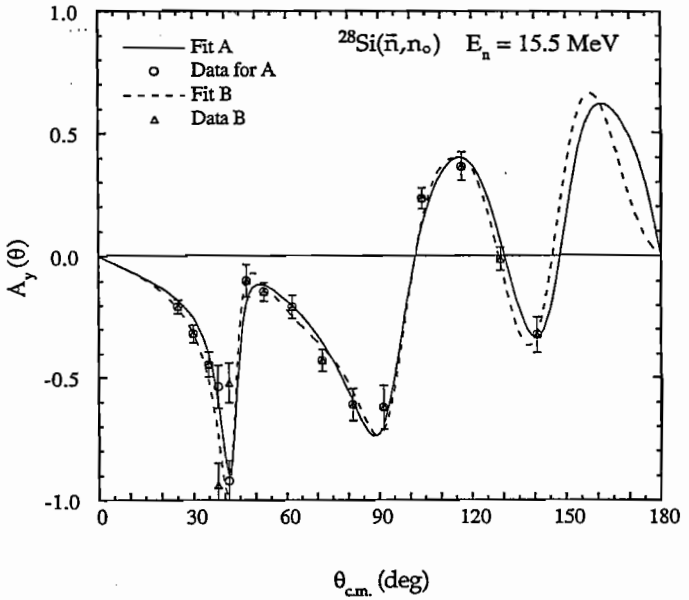

Figure 3.11. The two libraries (Fit A and Fit B) used to examine the sensitivity of the finite geometry corrections for the A_y (θ) values near the minimum at 40°. The symbols indicate the values used to generate the polynomial fits.

3.3.4 Presentation of the Data

The fit to the $A_y(\theta)$ data followed the conventional method of first multiplying the A_y values by $\sigma(\theta)$. As discussed in Sect. 2.3.5, the product $A_y(\theta)\cdot\sigma(\theta)$ can be expressed as an associated Legendre polynomial expansion of the following form:

$$A_y(\theta)\cdot\sigma(\theta) = \sum_{l=1}^{n} b_l \cdot P_l^1(\cos\theta), \qquad (3\text{-}23)$$

where the b_l are the coefficients of the associated Legendre polynomials.

The corrected analyzing power data for ^{28}Si and ^{32}S at a neutron energy 15.50 MeV are shown in Fig. 3.12 and Fig. 3.13, respectively. A tabulation of the data for ^{28}Si and ^{32}S along with the coefficients of the expansion is given in appendices A-5 and A-6, respectively. The $A_y(\theta)$ fits shown in the above figures were obtained first by fitting the associated Legendre polynomials to the product $A_y(\theta)\cdot\sigma(\theta)$ and then dividing the fit of the product by $\sigma(\theta)$ alone. The final values of $\sigma(\theta)$ of Sect. 2.2.4 were used in Eq. 3-20.

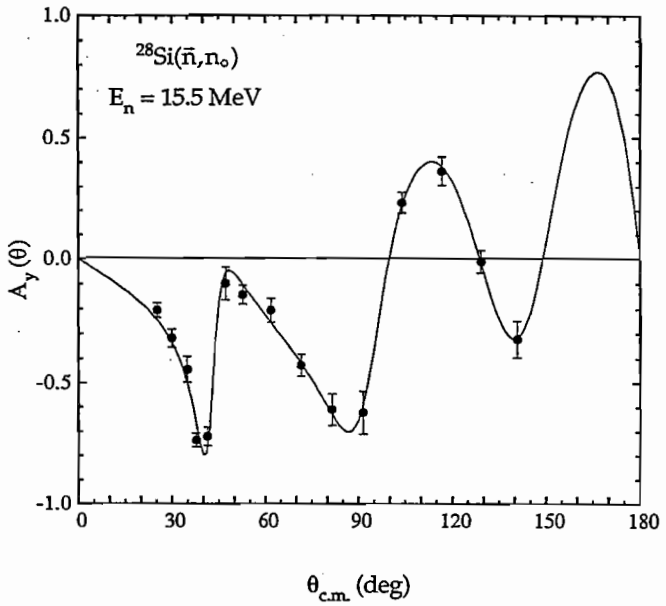

Figure 3.12. The $A_y(\theta)$ data for elastic neutron scattering from ^{28}Si at 15.5 MeV. The curve is a fit derived from an associated Legendre polynomial fit to the product $A_y(\theta)\cdot\sigma(\theta)$ (see text).

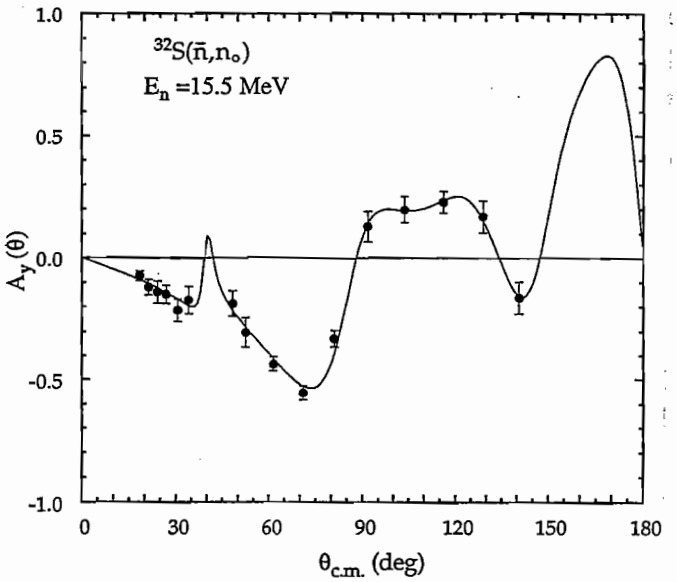

Figure 3.13. The $A_y(\theta)$ data for elastic neutron scattering from ^{32}S at 15.5 MeV. The curve is a fit derived from an associated Legendre polynomial fit to the product $A_y(\theta) \cdot \sigma(\theta)$ (see text).

CHAPTER 4

Database
&
Compound-Nucleus Corrections

4.1 Database

One of the main objectives of this project is to develop a valid neutron-nucleus optical-model parameterization for the ^{28}Si and ^{32}S nuclei capable of describing $\sigma(\theta)$, $A_y(\theta)$ and σ_T in the positive-energy region (scattering region), as well as predicting the bound-state properties in the negative-energy region, commonly studied via the shell-model potential. Hence, it is necessary to have a fairly wide energy range of data in both regions (i.e., the positive and negative energy regions). In the positive-energy region, the data base consisted of $\sigma(\theta)$, $A_y(\theta)$ and σ_T data from the present work and from other data experiments both at TUNL and other labs. The energy range for $\sigma(\theta)$ extended from 2 to 40 MeV, for $A_y(\theta)$ from 10 to 17 MeV and for σ_T from 0.3 to 80 MeV. Tables 4.1 and 4.2 list the scattering data base used in developing the dispersive optical-model (OM) parameterization for ^{28}Si and ^{32}S, respectively.

Table 4.1. Database used to develop the dispersive OM for n+^{28}Si

E_n(MeV)	$\sigma(\theta)$	$A_y(\theta)$	σ_T	Reference
0.2 — 50.0			√	[Kin 72]
0.5 — 32.0			√	[Cie 68]
1.7 — 6.0			√	[Koe 87]
2.0 — 81.0			√	[Lar 81]
2.3 — 15.0			√	[Fos 71]
1.95	√			[Bre 64]
2.45, 2.85	√			[Pet 60]
4.0, 6.0, 6.7	√			[Dra 69]
4.8	√			[Tsu 61]
5.95	√			[Mar 68]
8.0, 12.0	√			[How 84]
10.0, 14.0, 17.0	√	√		[How 84]
11.0, 20.0, 26.0	√			[Tai 82]
14.8	√			[BLC 82]
15.5	√	√		present work
19.0	√			present work
30.3, 40.0	√			[DeV 83]

Table 4.2. Database used to develop dispersive OM for n+^{32}S

E_n(MeV)	$\sigma(\theta)$	$A_y(\theta)$	σ_T	Reference
0.2 — 3.55			√	[Fil 68]
0.5— 32.0			√	[Cie 68]
2.3 — 15.0			√	[Fos 71]
3.0 — 5.0			√	[Tsu 63]
2.45, 2.85, 5.8	√			[Pet 60]
5.95	√			[Mar 68]
7.6	√			[Vir 81]
8.0, 12.0,	√			[How 84]
10.0, 14.0, 17.0	√	√		[How 84]
11.0, 26.0	√			[Tai 82]
14.8	√			[BLC 82]
15.5	√	√		present work
19.0	√			present work
21.7	√			[Ala 86]
30.3, 40.3	√			[DeV 83]

For the negative-energy region, the empirical information needed are the neutron bound-state energies. These are the energies of the neutron single-particle and single-hole states. The information about the bound states is usually obtained from one-neutron transfer reactions; stripping reactions and pickup or knockout reactions. The stripping reactions are used to obtain the particle states while the pickup or knockout reactions are employed for the hole states. The method to construct the bound-state information for the nucleus of interest is explained in the following example. If a neutron is added (or taken out, creating a hole) to a nucleus with mass number A, a system A+1 (or A-1) is formed. Then, the ground state of the (A+1)-nucleon system can be viewed as the ground state of the nucleus A with a neutron added to an exited state [Mah 91], thus forming single-particle states which are located above the Fermi energy. The energies of these particle states are equal to the Fermi energy (E_F) of the nucleus A plus the associated separation energies. In a similar way, the (A-1)-nucleon system can be viewed as the ground state of the nucleus A with a neutron taken out of an exited state to form single-hole states which are located below the Fermi energy. The energies of these hole states are equal to E_F of A minus the associated separation energies.

The Fermi energy is identified as the average of the seperation energy of the A-nucleon system (E_F^-) and the seperation energy of the (A+1)-nucleon system (E_F^+) [Mah 91].

$$E_F = \frac{1}{2}\left(E_F^- + E_F^+ \right) \qquad (4\text{-}1)$$

In the case of ^{28}Si and ^{32}S, the Fermi energies were calculated as the following:

$$\text{For } ^{28}\text{Si} \quad E_F = \frac{1}{2}\left(^{28}\text{Si} + ^{29}\text{Si} \right) = \frac{1}{2}\left(-17.177 + -8.474 \right) = -12.826 \text{ MeV} \qquad (4\text{-}2)$$

$$\text{For } ^{32}\text{S} \quad E_F = \frac{1}{2}\left(^{32}\text{S} + ^{33}\text{S} \right) = \frac{1}{2}\left(-15.088 + -8.643 \right) = -11.866 \text{ MeV} \qquad (4\text{-}3)$$

In addition to the bound-state energies, one can obtain single-particle and single-hole spectroscopic information from the reactions mentioned above. However, such information is easier to extract from (e,e' nucleon) measurements than from (d,p) or (p,d) reactions because the (e,e') process is better understood (i.e., an EM interaction).

However, the extraction of bound-state information from experimental data is considerably more difficult than the fitting of data in the scattering region. In many cases the deformation of a nucleus such as ^{28}Si or ^{32}S causes the particle and hole states to be fragmented. This fragmentation leads to difficulties in determining the centroid energies of the states. Nevertheless, we used as much information from the literature as could be obtained from stripping reactions, pickup reactions and electron scattering. Table 4.3 lists the sources of the empirical information used in our bound-state studies for extending the OM into the negative energy region.

In some cases, the information available was only for proton bound states rather than neutron bound states. In such cases, the neutron separation energy for ^{28}Si and ^{32}S should be added to give the neutron particle or hole states. The neutron separation energy used for the ^{28}Si data was 5.6 MeV and that for the ^{32}S data was 6.2 MeV [Wie 86, NDT 71].

Table 4.3. Empirical information on single-particle states for n-^{28}Si and n-^{32}S.

Nucleus	Particle States	Hole States	Reference
Silicon		(e,e'p)	Saclay [Fru 84]
	^{28}Si(d,p)^{29}Si		[Bol 64]
Sulfur		(e,e'p)	Saclay [Fru 84]
	^{32}S(d,p)^{33}S	^{32}S(d,p)^{33}S	[Spi 65]

4.2 Compound-Nucleus Correction

4.2.1 Introduction

The nuclear reactions can be classified either as *compound-nucleus* (CN) reactions or *direct reactions*. When an incident particle is absorbed by a target nucleus, a compound system is formed. In this compound system, the energy of the incident particle is shared with a number of nucleons in the system and the identity of the incident particle is lost. After a time (~10^{-14} s) long compared with the nuclear transit time (~10^{-23} s), the compound nucleus decays into energetically allowed reaction channels. In general, the CN dominates in the low energy region (E<3 MeV) and becomes negligible above 12 MeV.

The direct reactions, which are instantaneous processes, occur when the incident particle interacts with the target nucleus (primarily at the surface) in a very short time (<10^{-22} s). In direct processes, generally the interaction involves one or very few nucleons without forming a compound nuclear system.

The measured elastic differential cross section σ_{el}^{meas} can be considered as composed of two contributions [Sat 90]. One part σ_{el}^{SE} is due to the direct interaction (sometimes called shape-elastic scattering) and the other contribution σ_{el}^{CN} is due to the compound-nucleus reaction. These two contributions cannot be separated experimentally. However, the shape-elastic cross section can be determined from:

$$\sigma_{el}^{meas} = \sigma_{el}^{SE} + \sigma_{el}^{CN} \qquad (4\text{-}4)$$

In the present work an OM is developed (see Chap. 5) to describe the ^{28}Si(n,n$_0$) and ^{32}S(n,n$_0$) differential cross sections in the energy range from 2 - 40 MeV. Since the OM can account only for the direct contribution, the CN contribution must be removed from the experimental data before developing the model. Eq. 4-4 is used to obtain σ_{el}^{SE} for differential cross sections of ^{28}Si and ^{32}S.

What follows next is a brief discussion of the compound-nucleus reaction theory and the method that we followed to apply the CN corrections to the measured differential cross-section data.

4.2.2 Compound-Nucleus Cross Section

When a compound nucleus is formed, there are many possible channels (exit channels) through which the compound system can decay. The cross sections of these exit channels are, on the average, smoothly varying functions of the incident neutron energy [Sat 90]. Such smooth behavior suggests that the use of a statistical model to calculate these cross sections is appropriate. The statistical model used for compound nucleus formation was developed by Hauser and Feshbach [Hau 52].

We will next present a brief outline of the main concepts of the statistical model. For a lengthy discussion and derivation of the statistical model, the papers [Gol 63], [Hod 71] and [Mar 71] are recommended. In addition, Howell [How84] gave an excellent summary of the CN formalism applied to neutron scattering of the Si and S nuclei.

The treatment of the CN in Hauser-Feshbach theory has three main characteristics or assumptions: (1) The absence of any dependence between the modes of formation and decay of the CN; this is called the "independence hypothesis". (2) The probability of formation must equal the sum of the decay probabilities for all exit channels. (3) The reciprocity relation holds in the CN reactions; i.e., time-reversal invariance holds.

Let the cross section for forming a compound nucleus N through an incident channel α be represented by σ_α. Then, N decays through a particular exit channel β. The reaction cross section for the process going from channel $\alpha \rightarrow$ channel β is given by:

$$\sigma_{\alpha\rightarrow\beta} = \sigma_\alpha P_\beta , \tag{4-5}$$

where σ_α is the cross section for forming the CN through channel α, and P_β is the probability that the CN will decay through channel β. Under the time-reversal of the inverse reaction, the cross section from $\beta\rightarrow\alpha$ is related to the one from $\alpha\rightarrow\beta$ through a constant. The relationship is given by:

$$\sigma_{\beta\rightarrow\alpha} = \left(\frac{\lambda\!\!\!^{-}_\beta}{\lambda\!\!\!^{-}_\alpha}\right)^2 \bullet \sigma_{\alpha\rightarrow\beta} \ . \tag{4-6}$$

Rewriting Eq. 4-6 in terms of transmission coefficients T_α and T_β and using the reciprocity relation $T_\beta P_\alpha = T_\alpha P_\beta = T_\alpha T_\beta / \sum_\gamma T_\gamma$, where the sum $\sum_\gamma T_\gamma$ is evaluated over all possible exit channels, yields:

$$\sigma_{\alpha\rightarrow\beta} = \pi\lambda\!\!\!^{-2}_\alpha \frac{T_\alpha T_\beta}{\sum_\gamma T_\gamma} \ . \tag{4-7}$$

Here $\lambda\!\!\!^{-}$ is the reduced wavelength of the incident particle.

Eq. 4-7 is the simple form of the Hauser-Feshbach model. To be more exact a width fluctuation correction factor $W_{\alpha\beta}$ was introduced [Mol 64] into Eq. 4-7. This factor is greater than unity for the elastic cross-section channel and less than unity for inelastic cross sections since the elastic cross section is enhanced relative to all other cross sections due to the correlation in the fluctuations in the widths of the entrance and exit channels [Gri 69]. The width-fluctuation correction factor has the form [Gru 77]:

$$W_{\alpha\beta} = \left\langle \frac{\Gamma_\alpha \Gamma_\beta}{\sum_\gamma T_\gamma} \right\rangle \Bigg/ \frac{\langle \Gamma_\alpha \rangle \langle \Gamma_\beta \rangle}{\left\langle \sum_\gamma T_\gamma \right\rangle} \ . \tag{4-8}$$

4.2.3 The CN Reactions for n+^{28}Si and n+^{32}S

The possible exit-channel reactions included in the calculation of the CN elastic cross section for ^{28}Si and ^{32}S are listed in Table 4.3 .

Table 4.4. Decay scheme of the CN for the Silicon and Sulfur.

Initial Channel	Comp. Nucleus	Exit Channel	Q-value	Ref. for OM parameters
^{28}Si + n	$\rightarrow ^{29}$Si	$\rightarrow ^{28}$Si + n	0.00	[How 84]
		$\rightarrow ^{28}$Al + p	-3.85	[Per 63A]
		$\rightarrow ^{27}$Al + d	-9.36	[Per 63B]
		$\rightarrow ^{25}$Mg + α	-2.65	[Duh 68]
		$\rightarrow ^{29}$Si + γ	8.48	Default*
^{32}S + n	$\rightarrow ^{33}$S	$\rightarrow ^{32}$S + n	0.00	[How 84]
		$\rightarrow ^{32}$P + p	-1.04	[Per 63A]
		$\rightarrow ^{31}$P + d	-6.64	[Per 63B]
		$\rightarrow ^{29}$Si + a	1.53	[Duh 68]
		$\rightarrow ^{33}$S + γ	8.07	Default*

* Default parameters are provided by the code HAUSER*5.

4.2.4 Method of Correction

The shape-elastic differential cross section is the difference between the experimental data and the CN contribution:

$$\sigma_{el}^{SE}(\theta) = \sigma_{el}^{meas}(\theta) - \sigma_{el}^{CN}(\theta) \ . \qquad (4\text{-}9)$$

The shape-elastic analyzing power is given as:

$$A_y^{SE}(\theta) = \frac{\sigma_{el}^{meas}(\theta)}{\sigma_{el}^{SE}(\theta)} A_y^{meas}(\theta) \qquad (4\text{-}10)$$

In Eq. 4-10, there is no contribution from the CN analyzing power, because the spin information for the CN is averaged over all channels which cause the CN to lose its initial polarization. This makes $A_y^{CN}(\theta) = 0$.

The CN cross sections were calculated using the code HAUSER*5 [Man 79]. The code can calculate the reaction differential cross section with

a maximum of six reaction exit channels and with an incident energy up to 60 MeV. The Hauser-Feshbach theory relates the average CN cross section for a reaction to the transmission coefficients for all exit channels. To evaluate $\sigma_{\alpha\rightarrow\beta}$ in Eq. 4-2, the transmission coefficients need to be calculated. These coefficients are usually obtained from the optical model calculation. The code gives the user the option to use default OM parameters included in the code or supply the parameters. For the present work, the references for the optical-model parameters used for each reaction channel are listed in Table 4.3.

In order to evaluate the sum of the transmission coefficients over all exit channels, a level density formula was used for modeling the continuum of exited states for excitation energies up to 10 MeV. To estimate the level density $\rho(E)$ at the excitation energy (E), the constant-temperature approach was used

$$\rho(E) = \frac{1}{T} \exp \frac{(E - E_o)}{T} \qquad (4\text{-}11)$$

where T is the nuclear temperature, and E_o is the pairing energy. The level-density parameters used in the calculation were obtained from Gilbert and Cameron [Gil 65].

In this work, the energy range of the scattering cross-section database, was extended down to 2.45 MeV, as can be seen from Table 4.1. At such a low energy, the CN contribution is significant. Therefore, CN corrections must be applied to the measured cross sections in order to obtain data that can be used in the determination of the optical-model parameters. The above correction methods (Eqs. 4-9 and 4-10) for the CN contribution were applied to all data below 14 MeV.

Table 4.5. Level density parameters used for CN calculation

Nucleus	E_o (MeV)	T (MeV)
^{28}Si	3.20	2.09
^{28}Al	-0.70	1.5
^{27}Al	-0.35	2.08
^{25}Mg	-1.00	2.12
^{29}Si	0.75	1.91

Nucleus	E_o (MeV)	T (MeV)
^{32}S	1.75	2.05
^{32}P	-1.75	1.96
^{31}P	0.40	1.78
^{29}Si	0.75	1.91
^{33}S	0.00	1.68

CHAPTER 5

The Nuclear Mean Fields of ^{28}Si and ^{32}S

The Nuclear Mean Fields of ^{28}Si and ^{32}S

In this chapter we discuss the application of the DR and the optical model to derive the nuclear mean field for neutrons in ^{28}Si and ^{32}S. The concept of the nuclear mean field is first explained, then the historical application of the DR and the formulation of the Dispersive Optical Model (DOM) are discussed. The results of the DOM analyses of n-^{28}Si and n-^{32}S are then presented.

5.1 Nuclear mean field

The one-body potential between a nucleon and a nucleus is a concept that has a central unifying role in the interpretation of much nuclear structure information and reaction properties. One can describe the neutron-nucleus interaction approximately by a complex mean field, composed of real ($\mathcal{V}$)and imaginary ($\mathcal{W}$) parts

$$\mathcal{M}(r;E) = \mathcal{V}(r;E) + i\mathcal{W}(r;E). \qquad (5\text{-}1)$$

Here r denotes the displacement from the nuclear center and E denotes the neutron energy. For $E > 0$, $\mathcal{M}$ is called the optical-model potential and is used for the description of scattering cross sections. For $E < 0$, $\mathcal{V}$ is called the shell-model potential and is used to describe the single-particle and single-hole states.

It is worth mentioning that the nuclear mean field (NMF) is not an observable. It is just a theoretical concept introduced in the framework of the shell model and the optical model. The main purpose of introducing the NMF concept is to obtain some global properties of V(r;E) of the mean field from the phenomenological analyses of the experimental data. The approximate validity of the shell and optical models makes it possible to obtain these global properties [Mah 85].

Although the NMF varies smoothly as the neutron energy changes sign, its energy dependence is complicated in the region of the Fermi

energy, which lies between the occupied and unoccupied single-particle states at negative energies (see Sect. 4.1). This behavior can be traced to the coupling between the elastic channel and inelastic channels, the latter of which is responsible for the existence of the imaginary part $\mathcal{W}$ in the mean field [Mah 86]. (As in the analog with light waves, the imaginary part in the optical model is included to account for the flux removed from the elastic channel by non-elastic processes.) A connection between the real and the imaginary part can be obtained through the DR (see Eq. 5-5 and the description in Sect. 5.4).

The DR was derived from the basic concept of causality and from the analytical properties of the mean field. Mahaux *et al.* [Mah 86 A] presented a mathematical derivation of the DR. Earlier, Ericson and Locher [Eri 70] discussed the validity of the DR from the casualty principle.

5.2 Historical application of the DR

The DR has been known in physics for some time; it was first introduced by Kramers and Kronig [Kro 26] in the analysis of light scattered from an absorptive medium. But only in recent years have the experimental data for nucleon-nucleus scattering achieved the precision that enables them to be fully utilized. In this section a brief history is presented for some of the main applications of the DR in the field of the nuclear reactions. This presentation focuses on the different applications, and is not intended to list all work that has been done in this growing field.

In 1967, Passtor [Pas 67] tried to determine how much the local-energy-dependent approximation is due to the true dispersive character of nuclear matter and how much is due to the hypothesis of locality. In his analysis, there was no distinction between neutron or proton data. Lipperheide and Schmidt in 1968 [Lip 68] used the DR to study the energy-dependence of the phenomenological OMP for proton scattering from ^{40}Ca, ^{13}C and ^{58}Ni. The first specific application of the DR to the analysis of the phenomenological OMP was carried out by Ahmad and Haider [Ahm 76]. They attempted to use the DR to calculate the surface-peaked component of the real potential in the scattering of protons from ^{40}Ca. However, they did not include the dispersive volume contribution ΔV_V (which is defined and discussed in the next section).

The real boost of the DR utilization came after the work of Mahaux and Ngô in 1981 [Mah 81] [Mah 82], where they derived the integral subtracted form of the DR and applied it to their work on nuclear matter theory. The advantage of using the subtracted form is the convergence of the dispersion integral that can be achieved at higher energies. Since then, Mahaux and Sartor have done extensive work utilizing the DR to derive the properties of the nuclear mean field by extending the OMP to negative energy, predicting the bound states of n+^{40}Ca and n+^{208}Pb [Mah 86B] [Mah 87] [Mah 88] [Mah 89]. In a different study [Mah 86A], they applied the DR to investigate the threshold anomaly of the nucleus-nucleus potential. Smith *et al.* used the DR to study the energy-dependence of the real potential from neutron scattering from ^{93}Nb [Smi 86] and from ^{209}Bi [Law 87]. Another

important and detailed analysis of the interaction of n+^{208}Pb from -20 MeV to +165 MeV was done by Johnson, Horen and Mahaux [Joh 87] making full use of the DR to constrain the values of the OP parameters. Johnson *et al.* in another study [Joh 89] utilized the DR in the extrapolation of the dispersive optical model to the resonance region for neutrons on ^{86}Kr. Another application of the DR came in the study of Satchler [Sat 87], where he showed that the DR is applicable to the study of the effective interaction for nuclear nonelastic scattering. Furthermore, the DR was applied in the analysis of the inelastic scattering of 5-11 MeV neutrons with the excitation of the 3$^-$ state in ^{208}Pb in the work of Cheema and Finlay [Che 88]. Further support for the usefulness of the DR is provided by the analysis of analyzing powers of n+^{40}Ca from 9.9 MeV to 16.9 MeV by Tornow and Delaroche [Del 88]. They improved the quality of fit by applying the DR in their analysis in place of the previously needed inclusion of an absorptive spin-orbit term. The same authors utilized the DR approach to investigate the Coulomb correction term of the p-nucleus scattering at energies below 40 MeV [Tor 88]. They showed that DR provides a natural explanation for the observation of a surface contribution to ΔV_C at incident energies in the range they investigated.

The present study extends the range of the application of the DR to study the light nuclei (i.e., for A < 40). Further, this work intended to study the usefulness of the DOM approach for deformed nuclei.

5.3 Formulation of the dispersive optical model (DOM)

In the standard OMP analysis, the OM has been formulated in terms of the incident neutron energy E. In other words, the zero of the energy scale corresponds to the neutron separation energy for the compound nucleus. In the DOM analysis, it is more useful to introduce a different energy, the *Fermi energy* E_F. This choice is made because the mean field is continuous in energy with no special behavior at the neutron separation energy. In fact, Wang and Rapaport have shown in an empirical study of the influence of the symmetry potential on various nuclei, that a more consistent symmetry potential is obtained if the energy is measured relative to E_F [Wan 86]. Therefore, a shifted energy variable is introduced for formulating the DOM.

$$\mathcal{E} = E - E_F \tag{5-2}$$

Then the Mean field of Eq. 5-1 can be written as

$$\mathcal{M}(r;\mathcal{E}) = \mathcal{V}(r;\mathcal{E}) + i\mathcal{W}(r;\mathcal{E}) \tag{5-3}$$

where again $\mathcal{V}$ and $\mathcal{W}$ are the real and the imaginary parts of the mean field, respectively.

In the DOM the real part of the target nucleus is a sum of two components: the dominant one is the average mean field, known as "Hartree-Fock"; the other component is a dispersive contribution and is considered as a correction to the mean field. The real part is then:

$$\mathcal{V}(r;\mathcal{E}) = \mathcal{V}_{HF}(r;\mathcal{E}) + \Delta\mathcal{V}(r;\mathcal{E}) \tag{5-4}$$

The $\mathcal{V}_{HF}$ is the "local equivalent" to the Hartree-Fock potential and the $\Delta\mathcal{V}$ is the dispersive contribution. It is given by:

$$\Delta\mathcal{V}(r;\mathcal{E}) = \frac{P}{\pi}\int_{-\infty}^{\infty} \frac{\mathcal{W}(r;\mathcal{E}')}{\mathcal{E}'-\mathcal{E}}\, d\mathcal{E}' \tag{5-5}$$

where P indicates the principal value.

The imaginary term $\mathcal{W}(r;\mathcal{E})$ consists of two components; the volume absorption $\mathcal{W}_V$ and the surface absorption $\mathcal{W}_S$. Hence, the dispersive term has two contributions: a *dispersive volume* contribution $\Delta\mathcal{V}_V$ and a *dispersive surface* contribution $\Delta\mathcal{V}_S$.

Therefore, the real part of the mean field is then the sum of three terms as:

$$\mathcal{V}(r;\mathcal{E}) = \mathcal{V}_{HF}(r;\mathcal{E}) + \Delta\mathcal{V}_V(r;\mathcal{E}) + \Delta\mathcal{V}_S(r;\mathcal{E}) \tag{5-6}$$

In the original treatment of the nuclear potential, the Hartree-Fock nuclear potential was non-local and independent of energy $\mathcal{V}_{HF}(r; r')$. The non-locality here refers to the idea that the potential at any point depends not just on that point in space but on the wave function in surrounding space. A non-local potential is not easy to characterize. It is therefore convenient to replace it by a "local equivalent" $\mathcal{V}_{HF}(r;\mathcal{E})$, but this procedure requires an energy dependence in the potential [Mah 85]. This local potential is equivalent to the non-local one in the sense that they yield the same scattering phase shifts and single-particle energies.

The energy dependence of the Hartree-Fock and dispersive terms differs considerably. The $\mathcal{V}_{HF}(r;\mathcal{E})$ comes as a result of replacing the nonlocal potential with the local equivalent and has smooth energy dependence. In contrast, the $\Delta\mathcal{V}(r;\mathcal{E})$, which comes from the behavior of the imaginary term through the DR, has a strong energy dependence, particularly near $\mathcal{E} = 0$.

In addition to the central component of the NMF, Eq. 5-6 has to be supplemented by a spin-orbit term $\mathcal{V}_{s.o.}(r;E)$. This term arises from the two-body spin-orbit coupling of the nucleon-nucleon interaction. It is a surface-peaked potential and can be complex.

5.4 Parametrization of the terms of the mean field

In order to apply the DR, some assumptions need to be made. First, the $\mathcal{W}(r;\mathcal{E})$ is assumed to be symmetric with respect to the Fermi energy:

$$\mathcal{W}(r;\mathcal{E}) = \mathcal{W}(r;-\mathcal{E}). \tag{5-7}$$

As a consequence, the dispersive contributions are skew symmetric with respect to E_F, i.e. to $\mathcal{E} = 0$. Thus, at the Fermi energy (where $\mathcal{W}(r;0) = 0$) the real mean field becomes identical to the Hartree-Fock contribution as in Eq. 5-4. Therefore, the Hartree-Fock contribution can be interpreted as the mean field obtained when the scattering process leaves the target in its ground state (i.e., no nucleon-nucleon collisions and only the elastic process

is involved). The parametrization of the Hartree-Fock component is assumed to have the Fermi-form factor usually called Woods-Saxon form:

$$\mathcal{V}_{HF}(r;\mathcal{E}) = V_{HF}(\mathcal{E})\, f(r, R_{HF}, a_{HF}) \tag{5-8}$$

where $f(r,R_i,a_i) = \left[1+\exp\left\{\frac{r-R_i}{a_i}\right\}\right]^{-1}$,

$R_i = r_i\ A^{1/3}$ is the nuclear radius, and a_i is an adjustable parameter called the diffuseness. The radius and diffuseness R and a are referred to as the geometrical parameters.

In practice one can assume that the parameters r_{HF} and a_{HF} are independent of energy and the Hartree-Fock depth is an exponential function of energy [Joh 87, Joh 88]:

$$V_{HF}(\mathcal{E}) = V_{HF}(0) \cdot \exp\left\{\frac{-\alpha_{HF}}{V_{HF}(0)}\,\mathcal{E}\right\}. \tag{5-9}$$

Here $V_{HF}(0)$ is the Hartree-Fock potential depth at the Fermi energy and α_{HF} can be considered as the slope of the Hartree-Fock potential depth at very low energy (if V_{HF} is approximated to be linear in this energy range). [We found it was not necessary to force the parametrization in Eq. 5-9 to be linear for energies below E_F, as it had been done in some analyses [Tor 90] and [Wei 92]. Therefore, we used exponential parametrization throughout the energy range for the two nuclei (i.e., below and above the Fermi energy).]

The absorption or imaginary term of the mean field is represented as the sum of volume and surface contributions:

$$\mathcal{W}(r;\mathcal{E}) = \mathcal{W}_V(r;\mathcal{E}) + \mathcal{W}_S(r;\mathcal{E}). \tag{5-10}$$

It is common to assume that the volume-absorption component has the same radial shape as the Hartree-Fock field, i.e. the Woods-Saxon form. The surface-absorption component is proportional to the radial derivative of the Woods-Saxon form

$$\mathcal{W}_V(r;\mathcal{E}) = W_V(\mathcal{E})\, f(r, R_V, a_V) \tag{5-11}$$

$$\mathcal{W}_S(r;\mathcal{E}) = -4\, a_S W_S(\mathcal{E})\, \frac{d}{dr} f(r, R_S, a_S) \tag{5-12}$$

where $W_V(\mathcal{E})$ and $W_S(\mathcal{E})$ are the strengths of the volume and surface absorptions, respectively. The functions $W_V(\mathcal{E})$ and $W_S(\mathcal{E})$ and their derivatives are required to be continuous in order to apply the DR. The

following forms have been used in some of the works of Mahaux and others (see Sect.. 5.4):

$$W_V(r;\mathcal{E}) = \frac{A_V \cdot (\mathcal{E})^n}{(\mathcal{E})^n + (B_V)^n} \tag{5-13}$$

$$W_S(r;\mathcal{E}) = \frac{A_S \cdot (\mathcal{E})^m}{(\mathcal{E})^m + (B_S)^m} \exp(-C_S\,\mathcal{E}). \tag{5-14}$$

Here n and m are powers derived from nuclear matter theory [Bro 81] and [Jeu 83] and commonly are assigned the values 2, 4, or 6. The A_V and B_V are volume-absorption constants and A_S, B_S and C_S are surface-absorption constants. These free parameters are determined by the best fit to the scattering data.

Recently Mahaux and Sartor [Mah 91] made a modification to the effective range of $W_V(\mathcal{E})$ and $W_S(\mathcal{E})$. This modification suggests a need for improvement to the above functional forms of Eq. 5-13 and 5-14 which assume that the only zero-value of $W_V(\mathcal{E})$ and $W_S(\mathcal{E})$ is at the Fermi energy $E=E_F$. We recall from the discussion of the bound states of Sect. 4.1 that the first single-particle state lies a few MeV above E_F, and that the first single-hole state lies a few MeV below E_F. In the energy region between E_F and the first particle state no interaction can take place. Similarly, no interaction can take place in the energy region between the Fermi energy and the first hole state. Therefore, in the vicinity of the region between the first hole and the first particle states, the $W_V(\mathcal{E})$ and $W_S(\mathcal{E})$ should be zero. Mahaux and Sartor forced $W_V(\mathcal{E})$ and $W_S(\mathcal{E})$ to be zero, but over an even larger range. They preferred to choose the average energy $\bar{E}_p$ of the particle states to define such a region. This $\bar{E}_p$ is given by the sum of the energies of all available particle states divided by their number N as:

$$\bar{E}_p = \frac{1}{N}\sum_{i=0}^{N} E_i\ . \tag{5-15}$$

The particle-averaged energy introduces a change in the reference point of $W_V(\mathcal{E})$ and $W_S(\mathcal{E})$. The new functional form for the volume absorption W_V becomes:

$$W_V\left(E-\bar{E}_p\right)=\begin{cases}\dfrac{A_V\left(E-\bar{E}_p\right)^n}{\left(E-\bar{E}_p\right)^n+\left(B_V\right)^n}, & \text{for} \quad \bar{E}_p < E \\ 0, & \text{for} \quad E_F < E < \bar{E}\end{cases} \tag{5-16}$$

and similarly for the surface absorption W_S:

$$W_S\left(E-\bar{E}_p\right)=\begin{cases}\dfrac{A_S\left(E-\bar{E}_p\right)^m}{\left(E-\bar{E}_p\right)^m+\left(B_S\right)^m}\exp\left\{-C_S\left(E-E_p\right)\right\}, & \text{for } \bar{E}_P < E \\ 0, & \text{for } E_F < E < \bar{E}_P\end{cases} \tag{5-17}$$

In our formulation of the DOM in the search routine GENOA, the average energy $\bar{E}_p$ was determined by introducing an energy offset which adds to the E_F as:

$$\bar{E}_p = E_{offset} + E_F \tag{5-18}$$

In the negative energy range ($E<E_F$), W_V and W_S are determined from the symmetry condition Eq. 5-7.

Still another modification to the functional forms of the absorptive strengths was made by Mahaux and Sartor. This modification focuses on the energy range of the symmetry assumption of W around E_F. In Eq. 5-7, the symmetry assumption neglects the nonlocality effects of W which is much smaller than that of the Hartree-Fock component discussed earlier. These nonlocal effects change the behavior of the absorption components, especially the volume absorption. At large positive energies, nonlocal effects increase the W_V while it approaches zero at large negative energies. For E close to E_F, there is almost no effect due to the nonlocality of W. However, at large $|E|$, this effect is expected to be sizable [Mah 86C, Mah 91]. From nuclear matter studies, Mahaux and Sartor used the following

parametrization for the volume absorption at large negative energies {for $E<(E_F-60)$} to reflect the nonlocal effects:

$$\mathcal{W}_V(E) = W_v(E) - W_v(E_F - 60)\frac{(E-E_F+60)^2}{(E-E_F+60)^2+(60)^2} \tag{5-19}$$

where $\mathcal{W}_V(E)$ is the nonlocal volume absorption and $W_V(E)$ is the symmetric volume absorption.

On the other side of the energy domain (i.e., large positive energies), the absorptive potential is dominated by the strong repulsive nucleon-nucleon (N-N) interaction. In this region the short range N-N interaction can be characterized as a dilute Fermi gas of interacting hard spheres, with a high-energy behavior of:

$$\mathcal{W}(E) \sim \alpha E^{1/2} \tag{5-20}$$

where $\alpha = 1.65$, is a proportionality constant determined by quantities characterizing the Fermi gas [Mah 91]. The following parametrization is used to reflect the nonlocal effects of the volume absorption at large positive energies {for $E>(E_F+60)$}:

$$\mathcal{W}_V(E) = W_v(E) + \alpha\left[E^{1/2} + \frac{(E_F+60)^{3/2}}{2E} - \frac{3}{2}(E_F+60)^{1/2}\right] \tag{5-21}$$

For large $|E|$, the surface-peaked component of the absorption $W_S(E)$ can be neglected since it is due mainly to the surface excitation of the nuclear core. The functional form of the surface absorption, Eq. 5-16, approaches zero at large energies and adequately accounts for nonlocal effects of the surface absorption.

The spin-orbit term is represented by the traditional form

$$\boldsymbol{V}_{so}(r,E) = \left[\frac{\hbar}{m_\pi c}\right]^2 V_{so}(E)\frac{1}{r}\frac{d}{dr}f(r, R_{so}, a_{so})\,\sigma \bullet \ell \ . \tag{5-22}$$

The spin-orbit strength $V_{so}(E)$ takes on the standard linear energy dependence:

$$V_{so}(E) = A_{so} + \alpha_{so} E\,, \tag{5-23}$$

where A_{so} and α_{so} are model parameters determined from the fit to the experimental data.

5.5 DOM search method

The goal of the DOM analysis is to produce a set of parameters that fits the differential cross section, the analyzing power and the total cross section in a wide energy range (for this study up to +80 MeV) and, secondly, that allows the DOM to be extended to the negative energy region in a way that the available bound-state information is reasonably predicted.

In the present analysis, the dispersive optical model was developed through three steps:

i) The optical-model code GENOA was used to obtain optimum values for the DOM parameters to fit all the scattering data.

ii) These optimum values for the DOM parameters were adjusted in order to give an improved prediction to the known bound-state binding energies using the code BOUNDSTATE.

iii) An optimal compromise between the values of the parameters from these two steps was obtained by successive iteration with GENOA and BOUNDSTATE. The process was ended when we obtained a reasonable fit to the scattering data as well as to the binding energies of the bound states.

The search on the global parameters was carried out using a modified version of the code GENOA, which was originally obtained from F. Perey of Oak Ridge National Laboratory. In the modified version, the dispersion relation (DR) formalism and relativistic corrections are included [Wei 92]. Furthermore, the recent suggestion of Mahaux (discussed in Sect. 5.5) to introduce an offset energy in the parametrization of the absorption potentials was included in the presently used search code GENOA. The code calculates the dispersive contributions ΔV_V and ΔV_S by performing the integration of the DR formula Eq. 5-5. These dispersive contributions are added to the real potential prior to calculating the differential cross section, the analyzing power and the total cross section. The code GENOA can perform searches on a single parameter or multiple parameters simultaneously as well as on a series of energies. For each energy and with each choice of parameters, the code makes a given number of iterations to minimize the "chi-squared" (χ^2). This χ^2 is a quantitative measure of the

agreement between the calculation of the DOM and the experimental values. The code optimizes the total χ^2 where $\chi^2 = \sum_{j=1}^{N} \chi^2(E_j)$. At each energy ($E_j$) one obtains a $\chi^2(E_j)$:

$$\chi^2(E_j) = \sum_{i=1}^{N_\sigma}\left[\frac{\sigma^{exp}(\theta_i)-\sigma^{cal}(\theta_i)}{\Delta\sigma^{exp}(\theta_i)/F_\sigma}\right]^2 + \sum_{i=1}^{N_A}\left[\frac{A_y{}^{exp}(\theta_i)-A_y{}^{cal}(\theta_i)}{\Delta A_y{}^{exp}(\theta_i)/F_A}\right]^2 + \left[\frac{\sigma_T{}^{exp}-\sigma_T{}^{cal}}{\Delta\sigma_T^{exp}}\right]^2 \quad (5\text{-}24)$$

Here, $\sigma^{exp}(\theta_i)$ and $\Delta\sigma^{exp}(\theta_i)$ are the value and the uncertainty of the experimental differential cross sections measured at θ_i, respectively. The $\sigma^{cal}(\theta_i)$ is the DOM calculation for the differential cross sections. Likewise, the $A_y^{exp}(\theta_i)$ and $\Delta A_y^{exp}(\theta_i)$ are the value and the uncertainty of the experimental analyzing power and $A_y^{cal}(\theta_i)$ is the DOM calculation. The N_σ and N_A are the number of data points for differential cross section and analyzing power, respectively. The F_σ and F_A are the weights for each $\sigma(\theta)$ and $A_y(\theta)$ distribution. The uncertainty $\Delta\sigma_T{}^{exp}$ is adjusted to furnish a "proper" weight for the $\sigma_T{}^{exp}$.

In addition, the assumption of the symmetry of W_V about the Fermi energy was questioned by Mahaux and Sartor [Mah 91]. A sensitivity study was performed to look into this matter as discussed below in Sect. 5.6.1.

In the DOM used to describe the data, an offset of 3 MeV from the Fermi energy was used in the absorptive terms $W_V(\mathcal{E})$ and $W_S(\mathcal{E})$. That is, the absorption is not allowed to turn on in the 6-MeV region:

$$[(E_F - 3\ MeV) < E < (E_F + 3\ MeV)]$$

surrounding the Fermi energy. This follows the philosophy introduced by Mahaux and Sartor [Mah 91] that there should be no absorption between (approximately) the last hole- and first particle-states. We relaxed this offset condition in examinations to be discussed in the paragraphs on "sensitivities to parameter variations" near the end of Sect. 5.6.1.

As a preliminary step towards developing the model, we started with potentials and parameters from previous analyses. The most closely related optical-model analysis for the two nuclei under investigation in this work is that of Howell [How 84]. Although the parameters in his work were

derived from a conventional spherical optical-model (i.e., non-dispersive OM) analysis applicable only to the 8-40 MeV region (40% of the energy range of this study), the OM was considered to be a reasonable starting point.

In the first step of the analysis, *single-energy* searches were done at each energy for data sets between 2-40 MeV to obtain a reasonable set of starting parameters to eventually fit the entire set of scattering data. The energy dependence of the real potential during these single-energy searches was fixed close to that of Howell. This first step was expected to lead to obtain reasonable starting parameters for the functional form of the volume and surface absorption W_V and W_S. The code GENOA was first set to search upon the potential strengths: $V_{HF}(0)$, $W_V(\mathcal{E})$ and $W_S(\mathcal{E})$, then upon the geometries, and finally upon both simultaneously (avoiding the known ambiguities).

After obtaining the best values of $W_V(\mathcal{E})$ and $W_S(\mathcal{E})$ for all energies, a least-square routine (utilizing the functional forms of Eqs. 5-13 and 5-14) was used to obtain the optimum values for the constants (A_V, B_V, n and A_S, B_S, C_S, m) of the two functions. From this initial search-test, the absorption strengths were found to favor the values 4 and 6 for the powers n and m, respectively. The values of these seven constants were used as starting parameters in the following global-energy search.

The next step was to search simultaneously for optimum values over the entire energy range. A data set that is *global* in energy was constructed for this step. It contained all the $\sigma(\theta)$, $A_Y(\theta)$ and σ_T from the energy range 1 - 80 MeV. In this search, a broad parameter search was conducted where many combinations of parameters were searched simultaneously. The potential strengths $V_{HF}(0)$, $W_V(\mathcal{E})$, $W_S(\mathcal{E})$ and V_{SO} were first searched keeping all geometries fixed. These new optimized strengths were then used to initiate a second search on the geometrical parameters. A third search was conducted on the exponential constant α_{HF} of the HF potential and the absorption strengths $W_V(\mathcal{E})$ and $W_S(\mathcal{E})$.

As mentioned before, the search method was based on the minimization of the χ^2. But sometimes the χ^2 reaches a local minimum in the multi-parameter chi-squared space that gives a poor fit to the data,

while there is a deeper minimum elsewhere with another set of parameters (i.e., parameters that give a better fit). To ensure that the search method would search for the optimum values of a given parameter over a wide range (and not miss the optimum set of parameters), sensitivity studies were carried out in a restricted-parameter search on one or two parameters. Two of the parameters which were examined are the powers n and m of the absorption strengths. Different combination of values were tested by stepping the values from 1 to 8 in an integer step. In addition, we conducted free searches on only the powers and the corresponding constants (i.e., n with A_V, B_V, and m with A_S, B_S, C_S). As a result of all these searches, the values 4 and 6 became the clear choice due to the good quality of the fit they provide to the scattering data.

Another parameter that was studied closely is the exponential constant α_{HF} of the HF potential. A search on α_{HF} showed that there is a relatively wide range of values that can fit the scattering data. This led us to step the values of α_{HF} in increments of 0.05 between 0.20 and 0.65 and repeat the previous broad searches on the strengths and geometries. The result of this test revealed that there are three different regions of values for α_{HF} that gave good fits. These are 0.28-0.30, 0.42-0.44 and 0.48-0.55.

A third parameter, C_S of $W_S(\mathcal{E})$, was also investigated. During the free search upon this parameter, it was noticed that the data favor small values of C_S. A small value keeps the absorption strength relatively constant beyond a certain energy, thereby giving a large surface absorption at high energies (E > 50 MeV). A large surface absorption above 50 MeV is inconsistent with older global conventional optical models and with theoretical microscopic OM calculations. For this reason, we carefully studied this parameter. The C_S was changed in steps of 0.002 between 0.010 and 0.025 while performing the broad searches on the strengths and geometries. In all the above searches, both the χ^2 and the quality of fit to the scattering observables were examined carefully to determine the optimum values.

The next step in the parameter search was performed in the negative energy region, i.e., a "search" on the bound-state energies for the neutron single-particle and single-hole states. As mentioned in Sect. 4.1, the two

nuclei Si and S are deformed and this leads to a fragmentation of their single-particle states. This fragmentation causes the spectroscopic factors of these states to be less than one. Because of the fragmentation, our emphasis in this stage of the study was on the qualitative features of the DOM prediction of the binding energies (B.E.) and not on full quantitative agreement with all the experimental binding energies. In particular, we were interested in observing the ability of the model to predict the experimental Fermi energy and the deepest hole state which is believed to be less fragmented. The deepest hole states in ^{28}Si and ^{32}S are around -56.6 and -78.6 MeV respectively.

The code BOUNDSTATE, which was provided by Johnson of ORNL [Joh 90], was automated [Wei 92] and used to predict the binding energies. A sensitivity study for the prediction of the single-particle B.E. to changes in the DOM parameters was conducted in order to investigate systematic trends in the B.E. calculation. The binding energies of the particle and the hole states are directly related to the strength and the geometry of the HF potential. A decrease in the slope of the HF potential tends to shift both the particle and the hole states closer to the Fermi energy. The size of this shift is proportional to the distance of the particle or the hole state from the Fermi energy. The binding of particle and hole states is also dependent on the strength (A_V and A_S) of the absorptions. An increase in A_V results in an increase of the B.E. of the particle states and a decrease of the B.E. of the deep hole states. On the other hand, an increase of A_S increases the B.E. of the particle states without affecting the hole states appreciably.

It should be noted that the addition of the dispersive contribution $\Delta V(r;\mathcal{E})$ to the HF component $V_{HF}(r;\mathcal{E})$ makes the full potential more attractive than the HF component alone. Addition of this term increases the B.E. of the particle states ($E > E_F$). On the other hand, adding in the $\Delta V(r;\mathcal{E})$ decreases the B.E. of the hole states ($E < E_F$) because it makes the full potential less attractive than the HF component alone.

The most important parameter in predicting the B.E. of the states near the Fermi energy was the depth of the real potential at the Fermi energy, that is, $V_{HF}(0)$. One of the requirements of the dispersive approach is that the DOM potential should yield a symmetric prediction around E_F

for the first particle state and the last hole state, i.e., the least bound hole state. In order to determine $V_{HF}(0)$, a version of the code BOUNDSTATE was used to predict the value of the HF potential which is required to produce the exact experimental B.E for a specific particle or hole state. Based on that version of the code, the $V_{HF}(0)$ and the slope α_{HF} were adjusted (from the optimum search values reached in the first step) to locate the B.E. for the first particle and the last hole state symmetric with respect to the Fermi energy. For the two nuclei studied in this work, the required adjustment of the optimum parameters was about 5% of their value. This determination of the HF potential helps in the judgment of the best choice of the different regions of the slope for V_{HF} found in step *i)* of the search.

Another point to mention in the prediction of the hole states is the type of energy dependence of the HF potential for energies below E_F. In addition to the original exponential form Eq. 5-9, a linear function with the same slope at $E = E_F$ was also tested for $E < E_F$:

$$V_{HF}(\mathcal{E}) = V_{HF}(0) - \{\frac{\alpha_{HF}}{V_{HF}(0)}\mathcal{E}\}, \qquad (5\text{-}25)$$

where $V_{HF}(0)$ and α_{HF} have the same values as in the exponential form of Eq. 5-9. The two functional forms have different predictions for the B.E. of the hole states, affecting the deepest hole state the most. This test was suggested by the early work of [Joh 87] who preferred the linear function over the exponential function in their ^{208}Pb(n, n) study.

In the final steps, we returned to GENOA and performed searches on the positive-energy side to accomplish two things: First, to adjust the choice of the DOM parameters toward values which are desirable, as determined in the above sensitivity studies with BOUNDSTATE; Second, to initiate new searches starting with the optimum values found in the BOUNDSTATE studies in order to examine how much they must be readjusted to fit the scattering data. Eventually, a combination of these two processes of searching with the code GENOA and periodically checking the B.E. predictions with the code BOUNDSTATE was conducted until we determine a good set of parameters, that is, one that gives a good fit to the scattering data and also a reasonable prediction of the B.E. for most of the bound states.

5.6 The *n*-^{28}*Si* mean field analysis

In this section the results of the DOM analysis to derive the neutron mean field of ^{28}Si at the positive and the negative energy regions are discussed. In the $E > 0$ region, the experimental total and differential cross sections along with the analyzing power are compared with those calculated from our DOM analysis. In the $E < 0$ region, the experimental binding energies of the single-particle and -hole states are compared with the prediction of the same DOM extended to negative energies.

5.6.1 The *n*-^{28}*Si* mean field at positive energies

The database used in developing the DOM for neutrons scattered from ^{28}Si was given in Sect. 4.1. After subtracting the compound nucleus contribution from the experimental values for neutron energies below 14 MeV, a global-energy database was created for the energy range 0.3-80 MeV. In this global data set, there are 25 single-energy data sets consisting of 25 σ_T values, 16 $\sigma(\theta)$ distributions and 4 $A_y(\theta)$ distributions. At the beginning of the GENOA search, the σ_T were assigned an artificial uncertainty of ± 0.2% at all energies in order to give this observable adequate weight in the search. After several global DOM searches, we found that the model produced a large χ^2 in the low-energy ($E < 8$ MeV) total cross sections. Therefore, the artificial uncertainty was increased to ± 0.7% for the low-energy σ_T. In addition, the $\Delta\sigma_T$ was decreased to ± 0.1% at high-energies ($E > 40$ MeV) where only σ_T data were available; this was necessary in order to force the proper shape for the calculation of $\sigma_T(E)$ in this region. The previously described search method and the periodic prediction of the B.E. were carried out until the parameters converged to the values listed in Table 5-1. These values are considered by us to be optimum under various search compromises and constraints. The absorption potential strengths W_V and W_S and the corresponding dispersive contributions ΔV_V and ΔV_S are represented by the solid and the dashed curves in Figs. 5.1 and 5.2, respectively.

The calculations of the total cross sections from these parameters are compared with the averaged experimental total cross sections (see references in Sect. 4.1) in Fig. 5.3a for energies up to 80 MeV. The DOM

calculations (solid curve) give very good agreement with the experimental values over the broad energy range 8-80 MeV. However, in the low energy range 1-8 MeV the model overestimates the total cross section by about 13%. Recall that below 12 MeV there is much resonance structure in $\sigma_T(E)$ (see Fig. 5.3b). The dots shown as data in Fig. 5.3a represent an average of the σ_T data obtained from references in Table 4.1. The intervals taken for averaging were 50 keV for E<6 MeV, 200 keV for E>6 MeV and 2 MeV for E>30 MeV.

The DOM overestimation of the total cross section at low energies has been seen before in DOM analyses on ^{40}Ca [Joh 88] and ^{27}Al [Nag 92]. (In the previous conventional phenomenological approach (SOM) by Howell [How 84], the overestimation of the low-energy cross sections was even more severe than in the DOM calculations shown in Fig. 5.3a.) One cause of this difficulty might be based on the fact that the total cross section at low energies is dominated by very few partial waves (mainly *s* and *p* waves), and the absorption might be *l*-dependent (see [Joh 87]); in our DOM approach it is assumed that the absorption of the mean field is independent of the orbital angular momentum. Another possibility of the overestimation is that the true physics requires a model with energy-dependent geometries at low energies. A test was made to investigate the sensitivity to parameter variations in this region; we found that the total cross sections could be fit very well with lower values for the surface absorption geometry (r_S =1.043 fm and a_S =0.34 fm), but these values destroy the good fits at high energies. Our code for calculating the dispersive corrections does not allow us to have an E-dependent r_S, so it was not possible to insert such a modification in the DOM. As mentioned above, Nagadi [Nag 92] also had difficulties in describing σ_T data at low energy in his DOM and a coupled-channels (CC) study of the nearby nucleus ^{27}Al. He showed that by reducing the radius parameter r_V (for the real potential) in the CC model to about 1.07 fm for 1 < E < 10 MeV, he could greatly improved the agreement to σ_T. Because the radius parameter for V_{HF} and W_V are constrained to be equal in our (and Nagadi's) DOM, it would be necessary to carry out the dispersive integrals with an energy dependent radius r_V.

Table 5.1 DOM parameters for n-^{28}Si

The Real Term

V_{HF} (MeV)	α_{HF}	r_V (fm)	a_V (fm)
59.42	0.50	1.165	0.70

The Imaginary Term

A_V (MeV)	B_V (MeV)	power n	r_{WS} (fm)	a_{WS} (fm)	A_S (MeV)	B_S (MeV)	C_S	power m	E-offset (MeV)
11.56	89.76	4	1.315	0.52	10.65	7.50	0.010	6	3.00

The Spin-orbit Term

V_{SO} (MeV)	α_{SO} (MeV)$^{-1}$	r_{SO} (fm)	a_{SO} (fm)
5.31	-0.015	1.09	0.45

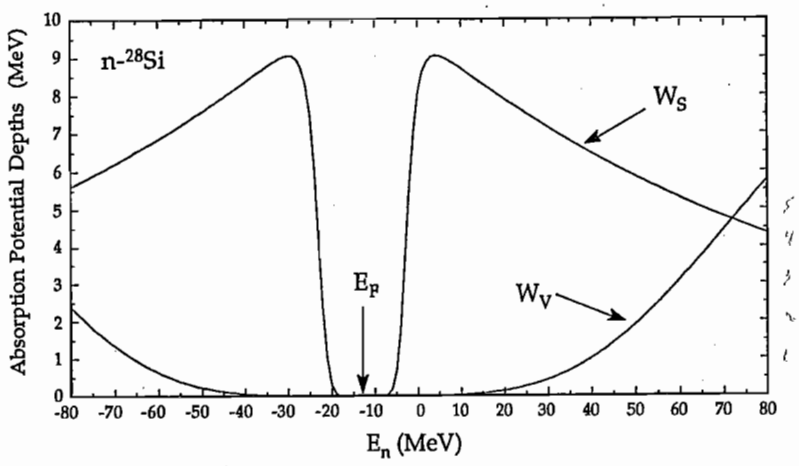

Figure 5.1. The energy dependencies of the absorptive surface potential (W_S) and the absorptive volume potential (W_V) for *n-28Si*. The Fermi energy E_F is indicated.

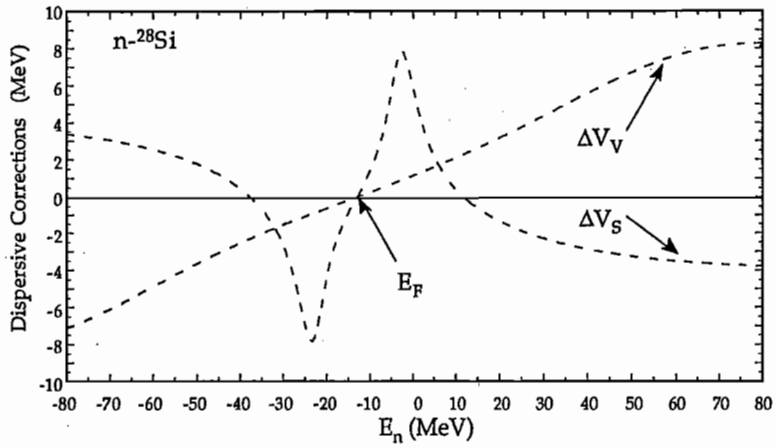

Figure 5.2. The energy dependencies of the dispersive corrections of the absorptive surface potential (ΔV_S) and the absorptive volume potential (ΔV_V) for *n-28Si*.

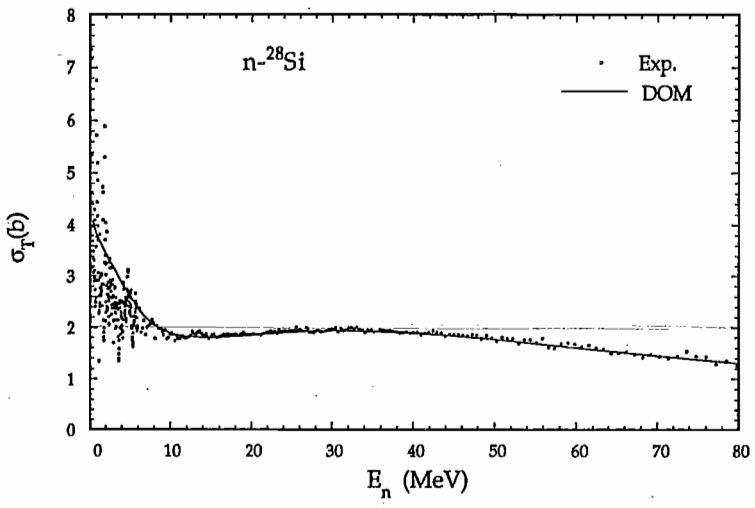

Figure 5.3a. Total *n-^{28}Si.* cross section in the energy range between 0 and 80 MeV. The dots are experimental values (see text) and the solid curve is the DOM prediction.

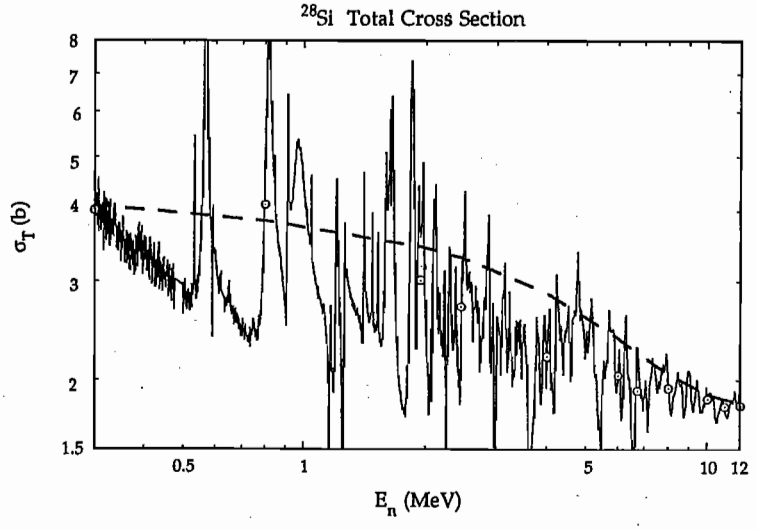

Figure 5.3b. The resonance structure in the total cross section of *n-^{28}Si.* in the energy range between 0 and 12 MeV. The open circles are the values of the total cross section at the energies used in DOM calculations. The dashed curve is the DOM prediction.

Again, this is not possible with our formulation. Therefore, we could not asses the effect of an E-dependent r_V.

The DOM fits to the differential cross section are shown in Figs. 5.4, 5.5 and 5.6. The points are the experimental values as reported in the literature, and the solid curves are DOM calculations added to the compound nucleus contributions for E ≤ 14 MeV. (The compound nucleus contributions for E ≤ 14 MeV were subtracted from the measured values of σ(θ) to obtaine the shape-elastic values which were used in the search procedure.) In the search for optimum parameters, the inclusion of the differential cross section at 40 MeV was very important for constraining the behavior of the absorptive potential at higher energies. In general, the agreement between the DOM calculations and the data is quite good for E > 11 MeV, although there are some discrepancies at the backward angles in the energy region 17 < E < 21 MeV. The fit in that region can be improved by merely decreasing the surface absorption strength by about 10%. This is shown by the dashed line in Fig. 5.6. This improvement implies that the exponential form of the E-dependence for the surface term may not be adequate. In general, the quality of the DOM fits is quite similar to that of the SOM in [How 84], even in the 17-21 MeV region. Since the DOM model is constrained to fit bound state B.E. and σ(θ) data below 10 MeV (neither of which were studied in the SOM of [How 84], we are pleased with the overall quality of agreement.

In Fig. 5.7 it is shown that the DOM calculations give a good description of the analyzing power at forward and backward angles. However, the DOM predictions lie above the data in the 60° - 95° region. The quality of the fits obtained with the DOM is similar to that of the SOM prediction [How84], except at 14 MeV where the DOM prediction is slightly better.

The influence of the choice of spin-orbit radius r_{so} was examined by merely decreasing its optimum value by about 5% and then 10%. The largest effect of the decrease in r_{so} was noticed in the forward spikes of the $A_y(\theta)$ distributions, particularly at E = 14 MeV. The decrease in r_{so} enhances the first positive spike in the analyzing power at E=10 MeV and the first negative spike at E=15.5 and 17 MeV, leaving the rest of the distributions almost unchanged.

Furthermore, we found that merely adding an imaginary term to the spin-orbit potential did not improve the overall agreement with the analyzing power data. We tested this by adding the small absorption spin-orbit term

proposed in the Walter and Guss global SOM model [Wal 86] with a geometry similar to the surface-absorption geometry (r_{so}=1.31 fm and a_{so}=0.52 fm). The inclusion of this term lowers the analyzing power beyond 50° as shown in the dashed curve of Fig. 5.8.

To test the sensitivity of the data to the removal of the energy offset, we searched with GENOA with the offset equal to zero. In general, the σ(θ) and $A_y(\theta)$ agreement was not affected. A decrease in the σ_T curve of Fig. 5.3a for E < 8 MeV gives about 4% improvement in the DOM calculation.

Another version of GENOA was used to test the symmetry condition for the W_V of Eq. 5-7. In this version W_V is replaced with the Mahaux and Sartor [Mah 91] modification of Eq. 5-16. Here W_V is replaced by a function that decreases to zero strength as E drops to about -200 MeV and, in addition, a function that adds more absorption than our original DOM formulation for $W_V(E)$ for E > 60 MeV. (See [Mah 91] for details.) In our version of GENOA one has the choice of turning on the effect only at negative energies or turning on the effects at both negative and positive energies. Because the W_V in our model is optimized at high energies by fitting high-accuracy σ_T data, we question the need to add the extra absorption above 60 MeV. Furthermore, the larger absorption seems to be inconsistent with high-energy conventional SOM's. Therefore, we place more belief in a model that only turns off the absorption at E ≈ -200 MeV. Nevertheless, we tested the ability of the DOM for n - ^{28}Si to incorporate both modifications to $W_V(E)$. Starting with the parameter values in table 5.1 we used GENOA to optimize the DOM parameters. For the case where we drop W_V to zero at 200 MeV, we did not observe any significant change in the calculations; similar fits were obtained to those of the symmetry case. However, in the "full asymmetry" DOM, the calculations overpredict the σ_T for E> 55 MeV; the source of this discrepancy seems to be traceable to too much absorption.

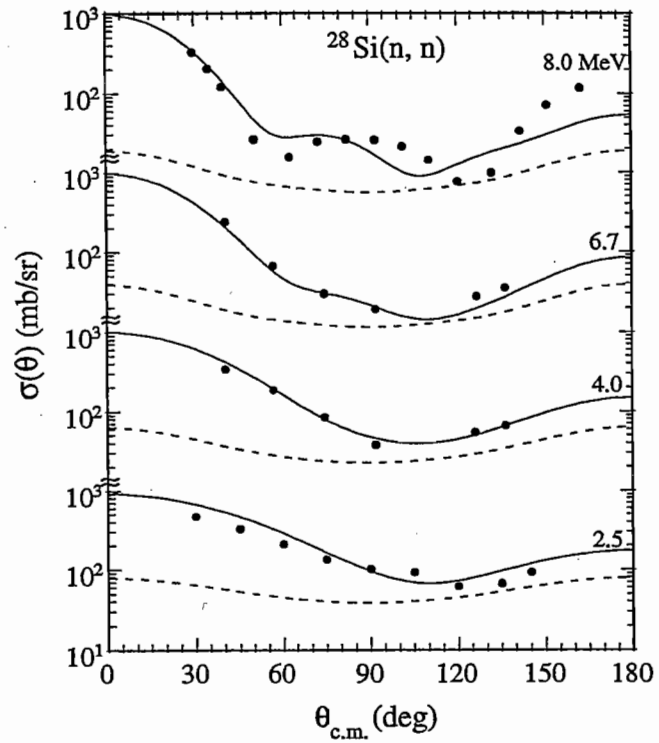

Figure 5.4. DOM calculations compared to the differential cross sections of neutron scattering from ^{28}Si at incident energies between 2.5 and 8 MeV. The dots are the experimental values, the solid curves are the DOM calculations added to the compound nucleus contributions and the dashed curves are the compound nucleus contributions.

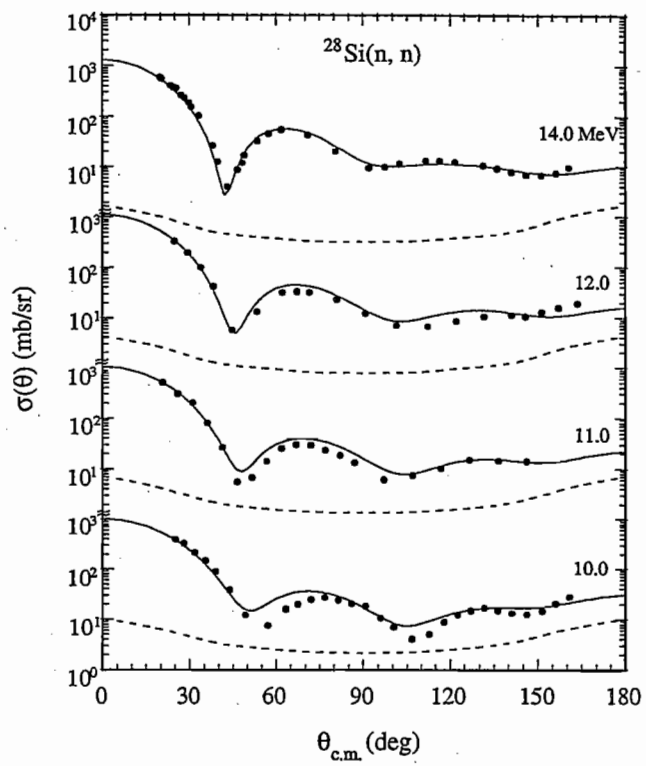

Figure 5.5. DOM calculations compared to the differential cross sections of neutron scattering from ^{28}Si at incident energies between 10 and 14 MeV. The dots are the experimental values, the solid curves are the DOM calculations added to the compound nucleus contributions and the and the dashed curves are the compound nucleus contributions.

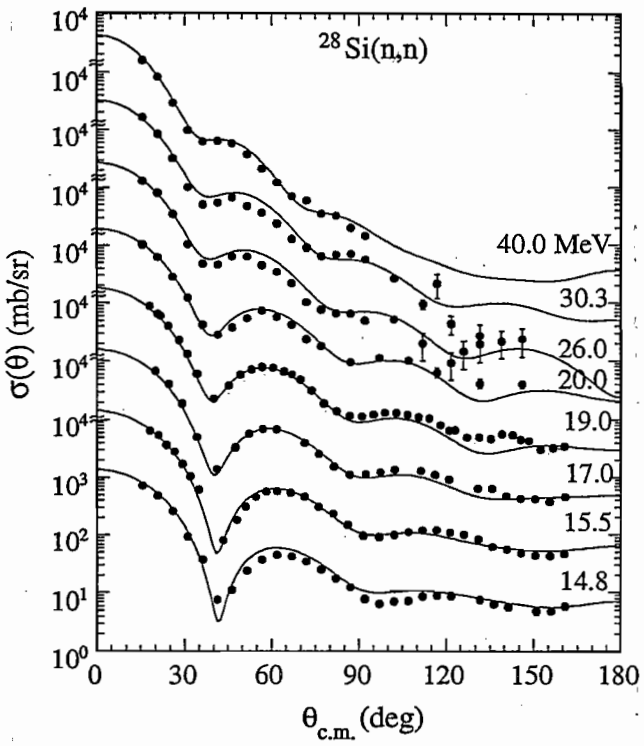

Figure 5.6. DOM calculations compared to the differential cross sections of neutron scattering from ^{28}Si at incident energies between 14.8 and 40 MeV. The solid curves are the DOM calculations and the dots are the experimental values.

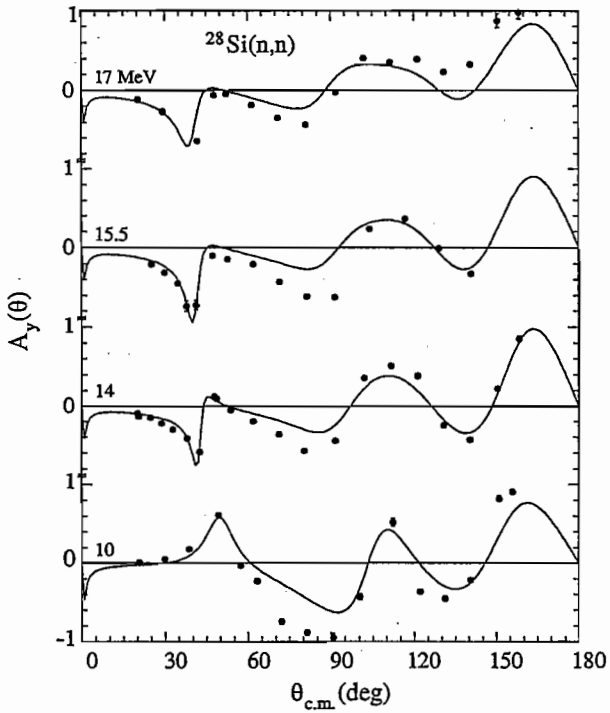

Figure 5.7. DOM calculations compared to the analyzing powers for neutron scattering from ^{28}Si at incident energies 10, 14 15.5 and 17 MeV. The solid curves are the DOM calculations and the dots are the analyzing power data.

One of the main features of the DOM approach is its capability to link the two energy regions by the extension of the real part of the mean field into the negative energy region, i.e., into the region of the bound states (located on both sides of the Fermi energy). In Fig. 5.9, the smooth-energy dependence of the depth of the HF potential for n-^{28}Si is shown as it cross from positive to negative energies.

Using BOUNDSTATE we determined a value for the HF potential depth at the energy E=E_F=-12.83 MeV by requiring that the calculated binding energies of the first particle state ($2s_{1/2}$) and the last hole state ($1d_{5/2}$) are centered around E_F. Using the geometry for our optimum potential (r_v = 1.165 fm and a_v = 0.70 fm), this requirement or constraint gives the following value for the depth of the HF potential: $V_{HF}(E_F)$ = -59.42 MeV.

With this constraint of the HF potential as one which we continually checked as we developed our DOM, the model is capable of fitting the scattering data at E > 0 and when extended to E < 0, it predicts nearly symmetric binding energies about the Fermi energy for the last hole state and the first particle state. In fact, the E_F is predicted by our model to be -12.85 MeV, which is in very good agreement with the value of -12.83 MeV, determined from separation energies. (see Sect. 4.1.). The deepest hole state ($1s_{1/2}$) has a B.E.=-56.6 MeV; the exponential form of the HF potential (as in Eq. 5-9) using our DOM parameters predicts -62.4 MeV. That is, our DOM gives a little overbinding (≈ +6 MeV) but this amount is within the estimated uncertainty of 5 to 10 MeV assigned to this level. When the linear energy-dependence (as in Eq. 5-25) is used, the prediction for this level is 54.5 MeV, only 2MeV from the experimental value. All the other hole states differ by less than 3% from the ones calculated with the exponential energy dependence. Although the linear energy-dependence prediction comes closer to the experimental $1s_{1/2}$ value, we will not consider it further because of two considerations. First, it is simply more convenient to have the same energy dependence for the entire energy range of the mean field of the two systems under study. Second, due to the more deeply bound $1s_{1/2}$ state for ^{32}S (discussed in Sect. 5.7.2), it was necessary to use the exponential form to come close to this deepest hole state.

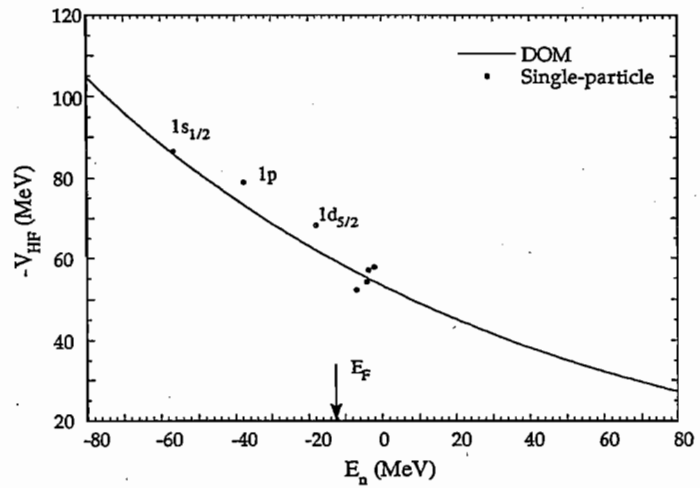

Figure 5.8. The smooth-energy dependence of the depth of the Hartree-Fock potential V_{HF}. The dots are the required V_{HF}-depths to predict the exact binding energies of n-^{28}Si.

On the right-hand side of Fig. 5.10 the predicted binding energies for the single-particle and -hole states (using the exponential form) are shown along with the experimental values. The deepest hole state shown in the figure between parenthesis ($1s_{1/2}$) indicate the predicted binding energy using the linear form. The effect of relaxing the $W_V(E)$ symmetry condition on the prediction of the binding energies was to spread the predictions farther from the E_F; i.e., it worsened the agreement with the experimental values. For the hole states it increased the B.E. by 0.1% at the last hole ($1d_{5/2}$) to 8% at the deepest hole ($1s_{1/2}$). For the particle states the B.E. decreased by 0.2% at the first particle ($2s_{1/2}$) to 15% at the last particle ($2p_{1/2}$). For the case of the "full asymmetry," the B.E. of both states decreased giving worse prediction than those for the "E < E_F asymmetry" case.

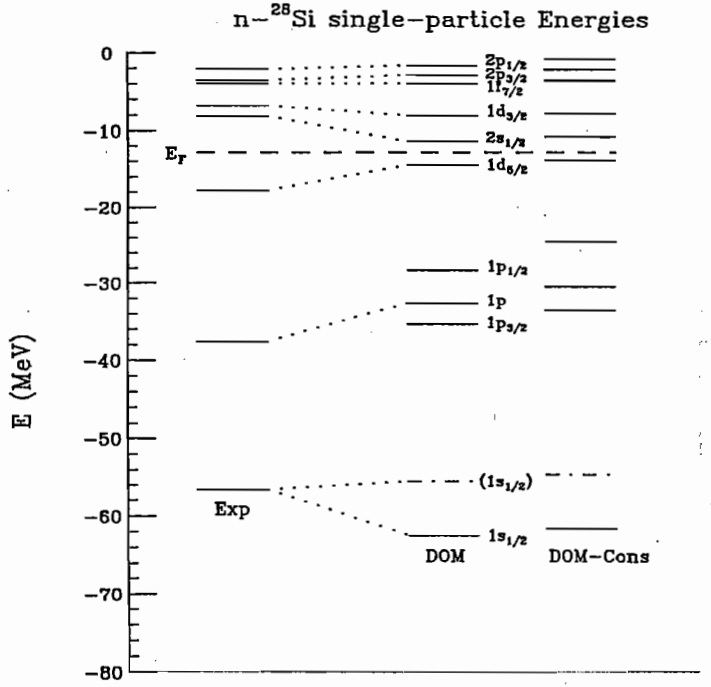

Figure 5.9. Neutron single-particle energies in n-^{28}Si. The column labeled EXP represents the experimental values. The column labeled DOM gives the predicted energies from a dispersive optical model for ^{28}Si. The column labeled DOM-Cons gives the predicted energies from a dispersive optical model for nuclei in the mass number between 27 < A < 32 discussed in Chap. 6.

In Fig. 5.10, the calculated binding energies for the first particle state ($2s_{1/2}$) and the last hole state ($1d_{5/2}$) show an overbinding for $2s_{1/2}$ while a less binding for $1d_{52}$ compared to experiment. We note that the difference between the separation energy $(E_F)^-$ =-17.177 MeV of ^{28}Si and $(E_F)^+$ =-8.474 MeV of ^{29}Si is very wide. Johnson and Mahaux [Joh 88] in their n-^{40}Ca analysis point out that when the $(E_F)^+$–$(E_F)^-$ gap is large, as in our case, the definition used here for (E_F) =1/2{ $(E_F)^-$ + $(E_F)^+$} is probably not adequate for describing both the particle and hole states near the Fermi energy region. The reason for that is the strong dependence of the real radius on energy in the vicinity of E_F, which causes the DOM model to predict large values for $(E_F)^+$ and small values for $(E_F)^-$. This weakness, of the averaging of the Fermi energy, might account for the difference in the B.E. between the DOM calculations and the experimental values.

5.7 The n-^{32}S mean field analysis

In the present section, a discussion similar to that given in Sect. 5.6 for n-^{28}Si is presented for the system n-^{32}S. Since the approach in this DOM analysis was very similar to that for ^{28}Si, fewer details will be reported. In addition, some comparisons with the SOM of [How 84] are also discussed.

5.7.1 The n-^{32}S mean field at positive energies

A database was created for ^{32}S in the energy range between 0.3 and 80 MeV. In this global data set the only available total cross section data are for neutron energies below 32 MeV (see Sect. 4.1). Since we require a wide energy domain to derive the nuclear mean field for ^{32}S, we estimated the total cross section for energies between 32 and 80 MeV. This was done using two models. One is an estimate using the parameters of the ^{28}Si DOM model where the A = 28 is replaced by A=32 and the proper E_F is used. The other is to extend Howell SOM model for ^{32}S [How 84]. The estimates from the ^{28}Si DOM model gave values that are about 10% higher than the ^{28}Si total cross sections. The SOM prediction for ^{32}S was only 4% lower than the DOM estimate. The average 7% was taken as our best estimate for predicting the ^{32}S total cross sections in the energy range of 32-80 MeV. Therefore, the experimental σ_T values for ^{28}Si between 32-80 MeV plus 7% was taken as ^{32}S "data".

In addition, there are 16 measurements for $\sigma(\theta)$ and 4 measurements for $A_y(\theta)$. The weighting assignments to the data are similar to those in the ^{28}Si global database except that the σ_T at E>32 MeV were given a factor of four reduced weighting in the χ^2 search (i.e., $\Delta\sigma_T = \pm 0.2\%$ instead of $\pm 0.1\%$ as in ^{28}Si). The optimum DOM parameters obtained in a search method similar to that discussed in Sect. 5.6 are listed in Table 5.2. These parameters were obtained using an energy offset of 3.0 MeV in the absorption potential parametrization forms. The absorption potential strengths W_V and W_S (and the corresponding dispersive contributions ΔV_V and ΔV_S for the n-^{32}S mean field) are represented by the solid and the dashed curves in Figs. 5.11 and 5.12, respectively.

Table 5.2 DOM parameters for n-^{32}S

The Real Term

V_{HF} (MeV)	α_{HF}	r_V (fm)	a_V (fm)
57.71	0.54	1.18	0.69

The Imaginary Term

A_V (MeV)	B_V (MeV)	power n	r_{WS} (fm)	a_{WS} (fm)	A_S (MeV)	B_S (MeV)	C_S	power m	E-offset (MeV)
12.8	74.7	4	1.265	0.52	12.0	12.5	0.0125	6	3.00

The Spin-orbit Term

V_{SO} (MeV)	α_{SO} (MeV)$^{-1}$	r_{SO} (fm)	a_{SO} (fm)
5.5	-0.015	1.05	0.48

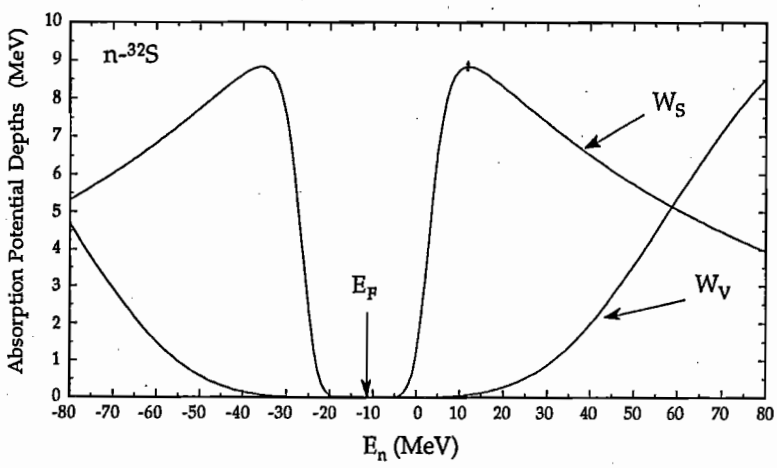

Figure 5.10. The energy dependencies of the absorptive surface potential (W_S) and the absorptive volume potential (W_V) for n-^{32}S. The Fermi energy E_F is indicated.

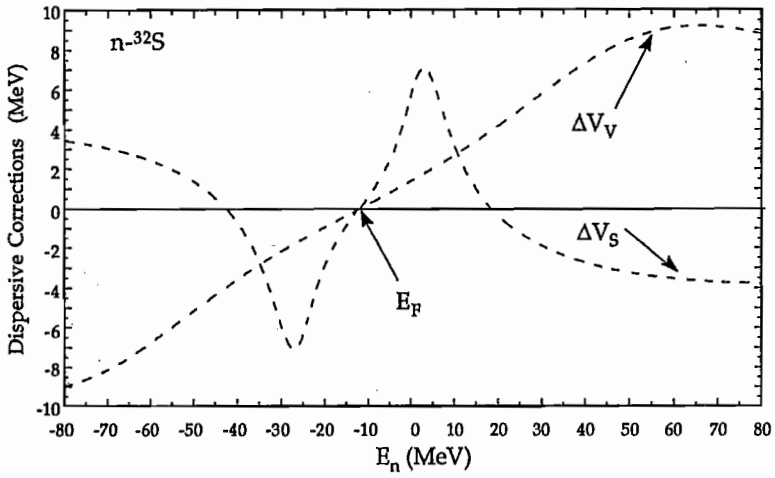

Figure 5.11. The energy dependencies of the dispersive corrections of the absorptive surface potential (ΔV_S) and the absorptive volume potential (ΔV_V) for n-^{32}S.

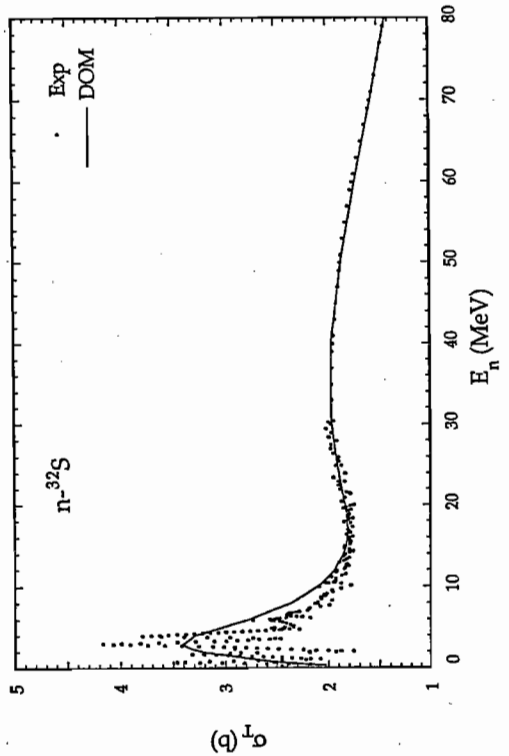

Figure 5.12. Total n-^{32}S cross section in the energy range between 0 and 80 MeV. The dots are experimental values and the solid curve is the DOM prediction.

The prediction (solid curve) of the present DOM for the total cross section in the energy range 0 to 80 MeV is shown in Fig. 5.12, where the points are the averaged experimental data. For E > 8 MeV, the model gives a good description for the total cross section, while it overestimates σ_T below E < 8 MeV. This problem has been seen in Sect. 5.6 in the case of Si, and the discussion there is applicable here as well.

In Figs. 5.13, 5.14 and 5.15 the DOM fitting to the experimental differential cross-section data is shown. The points are the experimental values as reported in the literature, and the solid curves are DOM calculations added to the compound nucleus contributions for E ≤ 12 MeV. (The compound nucleus contributions for E ≤ 12 MeV were subtracted from the measured values of $\sigma(\theta)$ to obtaine the shape-elastic values which were used in the search procedure.) The agreement is exceptionally good in most regions. Notice the excellent prediction of the model to our measurement at 15.5 and 19.0 MeV. However, the calculations are too high at the forward angles for the low energies; this translates to an overestimation of the total cross section in that energy region.

The DOM model calculation of the analyzing power is compared to the measured values in Fig. 5.16. The points at 10 MeV represent the experimental shape-elastic $A_y(\theta)$. As in the case of ^{28}Si, the calculations reproduce the shape of the $A_y(\theta)$ data quite well at most angles except in the 95°-130° region where the calculations are lower than the measured values. The present work contributes the additional analyzing power distribution at 15.5 MeV, which was particularly significant in the determination of the DOM parameters. The significance of this data set comes from the positive spike suggested by the measured values around 42°. A series of sensitivity tests were carried out to predict the correct shape of this spike. The sign of the spike was found to be sensitive to the slope of the real potential and to the spin-orbit geometry, especially the diffuseness. The mere inclusion of an absorption term of the size of [Wal 86] into the spin-orbit potential neither improved nor spoiled the quality of the fit.

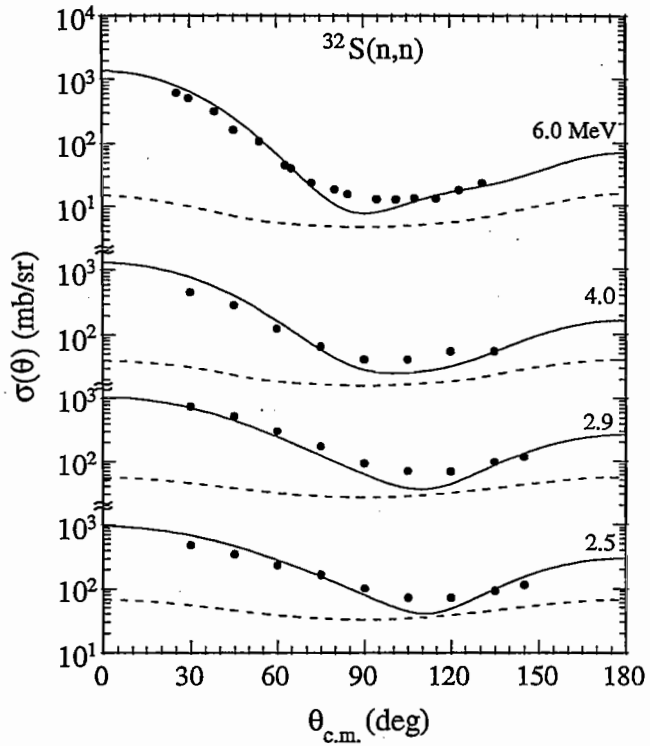

Figure 5.13. DOM calculations compared to the differential cross sections of neutron scattering from ^{32}S at incident energies between 2.5 and 6 MeV. The dots are the experimental values, the solid curves are the DOM calculations added to the compound nucleus contributions and the and the dashed curves are the compound nucleus contributions.

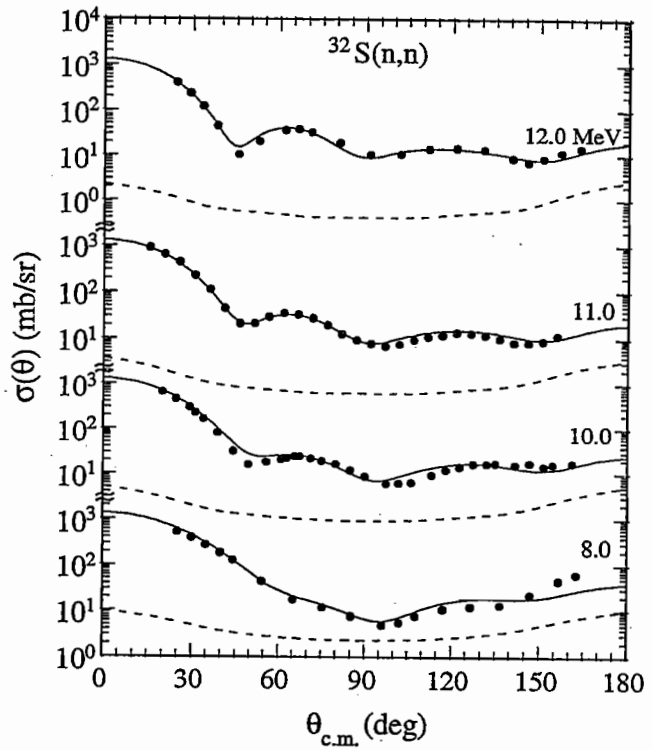

Figure 5.14. DOM calculations compared to the differential cross sections of neutron scattering from ^{32}S at incident energies between 8 and 12 MeV. The dots are the experimental values, the solid curves are the DOM calculations added to the compound nucleus contributions and the and the dashed curves are the compound nucleus contributions.

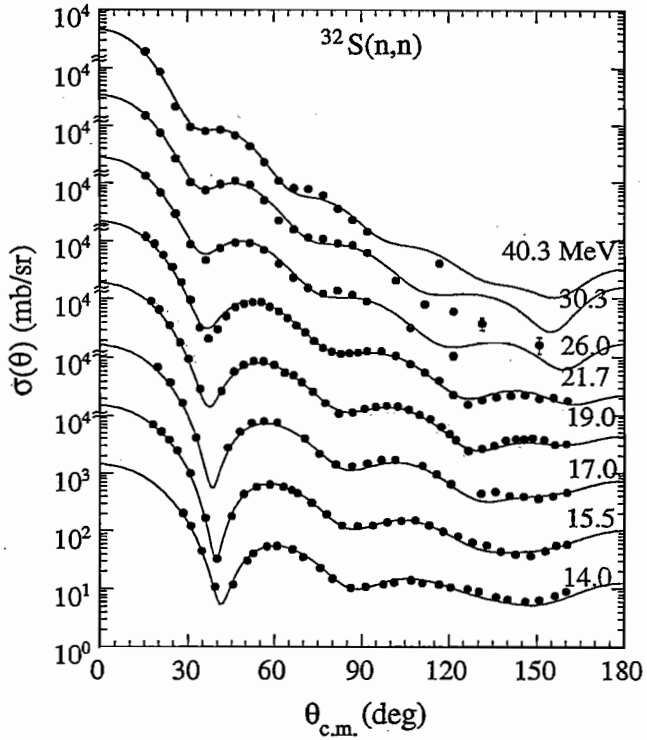

Figure 5.15. DOM calculations compared to the differential cross sections of neutron scattering from ^{32}S at incident energies between 14 and 40 MeV. The solid curves are the DOM calculations and the dots are the experimental values.

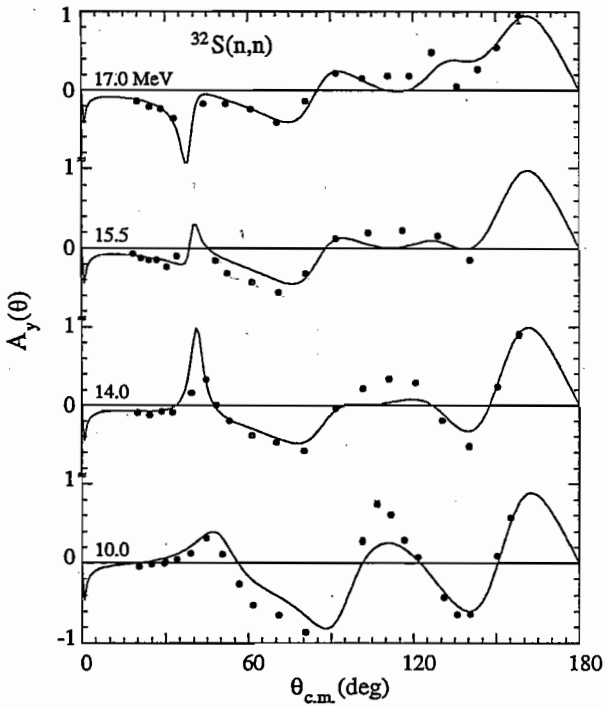

Figure 5.16. DOM calculations compared to the analyzing powers for neutron scattering from ^{32}S at incident energies 10, 14 15.5 and 17 MeV. The solid curves are the DOM calculations and the dots are the analyzing power data.

In comparison to the SOM analysis [How 84], the DOM calculation for the total cross section is superior in almost the entire energy range of [How 84], i.e. 8 - 40 MeV. Compared to the SOM of [How 84], this DOM study provides additional information on the total cross section at $E_n < 8$ MeV and $E_n > 50$ MeV, and the differential cross section at $2 < E_n < 8$ MeV. The DOM predictions for the differential cross section for neutron energies of 8 and 10 MeV represent the data better than the SOM; the two models give similar quality of fits for the rest of the distributions, i.e., for E > 10 MeV. The DOM and SOM give almost identical fits to the analyzing power.

5.7.2 The *n*-^{32}S mean field at negative energies

In this section we discuss the results of the extension of the real part of the mean field into the negative energy region in order to predict the bound states of the n-^{32}S system. The energy dependence of the HF potential is shown in Fig. 5.17 for the energy range between -80 and 80 MeV. The depth of the HF potential at the Fermi energy of ^{32}S ($E = E_F = -11.87$ MeV) was determined by the requirement that the calculated binding energies of the first particle state ($1d_{3/2}$) and the last hole state ($2s_{1/2}$) is symmetric around E_F. When using the optimum real potential geometry ($r_v = 1.18$ fm and $a_v = 0.68$ fm), the constraint gives the following value for the depth of the HF potential: $V_{HF}(E_F) = -57.71$ MeV.

In Fig. 5.18 the calculated binding energies for the single-particle states are shown with the experimental values. The E_F was predicted by our model to be centered between the last hole and the first particle states and it has the value -11.78 MeV, less than a 1% difference from the value of -11.87 MeV determined from neutron separation energies. The conventional phenomenological optical model SOM (which was adjusted to fit the scattering cross sections only) predicts -10.47 MeV for E_F, giving about 12% difference from the experimental value. From the physical point of view, this reflects the meaningfulness of extracting the real potential from the dispersive approach rather than from the conventional phenomenological approach. The binding energy of the deepest hole state is -78.1 MeV; it was necessary to use the exponential form Eq. 5-9 to predict such a deep state. The model prediction for this very deep state was in very good agreement with the measured value (see Fig. 5.18).

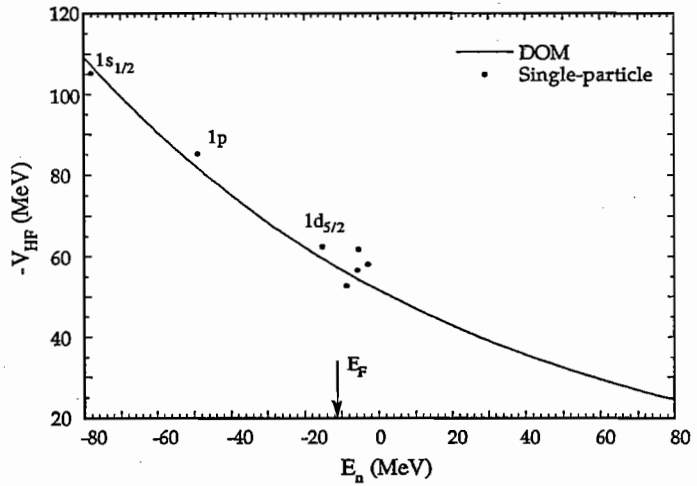

Figure 5.17. The smooth-energy dependence of the depth of the Hartree-Fock potential V_{HF}. The dots are the required V_{HF}-depths to predict the exact binding energies of the n-^{32}S.

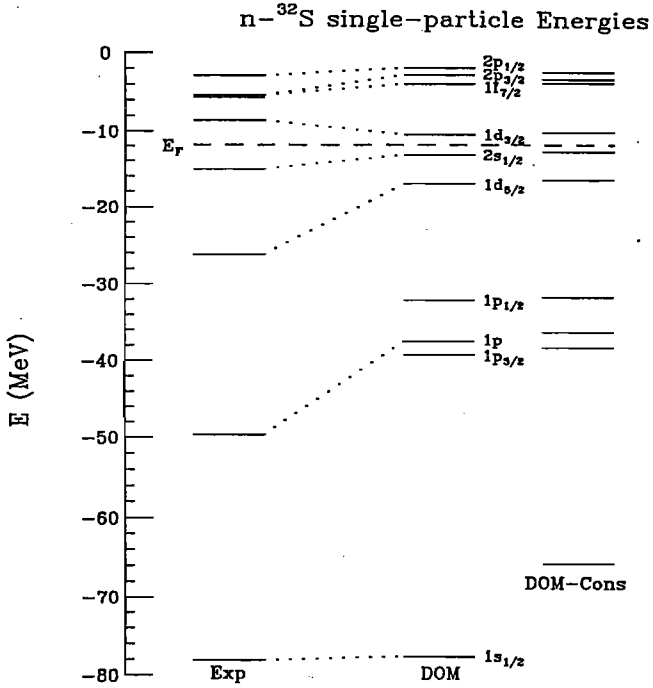

Figure 5.18. Neutron single-particle energies in n-^{32}S. The column labeled EXP represents the experimental values. The column labeled DOM gives the predicted energies from a dispersive optical model for ^{32}S. The column labeled DOM-Cons gives the predicted energies from a dispersive optical model for nuclei in the mass number between 27 < A < 32 discussed in Chap. 6.

5.8 Comparison between NMF

Different nuclear mean fields (NMF) for neutron, derived through DOM analyses, have been developed in 40 < A < 208 as mentioned in Sect. 5.4. Since the NMF of ^{28}Si and ^{32}S represent the lightest nuclei where "full application" of the DR was applied, it is of great interest to compare the results achieved from these two nuclei with the previous reported analyses. The NMF from ^{40}Ca, ^{90}Zr, ^{208}Pb are reported in [Joh 88], [Del 89], [Mah 91A], respectively. The comparison will focus on the main parameters of the NMF, namely: the HF potential depth at the Fermi energy $V_{HF}(E=E_F)$, the energy-dependence of the HF potential (α_{HF}), and the HF real radius r_{HF}. In Table 5.3, the values of these parameters compared to those obtained in the present work. In addition, we listed the Fermi energy E_F and asymmetry parameter η=(N-Z)/A, where A is the mass number.

Table 5.3: Comparison of the parameters of the NMF for different nuclei

Nucleus	^{208}Pb	^{90}Zr	^{40}Ca	^{32}S	^{28}Si
A	208	90	40	32	28
η	0.212	0.111	0	0	0
E_F	-6	-9.6	-12	-11.87	-12.83
$-V_{HF}(E=E_F)$	46.4	52.45	58.8	57.7	59.42
$-\alpha_{HF}$	0.31	0.33	0.55	0.54	0.50
r_{HF}	1.23	1.21	1.18	1.18	1.165

The radius decreases as the mass number A decreases. The dependence of r_{HF} on the mass number is represented in Fig. 5.19. One can parametrize this dependence by the following relation:

$$r_{HF} = 1.295 - 0.385\ A^{-1/3}. \qquad (5\text{-}26)$$

Two conclusions can be made here. First, this parametrization supports the earlier parametrization (r_{HF}=1.298 - 0.405 $A^{-1/3}$) proposed in [Jeu 91] where the study stopped at A = 40. Second, the parametrization of Eq. 5-26 has better accuracy than [Jeu 91] because, in their study, the imaginary part of the MF was not required to vanish in the energy region between $(E_F)^- < E < (E_F)^+$ in the DOM analyses of ^{40}Ca and ^{90}Zr. This agreement gives credence to the

extrapolation of the dispersive-relation approach to the lighter nuclei studied in the present work.

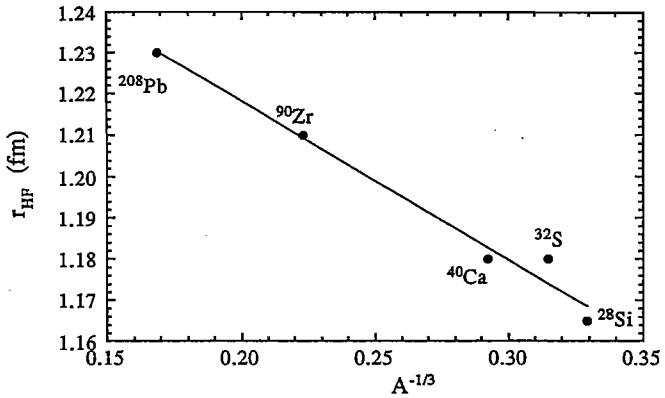

Figure 5.19. The dependence of the HF radius r_{HF} on the mass number A.

The increasing values for the depth of $V_{HF}(E=E_F)$ follow the trend of the depth of the E_F, where it suggests a dependence shown in Fig. 5.20 and represented by the following:

$$-V_{HF}(E=E_F) = 34.26 - 1.983\ E_F \qquad (5\text{-}27)$$

The dependence of the Fermi energy upon the neutron excess η of these nuclei is shown in Fig. 5.21. Although the Fermi energy does not depend only upon η, a rough dependence can be represented as:

$$E_F = -12.31 + 28.60\ \eta \qquad (5\text{-}28)$$

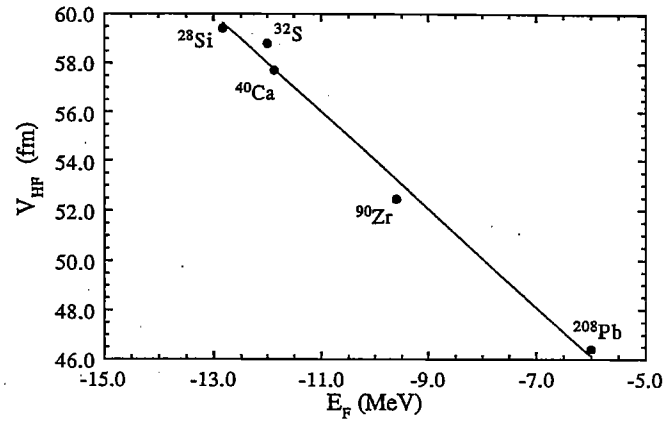

Figure 5.20. The dependece of the HF depth V_{HF} at the E_F on the Fermi energy E_F.

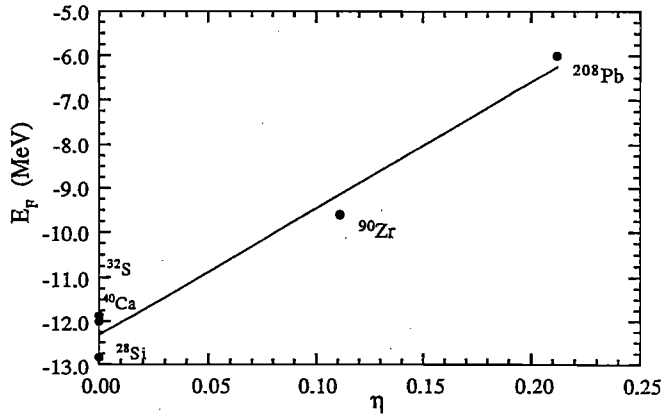

Figure 5.21. The dependence of E_F upon the neutron excess η.

CHAPTER 6

Global Dispersive Optical Model for ^{27}Al, ^{28}Si, and ^{32}S

Global Dispersive Optical Model for ^{27}Al, ^{28}Si, and ^{32}S

6.1 Introduction

The beauty of the phenomenological optical model is that it can produce the average behavior of elastic-scattering observables, i.e., the total, differential and reaction cross sections and the analyzing power, as a function of energy and mass. By its nature, it does not produce the fine resonance features in the cross sections, since these depend on details of the quantum states in the compound nucleus. Many analyses utilizing the optical model were successful in describing the scattering of a particle from an individual nucleus at a certain energy or at different energies (see [Hod 71] for review). Other so-called "global analyses" also studied many nuclei at different energies. Among the earliest and most widely used global phenomenological OMP analyses are those of Becchetti and Greenlees [Bec 69]. The range of the analyses were limited to neutron energies below 30 MeV, and to targets with $A > 40$. In 1982 Rapaport developed a neutron-nucleus optical model for $A > 16$ and $7 \leq E \leq 30$ MeV. However, the global parameters for both of these studies were less successful in describing the scattering data for nuclei of $A < 40$ than for $A > 40$. Therefore, some specific optical model potentials have been developed to improve the description of the scattering data in this low mass region.

The nuclei in the 2s-1d shell are known to have excited states with a highly collective nature. In particular, the nuclei near the center of the shell provide an attractive ground to which many nuclear models are applied. A conventional spherical optical model (SOM) study was done by Martin [Mar 87] for the same nuclei studied in this work, but in a more limited energy range (i.e., between 14 and 40 MeV). With the recent and more theoretically-based approach of the dispersion relation (which was developed in Sect. 5.4), individual nuclear systems have been better

described. In Chap. 5, we applied the DOM approach to neutrons scattered from ^{28}Si and ^{32}S in a wide energy range (-80 to 80 MeV).

The success of our individual DOM analyses for the n-^{28}Si and n-^{32}S systems and the success of Martin [Mar 87] with a global regional SOM led to the idea that it would be possible to obtain a global DOM for the 2s-1d shell nuclei by including the n-^{27}Al system into a database for ^{28}Si and ^{32}S.

As part of the TUNL program to develop dispersion relation analyses for different systems, a recent DOM analysis for neutrons scattered from ^{27}Al in the same energy range as this study (0–80 MeV) was recently completed by Nagadi [Nag 92] and was moderately successful. In the present chapter, a new DOM analysis for neutron scattering from ^{27}Al is developed, one which includes the recent modification suggested by Mahaux and Sartor [Mah 91]. This new dispersive model for n-^{27}Al is compared with the DOM analyses of the n-^{28}Si and n-^{32}S systems. In the final step the three systems are studied in concert to investigate the global nature of neutron scattering from nuclei in the center of the 2s-1d shell.

Our global DOM analysis has a more extensive database and wider energy range than that of [Mar 87]. Since the energy dependence of the real potential arises more naturally in the DOM, it has an advantage over the conventional SOM; it is easier to describe data over the wide energy range 0-80 MeV. The five high quality neutron differential cross sections and three sets of analyzing power data, which six of them measured in the present work at TUNL, are expected to help obtain a better determination of the OMP parameters, especially the spin-orbit parameters.

Therefore, the aim of the present chapter is to provide a constrained set of DOM parameters which will provide a description of the observables for neutrons scattered elastically from nuclei in the mass region $27 \leq \tilde{A} \leq 32$.

6.2 The Global Database

For the n-^{28}Si and n-^{32}S systems the database has been described in Chap. 4.1. For the n-^{27}Al system, the data used in this chapter are the same data as described in [Nag 92]. The total cross sections were obtained from Oak Ridge National Lab for the energies 2.0-80.0 MeV [Lar 81] and for the energies 0.2-49.0 MeV [Per 72]. For the $\sigma(\theta)$, there are 14 angular distributions in the energy range between 2.0 and 25.0 MeV. The data at the energies 2.0, 3.0, 6, 7, and 8 MeV were obtained from [Hol 69]. The data at 7.6 MeV was obtained from [Sch 89], at 9 MeV from [Vel 74], at 11, 14, 17 MeV from [Whi 84], at 15.4 MeV from [Nag 92], at 20, 22, 25 MeV from [Pet 85], and finally at 21.6 MeV from [Ols 87]. There are 3 data sets for the analyzing power: 14 and 17 MeV, which were obtained from [Whi 84], and 15.4 MeV from [Nag 92]. The compound nucleus contributions were subtracted from the differential cross sections for energies less than 11 MeV. The compound nucleus contributions were taken to be the same as those applied in [Nag 92]. The neutron Fermi energy for ^{27}Al is determined from the average of the separation energies in ^{27}Al and ^{28}Al: E_F = -10.4 MeV.

6.3 DOM potential form

In Sect. 5.5, the DOM potential formulation was discussed in detail and similar forms are used here in this chapter. In the formulation of the real and absorption strengths in the model, the reference energy used is the Fermi energy. *The selection of the Fermi energy as the reference energy is one of the advantages of the DOM formulation, especially for global parameter studies.* This favorable feature of the DOM eliminates one of the "structure" problems that enters into developing a global model. These structure differences occur even though the three nuclei lie close together in mass number. Therefore, in a global DOM parameter search, one attempts to obtain identical parameters for the three nuclei, but the forms will give each nucleus its proper strength value for the energy (relative to the Fermi energy). For example, the difference in mass between ^{27}Al and ^{28}Si is only one mass unit, but the difference in their neutron Fermi energy is -2.43 MeV {[^{27}Al – ^{28}Si] = -10.4 – (-)12.83}. To incorporate

the recent suggestion of Mahaux [Mah 91] concerning the constraint of the absorption potential, an energy offset of 3.0 MeV was included in the parametric forms of the volume and surface absorption forms of Eqs. 5.16 and 5.17.

6.4 Improved DOM for n-^{27}Al

In the present section, we discuss a new DOM for n-^{27}Al. The previous ^{27}Al-DOM analysis, developed by Nagadi (we will refer to it as ^{27}Al-Nag), was reasonably successful in describing the scattering data. However, this model overestimates the σ_T for E < 10 MeV. Upon examining the ^{27}Al-Nag parameters and comparing them with the corresponding parameters for the ^{28}Si and ^{32}S models developed in Chap. 5, one notes that the determination of the strength of the HF potential in ^{27}Al-Nag appears to be low {$V_{HF}(E=E_F)$=-51.16 MeV or $V_{HF}(E=0)$= *-48.03 MeV*}. It is about 7 MeV lower than the corresponding HF potentials at E=E_F of our analyses of neutrons scattered from ^{28}Si {$V_{HF}(E=E_F)$=-59.42 MeV} and ^{32}S {$V_{HF}(E=E_F)$=-57.71 MeV}. This low magnitude for the HF strength in ^{27}Al-Nag may be one of the reasons that cause the overestimation of the total and the differential cross sections at E<10 MeV. From our experience in the development of DOM for ^{28}Si and ^{32}S, we learned that an increase in the magnitude of the real potential (either in V_{HF} or in its slope) decreases the calculated value for σ_T.

From the database listed in Sect. 6.2, a global (in energy) data set for ^{27}Al was created; it contains 25 σ_T values, 14 $\sigma(\theta)$ distributions and 3 $A_y(\theta)$ distributions. The same version of the search code GENOA was used to carry out the development of the DOM. The σ_T data were assigned an artificial uncertainty of ± 0.7% for the low-energy (E < 8 MeV) and ± 0.1% for E > 10 MeV to increase the weight in the search.

The search procedure commenced by merely inserting the ^{28}Si-DOM parameters (listed in Table 5.1) in order to examine how well these parameters of the mass-neighbor will work. The prediction of the ^{27}Al scattering data from the ^{28}Si-DOM parameters reproduced the general shape of the experimental data, but the calculations of σ_T and $\sigma(\theta)$ were low in most energy regions. This underestimation of the $\sigma(\theta)$ data indicated that

the strength of the absorption of ^{28}Si-DOM are too high for ^{27}Al, especially at E > 10 MeV. Recognizing this, another search-test was done, but this time the surface absorption was decreased by lowering W_S in the region of the exponential tail (see Fig. 6.2). A value of 0.017 was used for the constant C_S in Eq. 5.17. The results of the test were remarkable. The fit was significantly improved; a factor of almost 2 was gained in the χ^2.

Before we searched on the HF potential two concerns had to be addressed. Since there is no reliable experimental information available on the single-particle states for neutrons and holes in ^{27}Al, the HF potential had to be derived using the isospin dependence of the real central potential between ^{27}Al and ^{28}Si. (The latter is a self-conjugate nucleus, i.e., T=0.) Using the isovector component (V_1 =16.5 MeV) of the Walter-Guss global Model [Wal 86], the isospin difference for the real potential was calculated to be 0.61 MeV {V_1 x (N-Z)/A= 16.5 x 1/27}. The second concern is related to the different Fermi energies. Due to the difference in E_F between ^{28}Si and ^{27}Al (2.43 MeV), a shift was also applied to determine the HF potential at E = E_F for ^{27}Al. Keeping the same V_{HF} slope as for ^{28}Si (0.50), a value of +1.22 MeV (0.50 x 2.43) was also subtracted from the V_{HF} of ^{28}Si to obtain a value for ^{27}Al. The end result of applying these corrections gave $V_{HF}(0)$=-57.59 MeV for ^{27}Al.

Using the above determined parameters for C_S and $V_{HF}(E_F)$, a new search was carried out to optimize the absorption potentials. The powers *n* and *m* of W_V and W_S were kept at 4 and 6, respectively. During this step of the search, it was found that the data favored a smaller value for the surface absorption constant B_S, which indicates a need for a faster rise in the form of W_S (at low energies). Different searches were performed on the strength parameters A_V and A_S alone, and then with B_V, B_S and C_S. The result was a better fit to the data, especially for σ_T (about 25% improvement in χ^2).

Next, the search was focused on optimizing the geometries. The real radius (r_V) was not changed. A search on the real diffuseness (a_V) and the absorption radius (r_S) and diffuseness (a_S) improved the fit, especially in the minimum of the differential cross sections.

The last step in the search was to optimize the spin-orbit potential parameters. The original parameters of the ^{28}Si-DOM give a reasonable fit

to analyzing power data. The search converged to smaller values for the geometry with very slight improvement on the χ^2 for the analyzing power.

Before presenting the final parameters and their fits to the scattering data, we developed another version of the ^{27}Al-DOM, with a very slight change from the previous model. Now, only the isospin-dependence difference is considered. A value of $V_{HF}(0)$=-58.81 MeV {-59.42 + 0.61} was calculated for the HF potential. A similar search upon A_V and A_S was carried out to optimize their values. We will refer to the parameters from this version as ^{27}Al-DOM-1.

The optimum values for the DOM parameters for ^{27}Al-DOM and ^{27}Al-DOM-1 are listed in Table 6.1. In fact, the fits from the two versions of DOM were very similar except for a very small difference (1% or less) in σ_T for E < 6 MeV.

The DOM prediction of the total cross sections for the neutron energies up to 80 MeV is shown by the solid curve in Fig. 6.1. Throughout the whole energy range, the DOM developed in this work gives a better prediction than ^{27}Al-Nag or SOM [Mar 86], especially for E < 8 MeV. In this work, the overestimation of σ_T in ^{27}Al-Nag is reduced from 26% to 8%. (The percentage is an average values of the overestimation for E < 8 MeV).

The prediction of σ_T became even better when the following adjustment was made. In the original ^{28}Si-DOM, a 3.0 MeV energy offset was introduced in the parametric form of W_V and W_S to ensure that there is no absorption in the near vicinity of the Fermi energy. We found that for ^{27}Al, when the energy offset is removed, a 23% gain in total χ^2 is obtained. The main improvement appears in σ_T for E < 6 MeV where the calculation came very close to the data with only 5% overestimation. This is shown in Fig. 6.1 by the dashed curve. The improvement suggests the need for higher surface absorption in that region (faster rise-up). This finding gives another indication for the need to improve the parametrization of the current exponential form of W over all energy regions. In Fig. 6.2 the surface absorption potential with an energy offset of 3.0 MeV is represented by the solid curve and with no energy offset is represented by the dashed curve.

Table 6.1 DOM parameters for n-^{27}Al

Parameter	^{27}Al-DOM-1	^{27}Al-DOM
V_{HF} (MeV)	58.81	57.59
α_{HF}	0.50	=
r_V (fm)	1.17	=
a_V (fm)	0.665	=
r_{WS} (fm)	1.285	=
a_{WS} (fm)	0.55	=
A_V (MeV)	8.60	10.30
B_V (MeV)	79.76	=
Power n	4	=
A_S (MeV)	9.44	9.33
B_S (MeV)	4.7	=
C_S	0.0155	=
Power m	6	=
V_{SO} (MeV)	5.59	=
α_{SO} (MeV)$^{-1}$	-0.015	=
r_{SO} (fm)	1.03	=
a_{SO} (fm)	0.42	=
Energy-offset (MeV)	3.00	=

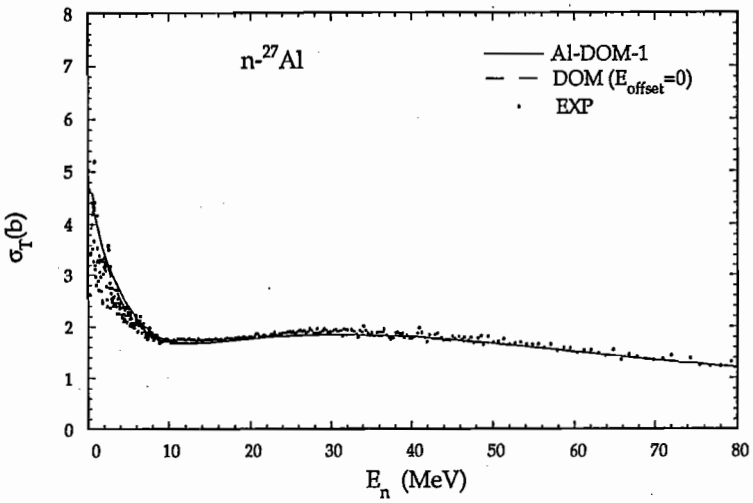

Figure 6.1a. Total n-^{27}Al cross section in the energy range between 0 and 80 MeV. The dots are experimental values and the solid and the dashed curves are the predictions of DOM with and without an energy offset in the absorption potentials (see text).

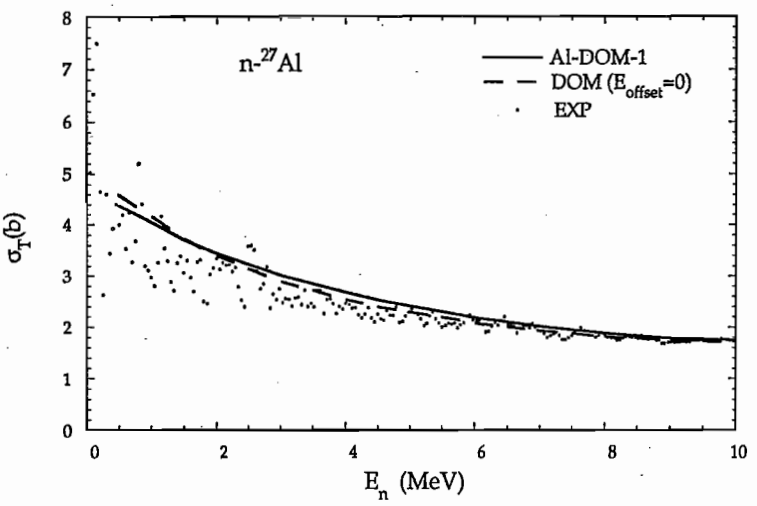

Figure 6.1b. Total n-^{27}Al cross section in the energy range between 0 and 10 MeV. The dots are experimental values and the solid and the dashed curves are the predictions of DOM with and without an energy offset in the absorption potentials (see text).

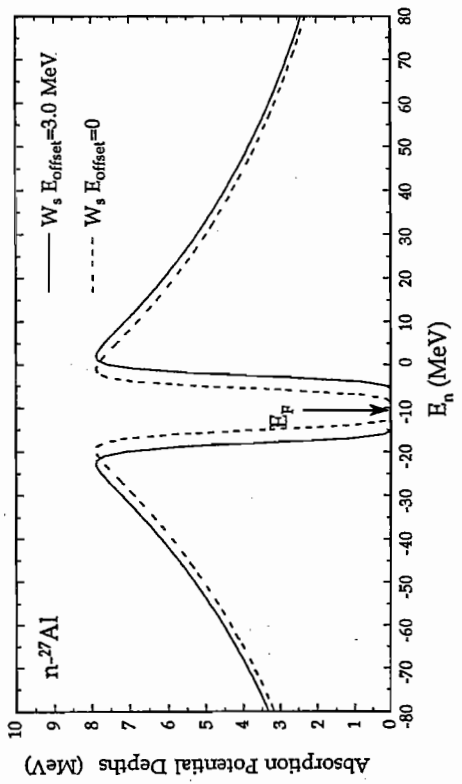

Figure 6.2. The energy dependencies of the absorptive surface potential (W_S) for *n-27Al* with and without energy offset.

The results of the fits to the differential cross-section data obtained with the parameters listed in Table 6.1 are represented by the solid curves in Figs. 6.3 and 6.4. The DOM fit to $\sigma(\theta)$ is very good for E > 8 MeV, except at backward angles for E = 15.5 MeV where the calculation is lower. In this region, the quality of the fit with our model is similar to that of ^{27}Al-Nag or the SOM. (Remember that the SOM energy range of study was only 30% of the energy-range of the present study.) For E < 7 MeV, where the compound nucleus contribution is quite large, our model gives a reasonable fit to $\sigma(\theta)$, considering the resonant behavior of the n-^{27}Al system in this energy range. In comparison with ^{27}Al-Nag, our model is superior for predicting $\sigma(\theta)$ for E < 7 MeV; the 60% overestimation problem of ^{27}Al-Nag is reduced to about 25% in our model. This overestimation is even reduced to about 5–10% when no offset is included in the absorption forms. In the $\sigma(\theta)$ data (Figs. 6.3 and 6.4), the error bars shown in the minimum correspond to an assigned uncertainty on the extracted value for σ^{SE} (= σ^{EXP} - σ^{CN}) of 50%. (Similar large uncertainties were used for the GENOA search to take care of the uncertainty in the CN calculation and to minimize problems caused by resonances in the region from 2 - 8 MeV).

In Fig. 6.5 the calculation of the model is compared to the measured analyzing power. The model reproduces the shape of the data quite well except in the region 60° < θ < 90°, where the calculation is high. We studied the sensitivity of the data to the introduction of an imaginary spin-orbit potential to the model using the W_{so} parameters of the Walter-Guss model [Wal 86], but no real improvement was achieved. The quality of the fit to $A_y(\theta)$ reached in this work is comparable to the fit of ^{27}Al-Nag and the SOM where a smaller geometry (r_{so} =1.00 fm and a_{so} =0.41 fm) was used for the spin-orbit potential.

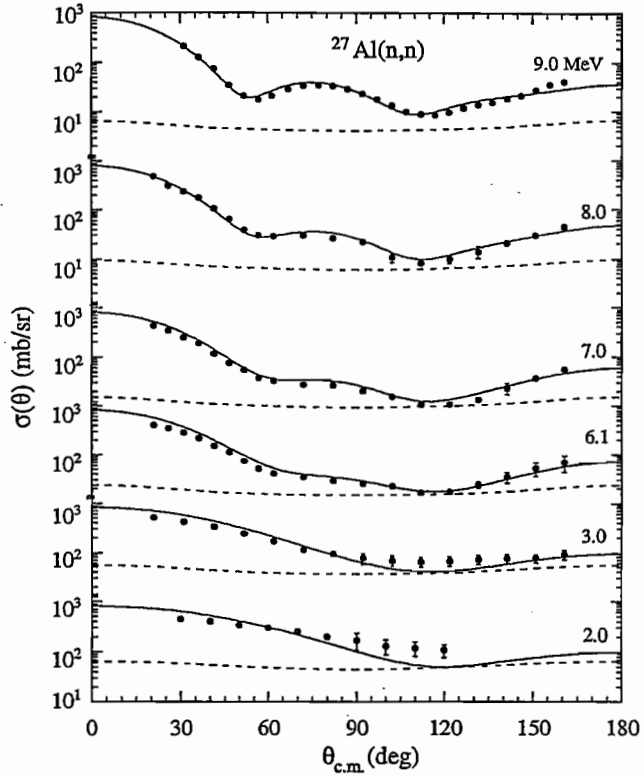

Figure 6.3. DOM calculations compared to the differential cross sections of neutron scattering from ^{27}Al at incident energies between 2 and 9 MeV. The dots are the experimental values, the solid curves are the DOM calculations added to the compound nucleus contributions and the dashed curves are the compound nucleus contributions.

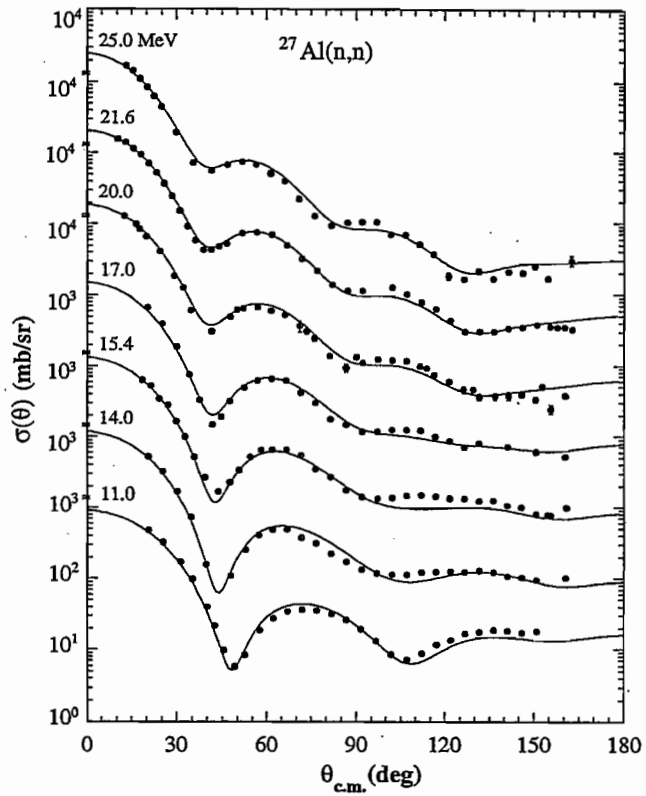

Figure 6.4. DOM calculations compared to the differential cross sections of neutron scattering from ^{27}Al at incident energies between 11 and 25 MeV. The dots are the experimental values and the solid curves are the DOM calculations.

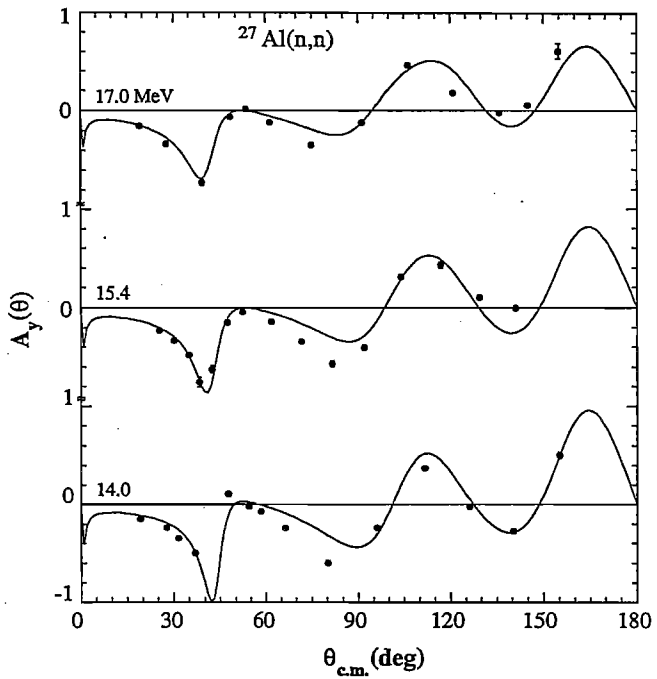

Figure 6.5. DOM calculations compared to the analyzing powers for neutron scattering from ^{27}Al at incident energies 14, 15.4 and 17 MeV. The solid curves are the DOM calculations and the dots are the analyzing power data.

6.5 The regional DOM for ^{27}Al, ^{28}Si and ^{32}S

Following the success of the development of the individual DOM for the three nuclei ^{27}Al, ^{28}Si, and ^{32}S, we present here the development of a regional DOM for the 2s-1d nuclei in the mass number region of $27 \leq A \leq 32$. The objective for the development of this regional optical model, which utilizes the dispersion relation is to determine if it is possible to obtain a constrained set of parameters that describes the scattering data of these nuclei. Although the model is "general" in nature, it preserve the characteristics (due to the different intrinsic structures) of these three nuclei. In the individual DOM analyses, the nuclear mean field NMF derived in Sect. 5.7.1 and Sect. 6.4 has two components. The first one is the HF component, which has a smooth dependence upon energy, mass number A and neutron excess. The second is the dispersive component, which is fundamentally due to the coupling of the neutron to the excited states of the core of the particular nucleus. This coupling (and hence the dispersive contribution) is expected to vary from one nucleus to the other. It is influenced by nuclear dynamics and cannot be expressed as a simple function of mass number or neutron excess [Mah 91, Joh 88]. Thus a regional model is not expected to give detailed agreement with the scattering data for every nucleus. However, in the models below, the individual values for the Fermi energy of each nucleus are introduced into the formulation. It is described below that merely introducing Fermi-energy differences is not adequate to represent the regional scattering data. To account for nuclear structure differences it was necessary to allow for stronger absorption in ^{28}Si and ^{32}S than in ^{27}Al. Thus, the concept of a regional model gives way to a "constrained" model in which the strength parameter of the surface and the volume terms were allowed to differ for the three nuclei. Eventually, in the last stage, the known isovector dependence of the real term of the optical potential was explicitly introduced in an attempt to partially compensate for the "structure dependence" on N and Z.

Since the concept of the NMF is an average nuclear potential, the NMF can only provide an average description for the properties of the bound states. In developing the regional model below, no attempt was made to adjust the parameters to predict the binding energies of the single-particle states in the negative energy region.

The databases for all three nuclei have been discussed in Sect. 4.1 and Sect. 6.4. The same version of the search code GENOA was used in this part of the work. Following the suggestion of Mahaux and Sartor, an energy offset of 3.0 MeV was used in the absorption forms. The first attempt in the search was to test how well the average values of the individual-DOM parameters predict the scattering data. The regional set of the average values are listed in the third right-hand column of Table 6.2 (we will refer to them as *Regional*). For all three nuclei, the *Regional* gives good fits to σ_T from 10 to 80 MeV and about 12% overestimation for E < 10 MeV for the three nuclei. In the case of ^{27}Al, the overestimation of *Regional* is 5% worse than that of the individual ^{27}Al-DOM, but in the case of ^{28}Si and ^{32}S, the overestimates are comparable to the individual DOM. Recall that the individual-DOM parameters in Chap. 5 were optimized in both energy regions (i.e., for both E < 0 and E > 0).

The predictions of the *Regional* for the differential cross sections are good and very similar to the fits obtained from their individual DOM. In the case of ^{27}Al, the predictions are consistently low at the backward angles for E > 14 MeV. This weakness in the ^{27}Al fit is due to the absorption being too large in the E > 14 MeV region. We conclude that the *Regional* parameters provide good absorption values for ^{28}Si and ^{32}S but too high for ^{27}Al. The lower absorption (relative to the other nuclei) favored by ^{27}Al was seen earlier in Sect. 6.4. Similarly, for the analyzing power data of ^{27}Al, ^{28}Si and ^{32}S, the *Regional* gave a comparable fit to that of the individual DOM.

Table 6.2 The Regional parameters for ^{27}Al, ^{28}Si and ^{32}S

Parameter	Regional	^{27}Al-Cons	^{28}Si-Cons	^{32}S-Cons
V_{HF} (MeV)	58.2	=	=	=
α_{HF}	0.52	=	=	=
r_V (fm)	1.17	=	=	=
a_V (fm)	0.69	=	=	=
r_{WS} (fm)	1.285	=	=	=
a_{WS} (fm)	0.53	=	=	=
A_V (MeV)	11.6	9.06	13.8	15.55
B_V (MeV)	82.0	=	=	=
Power n	4	=	=	=
A_S (MeV)	10.55	9.83	11.08	11.56
B_S (MeV)	8.0	=	=	=
C_S	0.012	=	=	=
Power m	6	=	=	=
V_{SO} (MeV)	5.5	5.81	5.81	5.81
α_{SO} $(MeV)^{-1}$	-0.015	=	=	=
r_{SO} (fm)	1.05	=	=	=
a_{SO} (fm)	0.45	0.48	0.48	0.48
Energy-offset (MeV)	3.00	=	=	=

Based on these results using the average parameters, an effort was made first to fine tune the spin-orbit potential parameters, relaxing the constraints made on them during the prediction of the B.E. of the bound states. An increase of 300 keV in the spin-orbit strength (see Table 6.2) gave an improved fit to the analyzing power data but only less than a 1% gain in the total χ^2 for the regional data set.

Next we focused on optimizing the volume and surface absorption parameters keeping the rest of the parameters as the average values. In this step, the search on the absorption parameters was carried out in the following sequence: *i*) upon the two constants A_V and A_S and *ii*) upon the three constants A_V, A_S and C_S. For the first sequence, 5.5%, 12% and 23% gains in the χ^2 (relative to that obtained with *Regional*) were reached in the case of ^{28}Si, ^{32}S and ^{27}Al, respectively. For the second sequence, where the exponent constant C_S was incorporated into the search, the gains in the χ^2 were 5.7%, 15% and 27% for ^{28}Si, ^{32}S and ^{27}Al, respectively. We should note that the χ^2 is very sensitive to small variations in the parameter values due to the small artificial error (i.e., heavy weight) assigned to the σ_T values. Although the fits to the scattering data were good in both cases, we choose the parameters obtained in the first sequence as our final regional parameters for the following reasons. In the second sequence of the search, the change in the sum of the χ^2 for all three nuclei was only 1.07 times better. Furthermore, it produced a large spread in the value of the exponent C_S, ranging from 0.008 for ^{32}S to 0.021 for ^{27}Al. A comparison between the different values of the parameters from the two search sequences is listed in Table 6.3.

Table 6.3 Comparison between the values of the two search sequences for the regional parameters for ^{27}Al, ^{28}Si and ^{32}S. Note that *seq. i* is the one chosen to be the regional parameters listed in Table 6.2

Parameter	^{27}Al-Cons		^{28}Si-Cons		^{32}S-Cons	
	seq. *i*	seq. *ii*	seq. *i*	seq. *ii*	seq. *i*	seq. *ii*
A_S (MeV)	9.06	10.52	13.8	14.07	15.55	13.71
B_S (MeV)	9.83	11.33	11.09	11.46	11.56	10.16
C_S	0.012	0.021	0.012	0.013	0.012	0.008

The quality of the fits from the two search sequences were very similar. For the three nuclei, we present the fits from the first sequence (call it constraint *Regional* DOM) to the total cross sections, $\sigma(\theta)$ distributions and the analyzing power data along with those obtained from the individual DOM. The predictions of the constraint *Regional* DOM to the total cross sections of ^{27}Al, ^{28}Si and ^{32}S are shown as dashed curves in Fig. 6.6. In this figure the previous fits from the individual DOM are also shown for the sake of comparison. The fits for $\sigma(\theta)$ of ^{27}Al are shown in Figs. 6.7 and 6.8, for ^{28}Si are shown in Figs. 6.9 and 6.10, and for ^{32}S are shown in Figs. 6.11 and 6.12, respectively. In Fig. 6.7, Fig. 6.9, and Fig. 6.11, the points are the estimates of the data for shape-elastic $\sigma(\theta)$. These values were obtained by subtracting predicted compound-nucleus values (see Ch. 4) from measured values of $\sigma(\theta)$. For $A_y(\theta)$, the fits are shown in Figs. 6.13, 6.14 and 6.15.

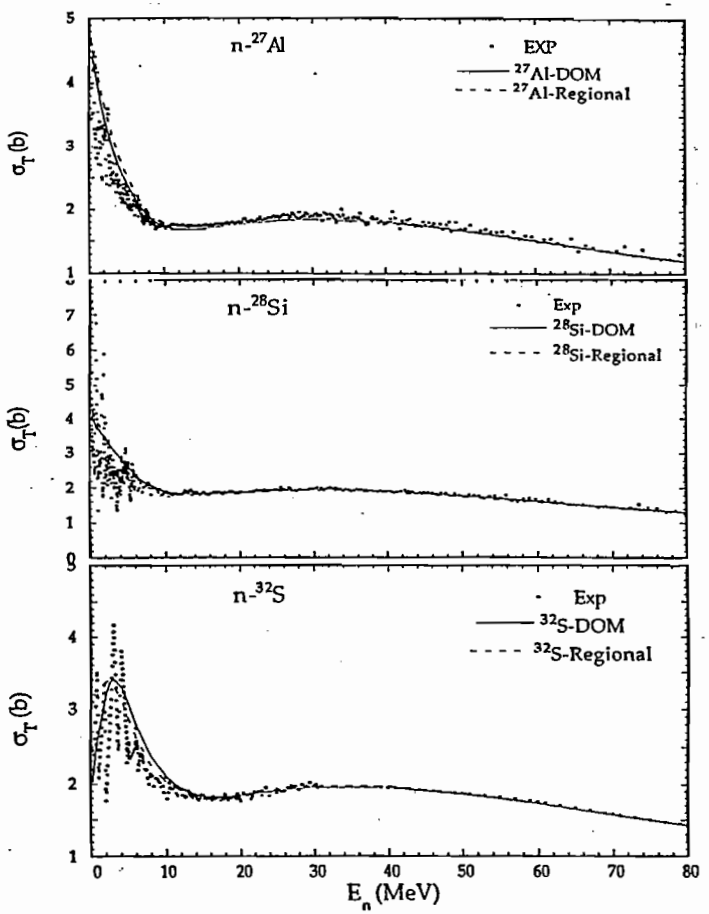

Figure 6.6. The individual and the constrained regional DOM predictions for the total cross sections of the three nuclei ^{27}Al, ^{28}Si and ^{32}S.

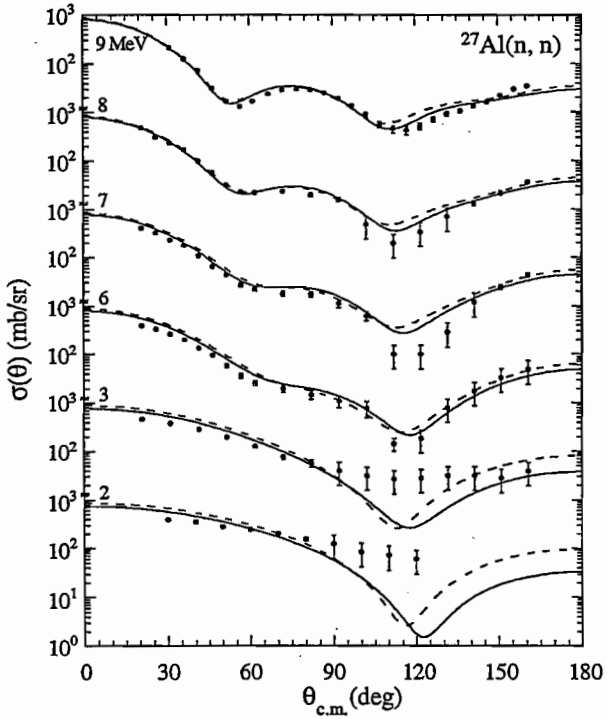

Figure 6.7. Individual DOM and constrained *Regional* DOM calculations compared to the differential cross sections of neutron scattering from ^{27}Al at incident energies between 2 and 9 MeV. The solid curves are the individual DOM calculations and the dashed curves are *Regional* DOM calculations. The dots are the shape-elastic values.

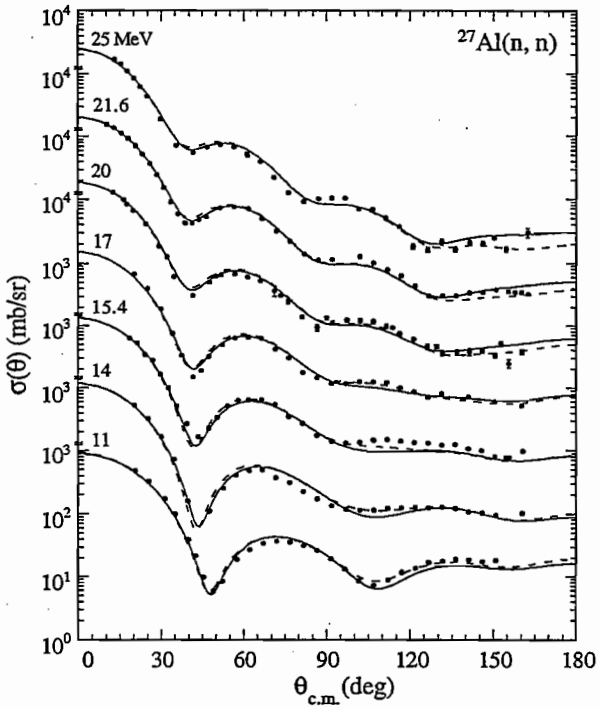

Figure 6.8. Individual DOM and constrained *Regional* DOM calculations compared to the differential cross sections of neutron scattering from ^{27}Al at incident energies between 11 and 25 MeV. The solid curves are the individual DOM calculations and the dashed curves are *Regional* DOM calculations. The dots are the experimental values.

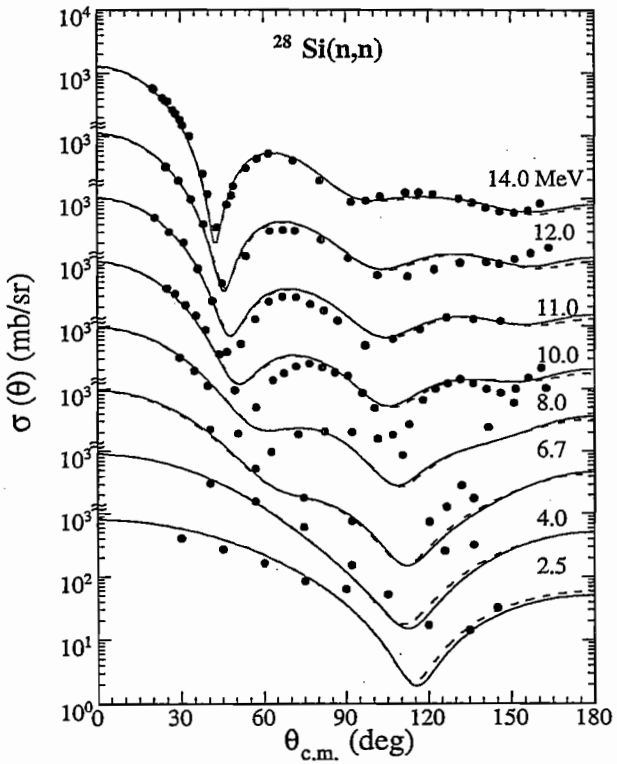

Figure 6.9. Individual DOM and *Regional* DOM calculations compared to the differential cross sections of neutron scattering from ^{28}Si at incident energies between 2.5 and 14 MeV. The solid curves are the individual DOM calculations and the dashed curves are the *Regional* DOM calculations. The dots are the shape-elastic values.

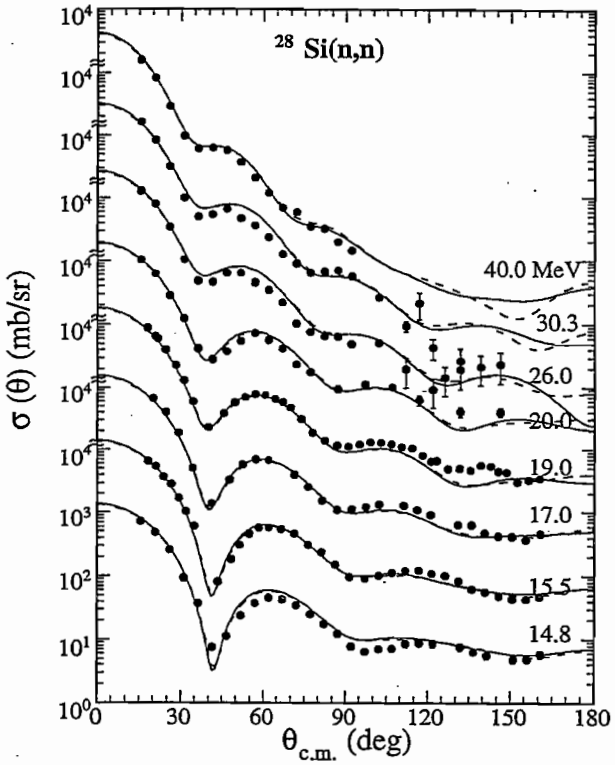

Figure 6.10. Individual DOM and constrained *Regional* DOM calculations compared to the differential cross sections of neutron scattering from ^{28}Si at incident energies between 14.8 and 40 MeV. The solid curves are the individual DOM calculations and the dashed curves are *Regional* DOM calculations. The dots are the experimental values.

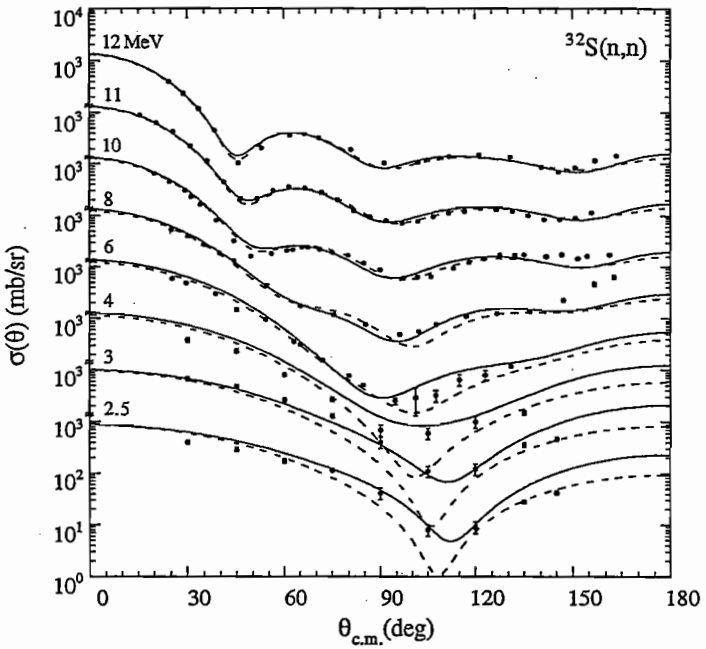

Figure 6.11. Individual DOM and constrained *Regional* DOM calculations compared to the differential cross sections of neutron scattering from ^{32}S at incident energies between 2.5 and 12 MeV. The solid curves are the individual DOM calculations and the dashed curves are *Regional* DOM calculations. The dots are the shape-elastic values.

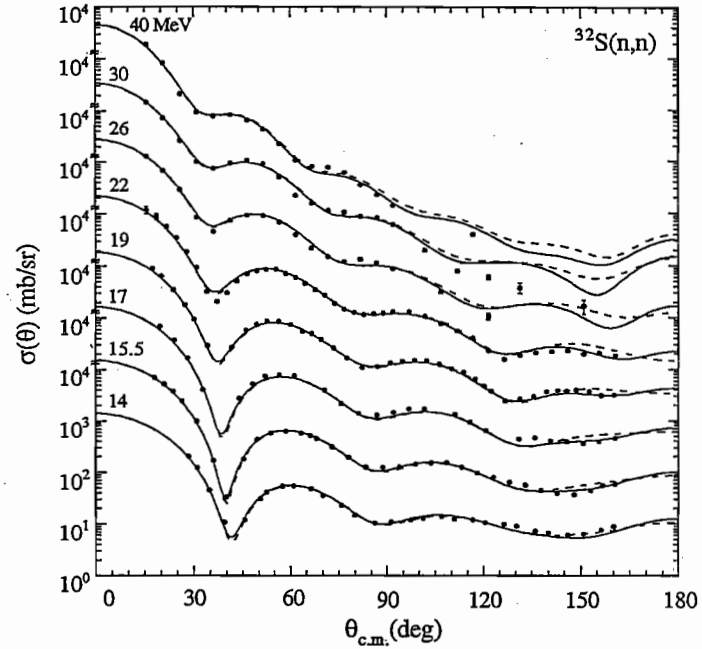

Figure 6.12. Individual DOM and constrained *Regional* DOM calculations compared to the differential cross sections of neutron scattering from ^{32}S at incident energies between 14 and 40 MeV. The solid curves are the individual DOM calculations and the dashed curves are *Regional* DOM calculations. The dots are the experimental values.

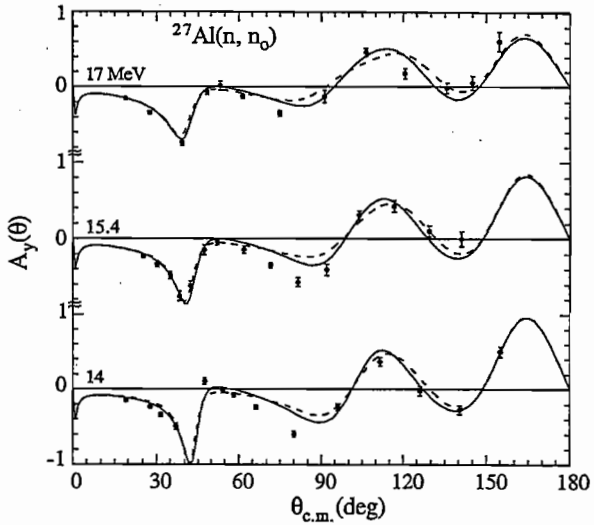

Figure 6.13. Individual DOM and constrained *Regional* DOM calculations compared to the analyzing powers for neutron scattering ^{27}Al at incident energies 14, 15.5 and 17 MeV. The solid curves are the individual DOM calculations and the dashed curves are *Regional* DOM calculations. The dots are the analyzing power data.

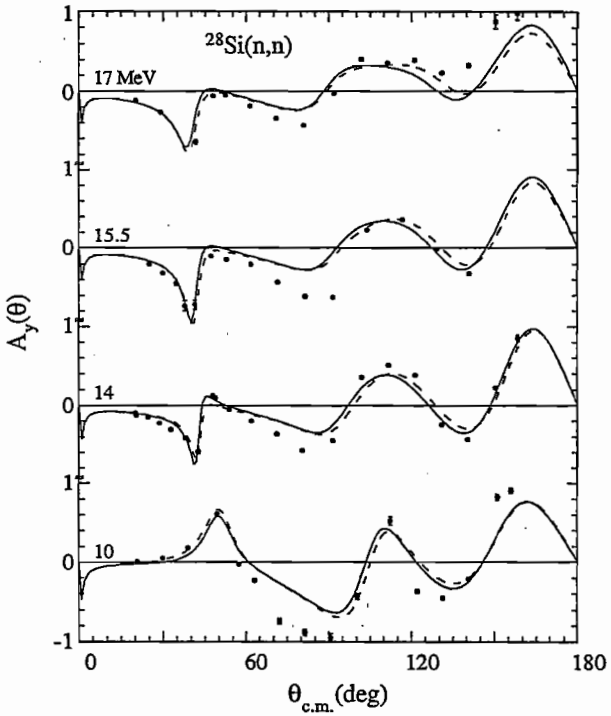

Figure 6.14. Individual DOM and constrained *Regional* DOM calculations compared to the analyzing powers for neutron scattering ^{28}Si at incident energies 10, 14, 15.5 and 17 MeV. The solid curves are the individual DOM calculations and the dashed curves are *Regional* DOM calculations. The dots are the analyzing power data.

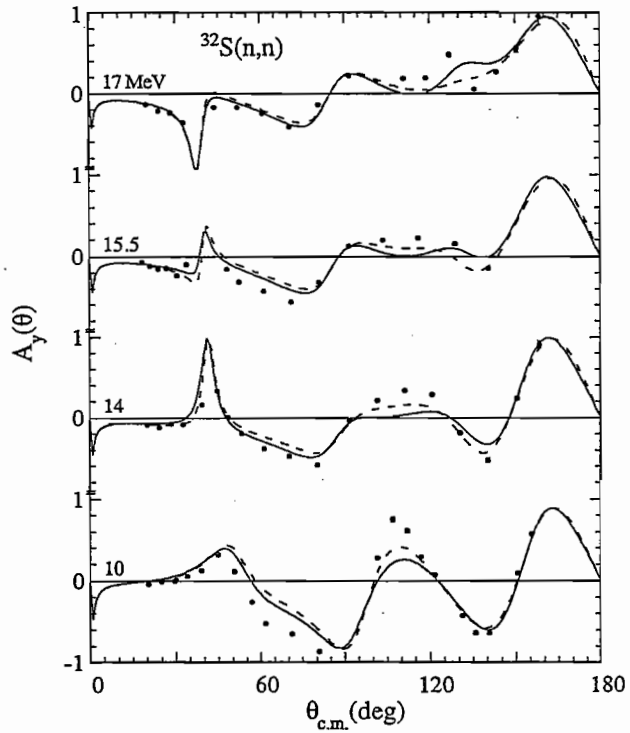

Figure 6.15. Individual DOM and constrained *Regional* DOM calculations compared to the analyzing powers for neutron scattering ^{32}S at incident energies 10, 14, 15.5 and 17 MeV. The solid curves are the individual DOM calculations and the dashed curves are *Regional* DOM calculations. The dots are the analyzing power data.

So far we developed a type of constrained or regional model for the three nuclei. In this regional model, all DOM parameters are the same except the two constants A_V and A_S of the volume and surface absorption. These parameters are listed in Table 6.2 as ^{27}Al-Cons, ^{28}Si-Cons and ^{32}S-Cons.

For the sake of interest and completeness, we extend the seq. *i* regional DOM (without adjusting any parameters) to the negative energy region for ^{28}Si and ^{32}S to see how well the binding energies of the single particles are predicted. On the second right-hand column of Figs. 5.10 and 5.18 the Regional-DOM prediction for the B.E. for states of ^{28}Si and ^{32}S are shown, respectively. The predictions for E_F of ^{28}Si and ^{32}S came within 4% and 3.5% (-12.31 and -11.44 MeV) of the values (-12.83 and -11.87 MeV) determined earlier from the separation energy calculations. The deepest hole state ($1s_{1/2}$) for ^{32}S was predicted (-65.55 MeV) 16% lower than the experimental value of -78.1 MeV.

6.5.2 Modification to the ^{27}Al-Constraint

The even-even nuclei (^{28}Si and ^{32}S) are self-conjugate, i.e., T=0, while ^{27}Al is not (T≠0). Therefore, there should be some difference for ^{27}Al because of the isovector component of the nuclear mean field.

A slight modification to the ^{27}Al-Constraint parameters (^{27}Al-Cons) was carried out to recalculate the value of the depth of the HF potential $V_{HF}(E = E_F)$ based on two considerations. The first was to account for the isospin dependence of the real central potential. The second, was to account for the influence of the difference in the Fermi energy on the depth of the HF potential between the three nuclei. For the first consideration, the isovector potential used was taken from the Walter-Guss model [Wal 86] in a similar way to that applied in Sect. 6.4. The value for $V_{HF}(E = E_F)$ (-57.59 MeV) was calculated from the real central potential obtained for the average value (-58.2 MeV, see Table 6.2) in the *Regional* model, that is V_{HF} = -58.2 – (-)0.61 = -57.59. In the second consideration we also include the effect of the difference in the Fermi energy (-1.95 MeV) (This difference in the Fermi energy was calculated from the difference between the average E_F of ^{28}Si and ^{32}S and E_F of ^{27}Al {1/2(12.83 + 11.87) - 10.4 = -1.95}). Keeping the same slope in *Regional*, a value (-56.58 MeV) was calculated from the real central potential of the average value {-56.58 =- 58.2 – (-)0.61 – (-)(1.95 × 0.52)}.

In this section we discuss the development (results) of three sets of parameters for the ^{27}Al Regional models: one with the HF depth calculated from the *average*, a second from *isospin only*, and a third from *isospin and the E_F-difference*. We will refer to these models as *^{27}Al-Cons*, *^{27}Al-CONS-1* and *^{27}Al-Cons-2* , respectively.

The new values for the depth of the HF potential (i.e., -57.59 and -56.58 MeV) were used in separate searches starting with the other parameters of *^{27}Al-Cons*. The constants A_V and A_S were optimized. Hence the parameters of the *^{27}Al-Cons-1* and *^{27}Al-Cons-2* models are identical to those of the *^{27}Al-Cons* model except for V_{HF}, A_V and A_S.

The fits to the scattering data from *^{27}Al-Cons-1* and *^{27}Al-Cons-2* models are nearly indistinguishable from those of the *^{27}Al-Cons* model except for small variations at the first minima of σ(θ) distributions for E > 14 MeV. Therefore, we only present the parameters of these three models in Table 6.4. The

parameters for the ^{27}*Al-Cons* model are listed again in Table 6.4 (from Table 6.1) for the convenience of comparison. Notice that in Table 6.4, the values of A_S are almost identical, which reflects that the A_V parameter is more sensitive to changes in V_{HF} than is the A_S parameter.

Table 6.4 The parameters for the modified versions of ^{27}Al-*Cons*

Parameter	^{27}Al-Cons	^{27}Al-G-1	^{27}Al-G-2
V_{HF} (MeV)	58.2	57.59	56.58
α_{HF}	0.52	=	=
r_V (fm)	1.17	=	=
a_V (fm)	0.69	=	=
r_{WS} (fm)	1.285	=	=
a_{WS} (fm)	0.53	=	=
A_V (MeV)	9.06	9.87	11.25
B_V (MeV)	82.0	=	=
Power n	4	=	=
A_S (MeV)	9.83	9.82	9.81
B_S (MeV)	8.0	=	=
C_S	0.012	=	=
Power m	6	=	=
V_{SO} (MeV)	5.81	=	=
α_{SO}(MeV)$^{-1}$	-0.015	=	=
r_{SO} (fm)	1.05	=	=
a_{SO} (fm)	0.48	=	=
Energy-offset (MeV)	3.00	=	=

6.6 Comparison between the regional models of DOM and SOM

In this section we compare the results of two regional analyses: the DOM developed in Sect. 6.5.1 and the conventional SOM [Mar 87]. The energy range studied in the DOM (0-80 MeV) is almost three times that studied in the SOM (14-40 MeV). Hence, the DOM involves a larger database for σ_T, $\sigma(\theta)$ and $A_y(\theta)$. The determination of the real potential in the two types of analyses is quite different. For the DOM, it is constrained by the requirement that the HF potential should yield nearly symmetric prediction for the bound states in the opposite side of the Fermi energy. (Although this constraint was not explicitly applied in the regional-model fitting, it was applied in determining the ^{28}Si and ^{32}S parameters that were the basis for obtaining the average or constrained DOM parameters. In the SOM, it is based solely on the best fit to the scattering data. Therefore, the DOM has a more physical base for determining the real potential. We realize that it is not too meaningful to compare DOM and SOM parameters because the dispersive correction introduces complicated energy variations in the strength and form factor of the real potential. Nevertheless, because the conventional SOM is the model classically used to describe elastic scattering, it may be of some usefulness to make the comparison for pedagogical or historical reasons.

The real and absorption geometries are very close in both analyses, while the spin-orbit parameters are smaller in the SOM (r_{so}= 1.00 fm and a_{so} =0.40 fm) than in the DOM (r_{so}= 1.05 fm and a_{so} =0.48 fm). The DOM used 11 sets of $A_y(\theta)$ data, while the SOM used only 7 sets of $A_y(\theta)$ data.

The DOM fit to σ_T is superior to the fit of the SOM for all three nuclei; the SOM prediction is consistently lower than the experimental data. For the differential cross section and the analyzing power data between 14 and 40 MeV, both the DOM and the SOM give good and comparable description to the measured data.

CHAPTER 7

Conclusions and comments

Conclusions and comments

The main objective of this study was to derive the nuclear mean field (NMF) for neutron scattering from ^{28}Si and ^{32}S in the broad energy range between -80 to +80 MeV. For each nucleus, the derived NMF gave a successful description for the total cross sections, differential cross sections and analyzing power data at the positive energies as well as a fairly reasonable prediction to the binding energies of the single particle states at the negative energies. This unified description of the NMF is made possible by utilizing the dispersion relation which connects the real and the imaginary part of the NMF through a DOM approach. The two derived NMFs support (and confirm the feasibility of) the approach which divide the NMF into Hartree-Fock-type and dispersive components. The HF component has a smooth dependence over a wide energy region, while the dispersive contribution is the one that contains the dynamical effects due to the coupling of the neutron single-particle configuration to the collective core excitations.

In order to derive a comprehensive NMF with improved accuracy of parameterization, the DOM analysis should make use of an extensive database at both energy regions. In the present work, and for the purpose of building the extensive database, differential cross-section angular distributions for elastic scattering were measured for the scattering of neutrons from ^{28}Si and ^{32}S at incident energies of 15.5 and 19 MeV. Furthermore, analyzing-power angular distributions for polarized neutron scattering from the same nuclei were measured at 15.5 MeV. The six scattering observables were incorporated with other data collected from experiments both at TUNL and other labs to form the most extensive study of ^{28}Si and ^{32}S, i.e., a study spanning the very wide energy range from -80 to +80 MeV.

The analysis applied in deriving the NMF in this work incorporated the recently introduced requirement that the absorption potentials vanish

in an energy region somewhere between $(E_F)^- < E < (E_F)^+$. However, this innovation did not affect the quality of agreement for σ_T at E < 10 MeV.

The DOM parameters listed in Tables 5.1 and 5.2 were able to describe the scattering observables quite well across the energy range of the study. However, the familiar optical-model overestimation problem of the total cross section at low energies (E<8 MeV) persists in the final results of the present study for ^{28}Si and ^{32}S (see Sect. 5.7.1 for discussion).

One area of the DOM which needs to be improved is the energy dependence of the absorption potentials. Although the current forms were able to give, on the average, adequate representation of the data in most energy regions, some difficulties for E < 8 MeV were confronted; this strongly suggests the need to improve the current form of the surface absorption. However, this low-energy problem with σ_T may also indicate a limitation of the DOM to produce the correct form-factor for the real potential as well.

Additional experimental data for the differential cross sections for E > 40 MeV is highly recommended to fully investigate the systematic behavior of the absorption potential at high energies; the end result would be the determination of more accurate DOM parameters at all energies.

The extension of DOM towards the negative energy region was reasonably able to predict the binding energies of the single-particle states. However, quantitative agreement for all the binding energies was not obtained. Part of this defect may be attributed to the deformation of these nuclei and also to the need for more accurate empirical bound-state information. In addition and in the spirit of any optical model for light (and deformed) nuclei, the DOM can only describe the average properties in specific energy region. That is, the NMF derived here is expected to describe the average properties of the bound states, but not to produce all the fine details in the excitation spectrum of these states for the n-^{28}Si and n-^{32}S systems.

The NMF derived in this work, in comparison with other NMF reported earlier, gave consistent results for the HF strength determination as well as for the real radius variation with mass number. The parametrization of the real radius (derived in Sect. 5.9) by incorporating the

NMF parameters of this study with other NMF parametrizations improved the accuracy of our knowledge of the A-dependence of the real radius reported in an earlier study of nuclei for the 40 < A < 208 region.

In addition, the development of a new DOM for n-^{27}Al gave a better prediction for the total cross section than the previous DOM over the entire range between 0–80 MeV and better representations of the differential cross-section data as well. The present DOM reduced the previous 26% overestimation of σ_T down to 8%, revealing the importance of determining the HF component in the negative energy region from empirical single-particle bound-state information for neighboring nuclei.

Another objective achieved in the present work is the development of a general DOM model for nuclei in the mass region of $27 \le A \le 32$. This "global" model followed the development of the individual DOM for the systems studied in the first part of the study. The average parameters from the individual DOMs gave a fair description to the scattering observables of all systems. However, a small re-optimization of the strengths of W_V and W_S furnished very good fits to $\sigma(\theta)$ and σ_T. The $A_y(\theta)$ data are well represented by the "global" parameters, both with or without the optimization of the absorption strengths. The success of the global DOM in describing the scattering data in the region of $27 \le A \le 32$ sheds light on the extension of a global DOM to other mass regions.

The extension of the DOM analysis to (p, p) scattering for the same T=0 nuclei (where the only difference is the Coulomb correction) will help in establishing the features of the Coulomb correction term more precisely.

The present work points to the possibility for future analyses that incorporate the dispersion relation approach to other deformed nuclei. It would be also desirable to extend the work to other light nuclei to study the full range of validity or applicability of the DOM.

References

[Ahm 76] I. Ahmad and Haider, *J. of Phys.*, G2 (1976) L157.

[Ala 86] R. Alarcon *et al.*, *Nucl Phys.* A458 (1986) 502.

[Bar 70] H.H. Barshall and W. Haeberli, eds., Polarization Phenomena in Nuclear Reactions, Third International Symposium, Madison, Wisconsin, 1970, University of Wisconsin Press.

[Bey 81] A. Beyerle, Ph.D. Dissertation, North Carolina State University (1981).

[Blc 82] Howell, private comunication with CEA group.

[Bol 64] L.N. Bolen and J.M. Eisenberg, *Phys Lett* 9 (1964) 52.

[Bre 64] D.J. Bredin, *et al.*, *Phys. Rev.* B135 (1964) 412.

[Che 88] T.S. Cheema and R.W. Finlay, *Phys. Rev.* C 37 (1988) 910.

[Cie 68] S. Cierjacks *et al.*, KFK-1000 (1968).

[Cle 89] T. B. Clegg *et al.*, TUNL Rep. XXIIX, (1989) 124.

[Del 88] J.P. Delaroche and W. Tornow, *Phys. Lett.* B203 (1988) 4.

[Del 90] J. P. Delaroche, Y. Wang and J. Rapaport, *Phys. Rev.* C 39 (1989) 391

[Dev 83] R. P. DeVito, *et al.*, *Phys. Rev.* C28 (1983) 2530.

[Dra 69] D.M. Drake *et al.*, *Nucl Phys.* A128 (1969) 209.

[Duh 68] H.H. Duhm, *Nucl Phys.* A118 (1968) 563.

[Eri 70] T.E. Ericson and M.P. Locher, *Nucl. Phys.* A148 (1970) 1.

[Far 66] S.A. Farris and J.M. Eisenberg, *Nucl Phys.* 88 (1966) 241.

[Fer 49] S. Fernbach, R. Serber and T. Taylor, *Phys. Rev.* 76 (1949) 1550.

[Fil 68] V.V. Fillippov *et al.*, 68 DUBNA. Ass-68.

[Fin 85] R.W. Finlay, J. Annand, J. Peter and F. Dietrich, *Phys. Lett.* B155 (1985) 313.

[Fos 71] D.G. Foster and D.W. Glasgow, *Phys. Rev.* C3 (1971) 576.

[Fru 84] S. Frullani *et al.*, *Adv. in Nucl. Phys.* 14 , (1984) 1.

[Gla 74] D. W. Glasgow, Ph.D. Dissertation, Duke University (1974).

[Gou 81] C.R. Gould, L. Holzsweig, S.E. King, Y.C. Lau, R.V. Poore, N.R. Roberson, and S. Wender, IEEE Transactions on Nuclear Science NS-28 (1981) 3708.

[Gri 69] S.M. Grimes, *Nucl Phys.* A124 (1969) 369.

[Gru 77] H. Gruppelar and G. Reffo, *Nucl. Sci. and Eng.* 62 (1977) 756.

[Gus 82] P. Guss, Ph.D. Dissertation, Duke University (1982).

[Hae 73] W. Haeberli, in Lecture Notes in Physics, No. 30, D. Fick, editor, Springer-Verlag, Berlin, Heidelberg, New York, 1973, p. 232.

[Hae 74] W. Haeberli, in Nuclear Spectroscopy and Reactions, Part A, J. Cenry, editor, Academic Press, New York, 1974, p. 151.

[Hod 71] P.E. Hodgson, *Nuclear Reactions*, Oxford University Press (1971).

[Hol 69] B. Holmquist *et al*, R-AE-366 (1969).

[Hon 83] G. Honore and R. Byrd, JANE Users Manual, TUNL, Internal Report, 1983.

[Hop 71] J. C. HOPKINS And G. Breit, *Nuclear Data Table* A9 (1971) 137.

[How 84] C. R. Howell, Ph.D. Dissertation, Duke University (1984).

[Jeu 91] J. P. Jeukenne, C. Mahaux and R. Sartor, *Phys. Rev.* C 43 (1991) 2211.

[Joh 87] C.H. Johnson, D.J. Horen and C. Mahaux, *Phys. Rev.* C 36 (1987) 2252.

[Joh 88] H. Johnson and C. Mahuax, *Phys. Rev.* C 38 (1988) 2589.

[Joh 89] C.H. Johnson, R.F. Carlton and R.R. Winter, *Phys. Rev.* C 39 (1989) 415.

[Kin 72] W. Kinney, ORNL 4823 (1972).

[King 81] S. E. King, Y. Lau, C. R. Gould, *IEEE trans. Nucl. Sci*, NS-28, (1981) 3822.

[Koe 87] W. Koehler *et al, J Phys.* C35 (1987) 1646.

[Kro 26] R.D.L. Kronig, *J. of the Opt. Soc. of Am.*, 12 (1926) 547.

[Lar 81] D.C. Larson *et al,* ORNL 5787 (1981).

[Law 87] R.D. Lawson, P. Gunther and A.B. Smith, *Phys. Rev.* C36 (1987) 1298.

[Lip 68] R. Lipperheide and A.K. Schmidt, *Nucl. Phys.* A112 (1968) 65.

[Mah 81] C. Mahaux and and H. Ngô, *Phys. Lett.* B100 (1981) 285.

[Mah 82] C. Mahaux and H. Ngô, *Nucl. Phys.* A378 (1982) 205.

[Mah 85] C. Mahaux and R. Sartor, *Theory of Nuclear Structure and Reactions* p. 12, World Scientific Publishing Co., 1985.

[Mah 86A] C. Mahaux, H. Ngô and R. Sartor, *Nucl. Phys.* A449 (1986) 354.

[Mah 86B] C. Mahaux and R. Sartor, *Nucl. Phys.* A460 (1986) 466.

[Mah 86C] C. Mahaux and R. Sartor, *Nucl. Phys.* A458 (1986) 25.

[Mah 87] C. Mahaux and R. Sartor, *Nucl. Phys.* A468 (1987) 193.

[Mah 88] C. Mahaux and R. Sartor, *Nucl. Phys.* A481 (1988) 407.

[Mah 89] C. Mahaux and R. Sartor, *Nucl. Phys.* A493 (1989) 157.

[Mah 91] C. Mahaux and R. Sartor, *Adv. Nucl. Phys.* 20 (1991) 1.

[Mar 87] Ph. Martin, *Nucl. Phys.* A466, (1987) 119.

[Nag 92] M. M. Nagadi, Ph.D. Dissertation, Duke University (1992).

[Ndt 71] Nuclear Data table, v.9, no.4-5 (1971) 308.

[Neg 70] J. W. Negele, *Phys. Rev.* C 1 (1970) 1260.

[Ohl 72] G. Ohlsen, *Rep. Prog. Phys.* 35 (1972) 717.

[Ols 87] N. Olsson et al, *Nucl. Phys.* A472 (1987) 237.

[Pas 67] G. Passator, *Nucl. Phys.* A95 (1967) 694.

[Per 63A] F.G Perey, *Phys. Rev.* 131 (1963) 745.

[Per 63B] C. M. Perey and F.G Perey, *Phys. Rev.* 132 (1963) 755.

[Per 72] F.G Perey *et al,* ORNL-4823 (1972).

[Pet 60] G.A Petitt *et al, Nucl Phys.* 79 (1960) 231.

[Pet 85] J.S. Petler *et al , Phys. Rev.* C 32 (1985) 673.

[Rob 81] N. R. Roberson and S. E. Edwards, *IEEE trans. Nucl. Sci,* NS-28, (1981) 3834.

[Rob 88] M. Roberts, Ph.D. Dissertation, Duke University (1988).

[Sat 87] G.R. Satchler, *Nucl. Phys.* A472 (1987) 591.

[Sch 89] G. Schreder *et al, Phys. Rev.* C39 (1989) 1768.

[Smi 86] A.B. Smith, P. Gunther and R.D. Lawson, *Nucl. Phys.* A455 (1986) 344.

[Spi 65] B.M. Spicer, *Aust. J. Phys.* 15(1965)1.

[Tai 82] R.C. Tailor, Ph. D. Dissertation, Ohio University (1982).

[Tor 87] W. Tornow, E. Woye, and R.L. Walter, *J. Phys. G: Nucl. Phys.* 13, (1987) 177.

[Tor 88] W. Tornow and J.P. Delaroche, *Phys. Lett.* B210 (1988) 26.

[Tor 90] W. Tornow and Z.P. Chen, *Phys. Rev.* C 42 (1990) 693.

[Tsu 63] K. Tsukada *et al, J. Phys.* J18 (1963) 610.

[Vel 74] D.E. Velkley, *Phys. Rev.* C 9 (1974) 2181

[Vir 81] A. Virdis *et al,* Bruyeres-le-Châtel Annual Report, CEA-R-5144 (1981) 502

[Wan 86] Y. Wang and J. Rapaport, *Nucl. Phys.* A454 (1986) 359.

[Whi 84] C.S Whisnant *et al, Phys. Rev.* C 30 (1984) 1435.

[Wie 86] J.S. Wienfield *et al, Phys. Rev.* C 33(1986)33.

[Wei 92] G. J. Weisel, Ph.D. Dissertation, Duke University (1992).

Biography

Mohammad Abdulaziz Al-Ohali

Born: Unayzah, Saudi Arabia September 5, 1959.

Education:

1982	B. Sc., Physics, King Fahad University for Petroleum and Minerals (KFUPM), Dhahran, Saudi Arabia.
1985	M. Sc., Physics, King Fahad University for Petroleum and Minerals, Saudi Arabia.
1988	M. Sc., Physics, Duke University, U.S.A.

Positions: 1982-1985 Graduate Assistant, KFUPM.

Memberships: American Physical Society

Journal Articles:

1. *Neutron-proton analyzing power data betwen 7.6 and 18.5 MeV*, G. Weisel, W. Tornow, C.R. Howell, P.D. Felsher, M. A. Al-Ohali, Z. P. Chen and R.L. Walter, Phys. Rev. C46 (1992) 1599.
2. *The low-energy neutron-deuteron analyzing power and the $^3P_{0,1,2}$ interactions of nucleon-nucleon potentials*, W. Tornow, C.R. Howell, M. A. Al-Ohali, Z.P. Chen, P.D. Felsher, J.M. Hanly, R.L. Walter, G. Weisel, G. Mertens, I. Slaus, H. Witala and W. Glöckle, Phys. Let. B257 (1991) 273.
3. *Neutron-proton analyzing power data at 7.6, 12.0, 14.1, 16.0, 18.5 MeV*, G.J. Weisel, W. Tornow, C.R. Howell, P.D. Felsher, M. A. Al-Ohali, Z.P. Chen, R.L. Walter, J.M. Lambert and P.A. Treado, Colloque De Physique, Colloque C6, supplèment au mo22, Tome 51 C6-515 (1990).

4. *Analyzing power for $^{12}C(n_{pol},n_{0,1})^{12}C$ and evaluation of n-^{12}C scattering at 18.2 MeV*, W. Tornow, C.R. Howell, H.G. Pfützner, M.L. Roberts, P.D. Felsher, Z.M. Chen, M. A. Al-Ohali, G.J. Weisel, R.L. Walter and A.A. Naqvi, J. Phys. G: Nucl. Phys. 14 (1988) 49.
5. *Stellar Krypton cross section at kT = 25 and 52 keV*, F. Käppler, A. A. Naqvi and M. A. Al-Ohali, Phys. Rev. C35 (1987) 936.
6. *Stellar cross section at kT=52 keV: The exapmpla of $^{85}Kr^m$*, F. Käppler, A. A. Naqvi and M. A. Al-Ohali, ADVANCES IN NUCLEAR ASTROPHYSICS, Edited by: E. Vangioni-Flam, J. Audouze, M Casse, J. Chieze and J. Thanh Van, (Proceedings of the Second Institut d'Astrophysique (IAP) Workshop, Paris, France July 7-11, 1986, pages 567-575)

Conference abstracts and associated talks:

Dispersion-Relation Optical Model for n+ ^{28}Si, M. A. Al-Ohali, J. P. Delaroche, C. R. Howell, W. Tornow And R. L. Walter, Bull. of the Amer. Phys. Soc., 35 (1990) 1650.

Large Discrepancies Between Rigrous Faddeev Calculations and Elastic Neutron-Deutron Analyzing-power data at Low Energies, W. Tornow, C. R. Howell, M A. Al-Ohali, Z.P. Chen, P.D. Felsher, J.M. Hanly, R.L. Walter, , G.J. Weisel, and G. Mertens, Contributed Papers in the 7th International Confernce on Polarization Phenomena in Nuclear Physics, Paris , 28A (1990).

Measurements of Vector and Tensor Analuzing Powers for d-p and d-n Quasifree Scattering using the d+d → d+p+n Breakup Reaction at 12 MeV

Compared to Plane-Wave-Impulse-Approximation Calculations, P.D. Felsher, C.R. Howell, W. Tornow, I. Slaus, J.M. Hanly, G.J. Weisel, M. A. Al-Ohali, R.L. Walter, G. Mertens, J.M. Lambert, P.A. Treado and Y. Koike, Bull. of the Amer. Phys. Soc., **35** (1990) 979.

Report on Operation of a New Intense Polarized Ion Source and ECR Ionizer. T. B. Clegg, D. Abbott, T. Black, E. Crosson, R. Das, K. Fletcher, C. R. Howell, N. R. Roberson, K. Sweeton, W. Tornow, W. Wilburn, and Z. Williams. In Proceedings of the 7th International Conference on Polarization Phenomena in Nuclear Physics, Paris 90, page 3E (1990).

Analyzing power data for $^{209}Bi(n,n)$ at 6 and 9 MeV, G.J. Weisel, W. Tornow, C.R. Howell, M.L. Roberts, P.D. Felsher, M. A. Al-Ohali, J.M. Hanly, R.L. Walter and G. Mertens, Bulletin of the Amer. Phys. Soc., 35 (1990) 1039.

Analyzing-power data for neutron scattering from protons between 7.6 and 18.5 MeV, G.J. Weisel, W. Tornow, C.R. Howell, P.D. Felsher, Z.P. Chen, M. A. Al-Ohali, J.M. Hanly, R.L. Walter, J.M. Lambert and P.A. Treado, Bulletin of the Amer. Phys. Soc., 34 (1989) 1140.

Neutron Detector Efficiency Calculations Compared to Experimental Determinations, P.D. Felsher, J.M. Hanly, W. Tornow, C.R. Howell, M. A. Al-Ohali, Z.P. Chen, G.J. Weisel, R.L. Walter and G. Dietze Bulletin of the Amer. Phys. Soc., 33 (1988) 2195.

Analyzing power data for neutron scattering from ^{209}Bi at 6 and 9 MeV, G.J. Weisel, W. Tornow, C.R. Howell, M.L. Roberts, P.D. Felsher, M. A. Al-Ohali, J.M. Hanly, R.L. Walter and G. Mertens, Bulletin of the Amer. Phys.

Soc., 33 (1990) 2195.

Neutron-proton analyzing power data below 20 MeV, G.J. Weisel, W. Tornow, C.R. Howell, M. A. Al-Ohali, Z.P. Chen, P.D. Felsher, J.M. Hanly, J.M. Lambert, P.A. Treado and R.L. Walter, Contributed Papers from Few Body XII, 12th Int. Conference on Few Body Prob. in Phys., Vancouver, C13 (1989).

Conference abstracts and associated posters:

A Dispersive Optical Model for neutron scattered from ^{28}Si, M. A. Al-Ohali, G .J. Weisel, W. Tornow, C.R. Howell, J. P. Delaroche and R.L. Walter, Contributed Papers in 7th International Conference on Polarization Phenomena in Nuclear Physics, Paris, Paris 90, 85B (1990).

Analyzing power data for $^{209}Bi(n,n)$ at 6 and 9 MeV and corrections for compound nucleus reactions, G.J. Weisel, W. Tornow, C.R. Howell, M.L. Roberts, P.D. Felsher, M. A. Al-Ohali, J.M. Hanly, R.L. Walter and G. Mertens, Contributed Papers in 7th Int. Conference on Pol. Phen. in Nucl. Phys., Paris 90, 85B (1990).

Neutron-proton analyzing power data at 7.6, 12.0, 14.1, 16.0, 18.5 MeV, G.J. Weisel, W. Tornow, C.R. Howell, P.D. Felsher, M. A. Al-Ohali, Z.P. Chen, R.L. Walter, J.M. Lambert and P.A. Treado, Contributed Papers in 7th International Conference on Polarization Phenomena in Nuclear Physics, Paris 90, 16D (1990).